An Investigation of the Outskirts of the Galaxy Cluster XLSSC122

by

Bryn Lonsbrough
B.Sc/B.A, University of California Santa Cruz, 2022

A Thesis Submitted in Partial Fulfillment of the
Requirements for the Degree of

MASTER OF SCIENCE

in the Department of Physics and Astronomy

University of Victoria

We acknowledge and respect the Lək̓ʷəŋən (Songhees and Xʷsepsəm/Esquimalt) Peoples on whose territory the university stands, and the Lək̓wəŋən and W̱SÁNEĆ Peoples whose historical relationships with the land continue to this day.

An Investigation of the Outskirts of the Galaxy Cluster XLSSC122

by

Bryn Lonsbrough
B.Sc/B.A, University of California Santa Cruz, 2022

Supervisory Committee

Dr. Jon Willis Supervisor Main, Supervisor
(University of Victoria Department of Physics and Astronomy)

Dr. Pat Côté Member, Departmental Member
(University of Victoria Department of Physics and Astronomy, NRC Herzberg)

Abstract

I investigate the redshift 1.98 galaxy cluster XLSSC 122 using the Hubble Space Telescope (HST) from the core of the cluster out to 3 Mpc, a scale equivalent to 10 times the $R_{500} = 295\,\mathrm{kpc}$ radius. I present an expanded photometric and spectroscopic catalogue of the cluster, bringing the total number of spectroscopically classified member galaxies to 74, with 35 new member galaxies added in the outer regions of the cluster. I compute the radial galaxy number density profiles in the cluster, and observe no clear evidence of infalling groups or cosmic filaments. I observe a clear bimodal colour relation in member galaxies, with an increasing number of red galaxies approaching the cluster centre. This red fraction enhancement, as well as the coincident appearance of post-starburst galaxies, indicates a rapid cessation of star formation as galaxies enter the cluster. We use a simple model to show that the observed galaxy properties may be explained by ram pressure stripping at or near the virial radius of the cluster.

Table of Contents

List of Tables

List of Figures

Acknowledgements

I would like to thank:

Dr. Jon Willis, for his mentorship and guidance, and for encouraging me to be a more independent researcher. I am grateful that our work felt more like a collaboration than an instruction.

Dr. Rebecca Canning, for her patience in teaching me the workings of the Hubble reduction pipeline, and for taking the time to meet with me outside of her more pressing commitments.

Dr. Pat Côté, for his advice and encouragement throughout this work, and for serving on my committee and providing thorough feedback.

My mother and sisters, Kim, Taryn, and Ainsley Lonsbrough for their unwavering support and love. Though you are far from here I hold you in my heart and cherish your journey.

My friends, Josh, Daniel, Aviv, Ruxin, Jono, Diego, Ted, Cam, and Shoshannah, (not extensive) for their grounding presence and guidance in the progression of this work. Thank you for allowing space for a respite amidst the storm of expectations.

My coworkers and GARGOYLE members, for providing a space to talk about galaxies, and for a diversity of perspectives.

Simon, For his mentorship, and for showing me the ropes. You made that integration far smoother than it would have been.

The pursuit of knowledge is a lifelong journey, not a destination.
Isaac Aasimov

Dedication

This work is dedicated to:
My grandparents, Angus and Lynda Todd
Thank you for sharing with me your knowledge of the world, it’s people, and a love of Canada.
Those who question
Whether it be the nature of the universe or your personal form and place within it
May you hold the light of hope within you during these dark days
and create a more harmonious future when time allows
Love will conquer hate

Chapter 1

Introduction

Galaxy clusters offer an important environment to study the formation and evolution of galaxies across cosmic time (Dressler, 1980; Peng et al., 2012; Wetzel et al., 2013), with cluster cores hosting a greater number of red galaxies than the surrounding field (Balogh et al., 2004; Gladders and Yee, 2005; Rykoff et al., 2014; Strazzullo et al., 2016; Balogh et al., 2016) and the outskirts hosting galaxies in the midst of evolution from active to passive (McGee et al., 2009; Webb et al., 2020; Werner et al., 2022). Galaxies in cluster outskirts experience a cessation of star formation (quenching) in part due to the interplay of high concentrations of member galaxies with a hot intracluster medium (ICM) and a parent dark matter halo (Gunn and Gott, 1972; Abadi et al., 1999; McGee et al., 2009), a process which has been observed in the local universe in the stripping of gas from galaxies in infall regions (Paccagnella et al., 2017; Brown et al., 2017; Watts et al., 2023). The bimodal colour distribution of cluster galaxies from the local universe to at least $z = 2$ (Balogh et al., 2004; Strazzullo et al., 2019; Willis et al., 2020) indicates that rapid quenching is present from early cosmic times. This work focuses on the properties of galaxies in the outskirts of the $z = 2$ galaxy cluster XLSSC 122, tracing the effects of environment on the evolution of its infalling galaxies.

1.1 Historical Background for Researching Galaxy Clusters

Early astronomers noticed clusters of faint extended objects in the sky (Messier, 1781; Herschel, 1786). When we discovered that these galaxies were located outside of the Milky Way (Shapley and Ames, 1932; Abell, 1958), we could identify these structures as galaxy clusters. At later times, astronomers connected galaxy clusters to large dark matter halos (Zwicky, 1933) and a hot baryonic plasma intracluster medium (ICM) (Gursky et al., 1971). Despite the fact that they are dark matter dominated structures, galaxy clusters remain labelled by the galaxy populations they host. Galaxy clusters are useful as probes of the early universe, as they are massive gravitational assemblages of galaxies that trace the distribution of dark matter in the cosmic web (Abell, 1958; Libeskind et al., 2018). As the universe evolves forward in time, their overdensity increases compared to the early universe. Early universe galaxy clusters in particular are then useful for studying this early structure because they provide a large number of galaxies in an environment dissimilar to our local universe, and can trace the earliest effects of environment on the formation and evolution of galaxies (Dressler, 1980; Poggianti et al., 1999; Balogh et al., 1999, 2004; Strazzullo et al., 2019; van der Burg et al., 2020; Trudeau et al., 2022).

1.2 Galaxy Clusters

1.2.1 Cluster Origins and Evolution

The early universe experiences a variety of quantum fluctuations, leading to minor overdensities in the dark matter mass distribution which grow over time and merge with other gravitationally bound structures, or halos (Blumenthal et al., 1984, 1986; Navarro et al., 1995). Low mass overdensities are more compact, and collapse earlier (Blumenthal et al., 1984). At later times, these smaller developing halos are drawn into more massive, later collapsing halos (White and Rees, 1978; Blumenthal et al., 1984; White and Frenk, 1991; Muldrew et al., 2015). These massive amalgamations of dark matter form the largest overdensities in the universe, galaxy clusters. In the process of this accretion, shearing forces and attraction carve the universe into long filaments separated by voids (Bond et al., 1996; Libeskind et al., 2018). Galaxy clusters occupy the nodes in this cosmic web and are in turn connected to filamentary structures (Muldrew et al., 2015; Libeskind et al., 2018; Santiago-Bautista et al., 2020). These outlying overdensities continue to funnel new material into a cluster, maintaining a stream of new galaxies, dark matter, and gas (McGee et al., 2009; Martínez et al., 2016; Trudeau et al., 2022). A galaxy in a cluster environment may arise from an infalling group, cluster, filament, or other overdensity, or originate from a void, or other region of lower density. Individual galaxies, though affected at this time by the cluster itself, may have drastically different origins, leading to a different star formation history and evolution (Bahé et al., 2013). By looking at galaxies in the early universe one can trace their eventual evolution through time to the local universe (Chiang et al., 2013). Tracing clusters out to higher redshifts traces not only the evolutionary histories of our own galaxy and nearby clusters, but also provides estimates for our universe's changing cosmology (Eke et al., 1996).

1.2.2 Spherical Collapse

A simple model for the formation of dark matter halos is the collapse of an initial sphere of dark matter in an expanding universe with a small initial overdensity at the centre. The overdense halo initially expands at a rate slower than the expansion of the universe, leading to an increase in the density contrast (Gunn and Gott, 1972). If one placed a test particle at the edge of the overdense region it would eventually stop expanding and turn back to fall into the centre of the overdensity. Before collapsing, the interactions between mass components will bring the cluster into a stable equilibrium defined by the virial equation seen in Peebles (1980) and shown in Eq. 1.1, a balance between the bulk kinetic and potential energies in a cloud of collisionless particles. The radius of virialization occurs at a density contrast under spherical collapse as $\rho_{vir}/\rho_{critical} = 178$ (Bryan and Norman, 1998). Here, ρ_{vir} is the density within a circle of radius r_{vir} from the centre of mass. Often, the virial radius is quoted as $r_{vir} = r_{200}$, where r_{200} is the radius at which the overall density of the mass component (predominantly dark matter) is $\rho_{vir}/\rho_{critical} = 200$. Going forward, the use of a radius R_x indicates the radius of a sphere (or observationally a projected circle) within which the density is x times the critical density of the universe.

Over time, the turnaround radius increases as farther regions are accelerated opposite their expansion velocity. However, such an idealized spherical collapse is complicated by the existence of other dark matter halos in the universe, as well as the assumption that mass is uniformly distributed in a sphere. As there are a great number of over and under-dense regions in the universe, the true behaviour of dark matter halos is far more complex. Merging halos, filamentary structures, and tidal effects all break the behaviour of a simple collapse. Though in the central regions of relaxed clusters, those not showing any major perturbations, a collisionless gravitationally bound system of particles approximates both the dark matter and galaxy distribution, allowing a rough characterization of cluster mass and extent.

1.2.3 Virialization

A galaxy cluster's dark matter halo can be considered as a collection of collisionless moving particles bound by a conservative force of gravity (Zwicky, 1933). When characterizing a galaxy cluster, one often talks about its virial radius, and virial mass. The virial radius is the radius within which the particles in the dark matter halo have a balanced kinetic and potential energy according to Eq. 1.1 as adapted from Binney and Tremaine (1987).

$$< T >= -\frac{1}{2} < U > \tag{1.1}$$

Here, $< T >, < U >$ are the average kinetic and potential energies of the mass component. A cluster is considered virialized when the mass contained within a radius r_{vir} satisfies Eq. 1.1 (Binney and Tremaine, 1987). An early use of the virial theorem was to estimate the gravitational mass in a galaxy cluster by using the motion of its galaxies as tracers of the potential well (Zwicky, 1933). The exceptional speeds of the galaxies in a cluster were suggestive of a higher total mass than visible mass, indicating that a cluster environment contains dark matter in large amounts. With X-ray data one can relate the kinetic energy of the ICM particles given by the virial theorem to the thermal energy of the plasma as observed in the X-ray range (Bryan and Norman, 1998). The mass of a cluster can also be inferred from the gravitational effect of the cluster mass on the light passing through or near to the cluster. This gravitational lensing traces the mass distribution of the entire cluster mass component, rather than the visible mass in the cluster, and can be used to infer the dark matter distribution (Bartelmann and Schneider, 2001; Hoekstra, 2003).

1.2.4 X-ray Emission

Extended emission of X-ray photons have been found in the direction of galaxy clusters from the local universe (Zwicky, 1933; Gursky et al., 1971) and clusters out to out to $z = 2$ (Mantz et al., 2018). The ICM of a galaxy cluster produces high energy photons via Bremsstrahlung, or "breaking radiation". In this process, charged particles (mostly protons and electrons) are decelerated and deflected via electromagnetic interaction. This change in energy of the interacting particle releases energy in the form of photons with emissivity given by Eq. 1.2 as expressed in Sarazin (1986).

$$\epsilon_\nu^{ff} = \frac{2^5 \pi e^6}{3 m_e c^3} \left(\frac{2\pi}{3 m_e k} \right)^{\frac{1}{2}} Z^2 n_e n_i g_{ff}(Z, T_g, \nu) T_g^{\frac{1}{2}} \exp\left(\frac{-h\nu}{kT_g} \right) \tag{1.2}$$

Here, ϵ_ν^{ff} is the energy per unit time, frequency ν, and volume V of an ion of charge Z in a plasma with electron temperature T_g, n_i is the ion number density, n_e is the electron number density, and g_{ff} is a correction for quantum mechanical effects. Since the ICM is hot, the photons released are primarily observed in the X-ray range, where the power output peaks. As an example of the X-ray extent of a galaxy cluster the blue contours in Fig. 1.1 trace the X-ray emission from the galaxy cluster XLSSC 122 (Willis et al., 2020; Mantz et al., 2018), theoretically tracing the extent of the ICM. Massive ($M_{500} > 10^{15} M_\odot$) galaxy clusters can have temperatures upwards of 5-13 keV (Sayers et al., 2019), whereas less massive clusters can have temperatures closer to 1-3 keV (Zou et al., 2016).

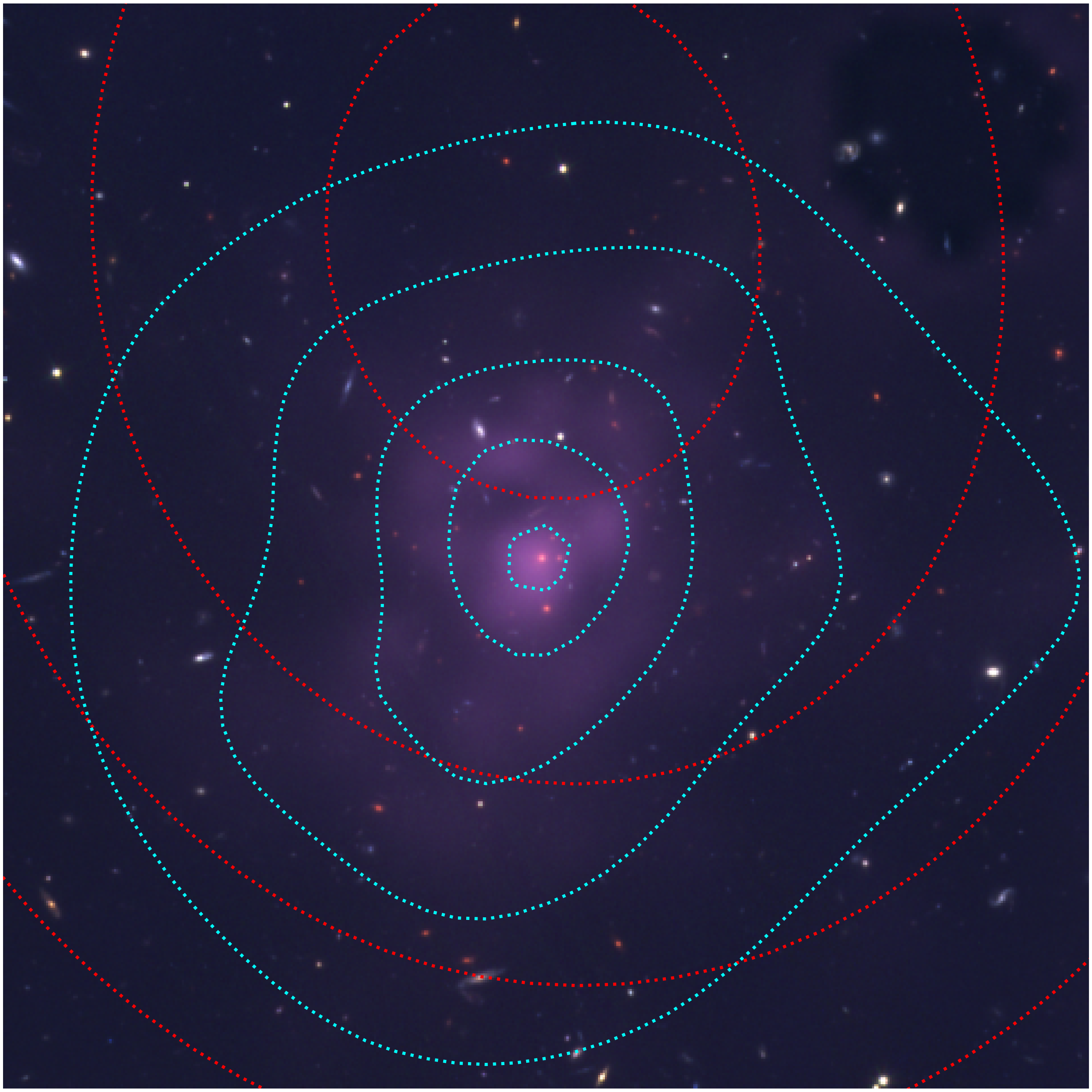

Figure 1.1: X-ray emission (purple) from the XMM-Newton space telescope from (Mantz et al., 2018) overlaid on an rgb colour image incorporating data from the Hubble Space Telescope data taken in Cycle 25 (r = F140W, g = F105W) and Cycle 30 (b = F814W) for the galaxy cluster XLSSC 122. Radio contours (red dotted) and X-ray contours (cyan dotted) are overlaid showing the extent of the ICM's radio and X-ray detections. The radio emissions spatial offset from the X-ray may indicate a disturbed cluster morphology (Mantz et al., 2018).

1.2.5 Radio Signatures from the Sunyaev Zeldovich Effect

The Sunyaev Zeldovich effect (Zeldovich and Sunyaev, 1969) is the alteration of cosmic microwave background (CMB) photons (Penzias and Wilson, 1965) when they pass through the hot, ionized plasma of the ICM. The cosmic microwave background was emitted by plasma early in the universe during recombination, when the early universe particles combined and formed neutral atoms. The CMB photons interact via inverse Compton scattering, where a photon and an electron interact, with momentum transferred to the incident photon, noticeably boosting its energy and subsequent frequency.

We know that the CMB is relatively homogeneous across the entire sky (Penzias and Wilson, 1965). In the direction of a galaxy cluster the photons have travelled through the hot ionized plasma of the cluster and emerged with higher energy (Sunyaev and Zeldovich, 1980). This shifts photons out of the range we expect from the CMB. As such, the difference in the integrated spectra of the uniform CMB and the cluster direction CMB appears as an apparent decrement in the CMB emission. This effect traces the energy and density of the ICM (Sunyaev and Zeldovich, 1980). A sample Sunyaev Zeldovich decrement is shown by the red contours in Fig. 1.1.

1.3 Properties of Cluster Components

1.3.1 Cluster Mass Distribution

The density over radius of a dark matter halo can be modelled as collisionless particles as described by Navarro et al. (1997) in three dimensions (Eq. 1.3) and projected onto two dimensions (Eq. 1.4).

$$\rho_{NFW}(r) = \frac{f_0}{x(1+x)^2}, x = \frac{r}{R_s} \tag{1.3}$$

$$\sigma_{NFW} = 2\int_R^\infty \rho_{NFW}(r) \cdot \frac{r}{(r^2 - R^2)} dr \tag{1.4}$$

The NFW surface density at radius r given by $\sigma_{NFW}(R)$ is the integrated NFW three dimensional profile (Navarro et al., 1997) $\rho_{NFW}(r)$ given in Eq. 1.3 with scale radius R_s and normalizing constant f_0. Though the dark matter halo of a galaxy cluster cannot be directly observed, it can be inferred from the luminous components of the cluster, as in the case of gravitational lensing (Bartelmann and Schneider, 2001). The growth of the dark matter halo of the Brightest Cluster Galaxy, or BCG, of a cluster is related to the growth of the mass of the cluster dark matter halo (Lavoie et al., 2016). Additionally, the galaxy density in a cluster is expected to roughly trace the dark matter density, as the galaxies behave similar to collisionless particles in a gravitational potential well, a fact which has been used to estimate the amount of dark matter in a galaxy cluster (Zwicky, 1933).

1.3.2 Cluster ICM Distribution

The baryonic plasma in the centres of galaxy clusters can be modelled according to a β model (Cavaliere and Fusco-Femiano, 1976). The β model assumes that the intracluster gas is in isothermal hydrostatic equilibrium. The dark matter mass distribution in this case was assumed to be distributed in a King (1962) profile, and the gravitation from that dark matter distribution is resisted by gas pressure. The number density of plasma particles over radius is then given by Eq. 1.5.

$$n_e(r) = n_{e,0}\left(1 + \frac{r}{r_c}^2\right)^{-3\beta/2} \tag{1.5}$$

Here, n_e is the electron number density at a radius r with a given core number density $n_{e,0}$, and scale radius r_c. The slope term is $\beta = \mu m_p \sigma_v^2 / k_B T$, where μ is the mean molecular mass, m_p is the mass of the proton, σ_v is the velocity dispersion of the gas particles, k_B is the Boltzmann constant, and T is the temperature of the plasma. The gas density profile of XLSSC 122 from Mantz et al. (2018) is shown in Fig. 1.2.

1.3.3 Cluster Redshift

One can infer the distance to, or redshift of, a cluster from its colour and spectral properties. The first method, by photometric redshift, relies on the combination of photometric bands to infer the redshift of the underlying spectral energy distribution. Some examples of acquiring cluster distance by photometric redshift can be found in Skelton et al. (2014). The second method is by spectroscopic redshift. The addition of spectroscopic information allows us to look at a range of wavelengths, and with the right resolution, identify known features and their resulting shift from their rest wavelengths, or expected wavelength of incidence. These observations are much more precise, but often more expensive to acquire. Some examples of acquiring distant cluster redshifts via spectroscopy can be found in Dressler (1980); Newman et al. (2014) and Willis et al. (2020). The spectroscopic method, though more time consuming, is far more accurate and preferred over a photometric redshift estimate.

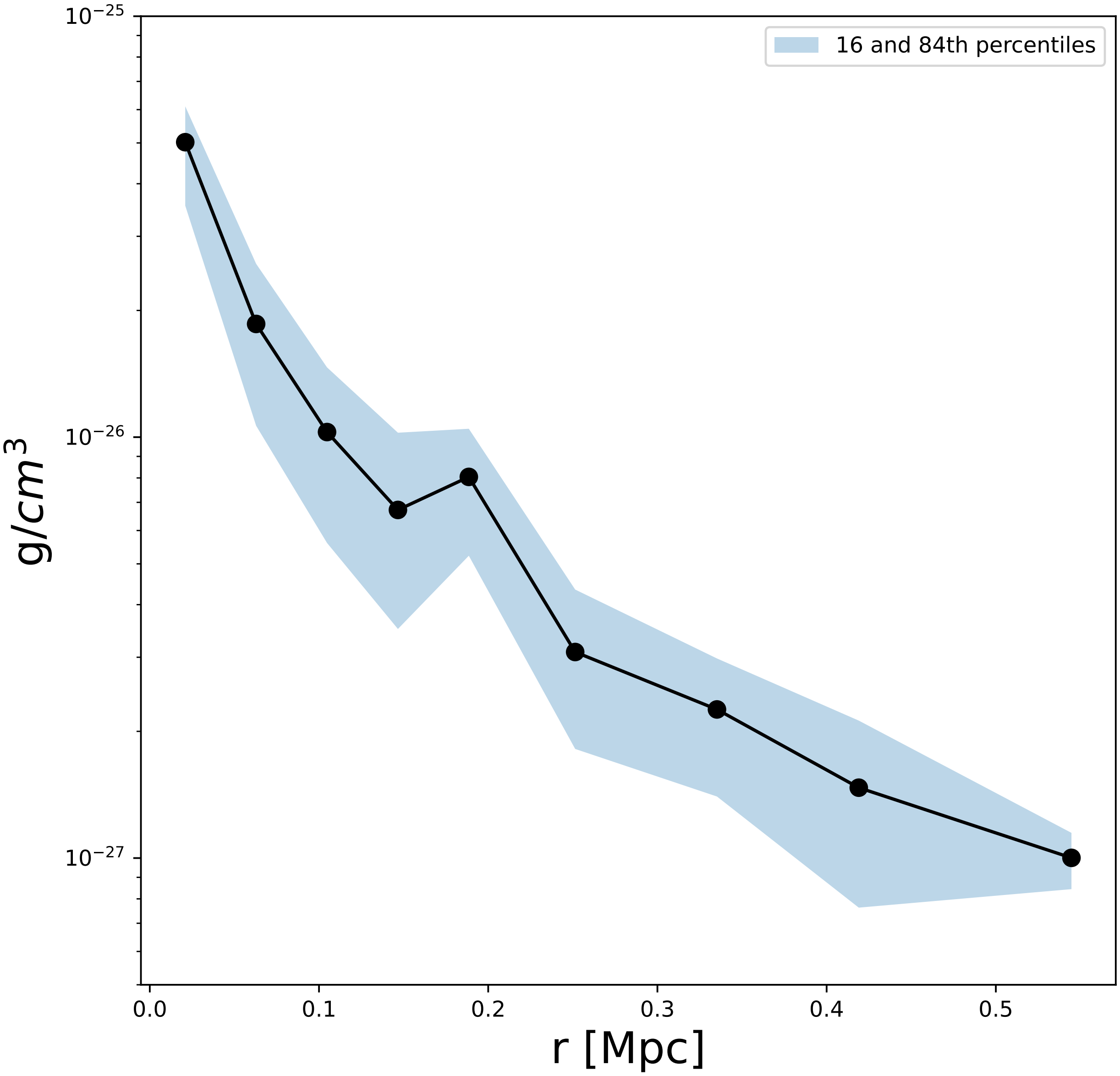

Figure 1.2: The ICM gas density from (Mantz et al., 2018) with 16th and 84th percentiles over distance from cluster centre. This profile was formed from the PN, MOS1, and MOS2 detectors on the EPIC instrument on the XMM Newton space telescope. The final clean exposure time in each instrument was about 70 ks.

1.3.4 Luminosity and Stellar Mass Functions

The number of galaxies at different masses or luminosities in a galaxy cluster member population traces the evolution of galaxies from low to high mass. This relation allows one to see the highest achieved luminosity, the buildup to most common luminosity, and the shape of the low luminosity galaxy slope. The luminosity function of a galaxy has been found to satisfy a Schechter (1976) profile, given in Eq. 1.6. One can convert between luminosity and mass by noting the mass to light ratio in galaxies of a specific colour.

$$\Phi(M_i) = \Phi_0 \cdot (10^{0.4(M-M_i)}))^{\alpha+1} \cdot \exp(-10^{0.4\cdot(M-M_i)}) \tag{1.6}$$

Here, M is the scale magnitude, Φ_0 is a normalizing factor, and α is the dim slope. Galaxies acquire more stellar mass through a variety of processes including the accretion of star forming material, interactions between the ICM and the galaxy, as well as interactions between galaxies. The resulting luminosity distribution could provide a tracer of galaxy evolution and interaction, with different proportions of low to high mass galaxies based on different quenching and mass acquisition processes. In galaxy clusters, where the mass growth of galaxies is higher, the characteristic luminosity is higher. In the field, the luminosity function appears to have a flatter slope than in clusters, which have an abundance of lower mass galaxies (Muzzin et al., 2013). In the early universe, the faint end slope of the red sequence luminosity function appears to be flatter in clusters, approaching $\alpha = 0$. Between $z = 1.15$ and $z = 0.6$, α decreases from -0.5 to -1 (Chan et al., 2019). For a cluster at $z = 0.83$, the red galaxy population fits to a high slope of $\alpha \approx -0.1$ (Goto et al., 2005), though that cluster appears to have not evolved low mass red galaxies in high numbers at that time. Alternatively, the UV galaxy luminosity function α parameter appears to have increased from -2 at $z = 8$, to -1.5 at z = 1 (Parsa et al., 2016). In essence, lower mass blue galaxies are turning red as the universe ages. For clusters at $z = 1.5$, van der Burg et al. (2018) find $\alpha \approx -0.2$ for their sample. They also find that the relative mass distributions between cluster and field are more similar than their local universe control. For comparison, initial studies of the Virgo Cluster place the low mass slope of a fit to it's elliptical members to be ≈ -1.4 (Sandage et al., 1985; Ferrarese et al., 2016), a steep slope also seen with SDSS (McDonald et al., 2009), and in the local universe out to intermediate redshifts. The behaviour of the luminosity function's outer slope can be extreme, as the slope is sensitive to changes in cluster type, size, spectroscopic incompleteness, etc. At high redshift however, the dim slope is closer to $\alpha = 0$. Example profiles with varying α parameter are shown in Fig. 1.3. It appears that in galaxy clusters, the α slope for the red sequence is lower, leading to a larger proportion of red galaxies at low mass compared to the field.

1.3.5 Colour Bimodality

The cluster galaxy population is broadly bimodal in colour (Butcher and Oemler, 1984; Baldry et al., 2006; Urquhart et al., 2010) and manifests approximately as 2 Gaussians in colour space, with the fraction of red galaxies increasing with cluster mass density (Balogh et al., 2004). Due to this quiescent galaxy dominance and the hot ICM, clusters are observed as regions with an overdensity of massive red galaxies (Dressler, 1980; Hogg et al., 2003; Gladders and Yee, 2000; Rykoff et al., 2014; Strazzullo et al., 2015) and extended X-ray emission (Newman et al., 2014; Gobat et al., 2011).

The strength of star formation cessation can be traced by the relative number of red and blue galaxies (red fraction). This red fraction can be used to compare the effect of environmental density on the star formation history of galaxies (Balogh et al., 2016), and has been used as strong indication of quenching activity (Willis et al., 2013; Strazzullo et al., 2016; Rykoff et al., 2014). As such, the change in red fraction over regions of varying density probes the prominence of cluster environments on the quenching of their member galaxies (Raichoor and Andreon, 2012).

Galaxies which have recently undergone a rapid quenching event can show signs of their recent star formation into their red and quiescent stage (Poggianti et al., 1999); such galaxies are labelled as post-starburst. Quenched galaxies will retain their blue stars whose signatures one uses to estimate star formation rate. In the period between the decay of the most massive stars and the dominance of red stars in the surviving stellar population of a quenched galaxy, there is a period of time when the intermediate mass A type stars are the most massive stars in a galaxy. These A type stars exist in sufficient number to be noticeable in the spectra of a recently star forming galaxy (Paccagnella et al., 2017). A characteristic feature of A-type stars is their strong Balmer absorption lines, $H_\alpha, H_\beta, H_\gamma$, etc. Thus, one can observe recently quenched galaxies by looking for strong Balmer absorption, with a shortage of star formation emission lines such as $O[III]$ from active star formation and the presence of O and B type stars. These galaxies are often called post starburst because the strongest absorption features would be those detected right after a strong burst of star formation which has been cut short, amplifying those post-starburst features. In cluster environments, the incidence rate of post-starburst galaxies is higher than the field (Poggianti et al., 2009) at least out to intermediate redshifts of $z = 0.4$ (Werle et al., 2022).

The colour bimodality in a galaxy cluster separates these galaxies into two groups, the

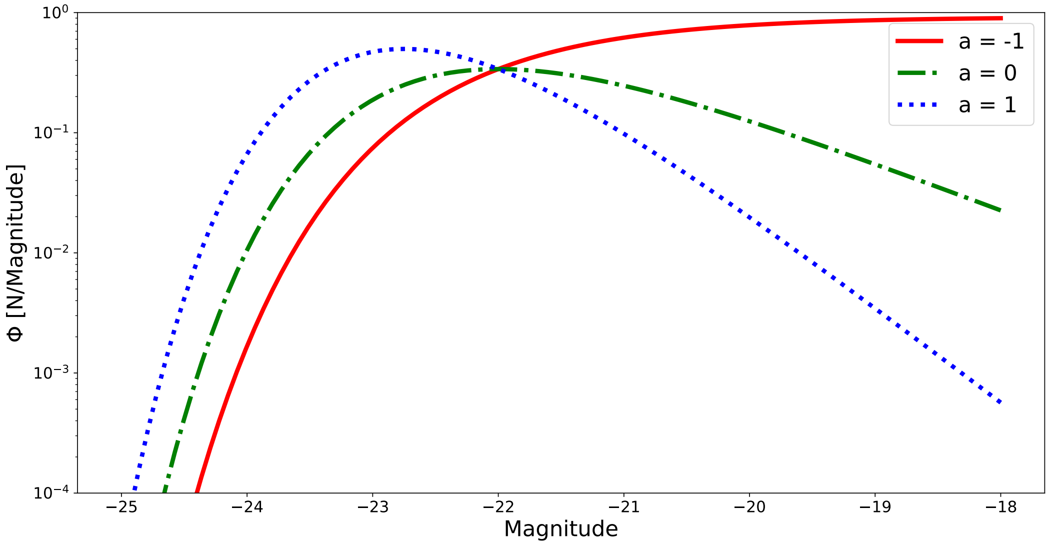

Figure 1.3: Example Schecter (Schechter, 1976) functions with $M_* =$ -22 and $\Phi_0 = 1$. Three plots are shown with varying α parameters, $\alpha = -1$ (blue dotted), $\alpha = 0$ (green dot-dash), and $\alpha = -1$ (red solid).

red sequence and the blue cloud, so named because the red sequence is a fairly tight relation, and the blue cloud has a higher colour scatter. In this context, colour separates galaxies based primarily on their star formation history. Red galaxies emit a much larger portion of their light from older, redder, longer lived stars, with very little recent star formation. On the other hand, blue galaxies emit more light from younger, bluer, shorter lived stars. The initial blue light signature from a young galaxy changes as the more massive and hotter (bluer) stars explode, it is then the time since star formation which determines the remaining population of stars. Red galaxies tend to be located along a tight colour magnitude relation with low scatter and evolving with redshift out to $z = 1$ (Bell et al., 2004), they form a distinctive overdensity in colour magnitude space. Since the galaxies in a cluster have the same redshift, assigning membership within this red sequence at a given redshift can help find the cluster members from a previously identified cluster or identify a galaxy cluster from a prominent red sequence (Rykoff et al., 2014; Gladders and Yee, 2000, 2005).

1.4 Ram Pressure Stripping and Other Quenching Mechanisms

Quenching mechanisms can be broadly divided between mass quenching and environmental quenching (Peng et al., 2010; Kawinwanichakij et al., 2017). Quenching mechanisms due to a galaxy's mass include either a rapid consumption of the gas content due to star formation (McGee et al., 2009), or the heating and removal of gas in the galaxy due to the feedback from active galactic nuclei (AGN Circosta et al. (2018)). Environmental quenching occurs when galaxies interact with other galaxies, causing a removal of gas due to near interaction, or harassment (Moore et al., 1996). The quenching mechanism of most interest to us in the study of dense cluster environments is the interaction between the galaxy and the hot plasma ICM, known as ram pressure stripping (Gunn and Gott, 1972). When a galaxy enters a cluster environment, passing through its ICM, one occasionally observes a compression and expulsion of gas from the galaxy (Werle et al., 2022). This initial pressure can remove the gas reservoir necessary for star formation (Brown et al., 2017). The galaxy at this point may quench rapidly due to the consumption and removal of gas viable for star formation (McGee et al., 2014). Ram pressure stripping shapes the evolution of galaxies in dense cluster environments, altering morphology, colour, and gas properties (Boselli et al., 2022). Ram pressure stripped, and other fast quenched galaxies may appear as post-starburst galaxies (Poggianti et al., 1999; Paccagnella et al., 2017). By tracing their incidence over radius one can work backwards to estimate whether a prior ram pressure force could explain the distribution of post-starburst features (Reynolds et al., 2021).

Galaxies in regions with a hot, dense ICM, such as a cluster environment, have a higher rate of quenching than low density regions (Baldry et al., 2006; Peng et al., 2012). At higher cluster masses, ram pressure stripping is more effective, scaling with both ICM density and infall velocity (Gunn and Gott, 1972; McCarthy et al., 2008), with both higher in more massive cluster environments. A massive cluster is also located at the intersection of a greater number of filaments of the cosmic web (Bond et al., 1996). Just as a galaxy in a cluster is quenched, a locally overdense region such as a filament could quench or partially quench the galaxies, reducing their gas supply upon reaching the cluster. Comparing the evolution of galaxies has revealed a difference in quenching mechanisms over time. In the local universe, environmental quenching (Gunn and Gott, 1972; Balogh et al., 2000) has been observed as the dominant quenching mechanism (Darvish et al., 2016; Peng et al., 2010) in galaxy clusters, where galaxies quench at a rate different from that expected from their mass.

Galaxies in some of the few distant clusters observed still possess old stellar populations (Willis et al., 2020; Trudeau et al., 2024; Strazzullo et al., 2016; Webb et al., 2020) despite existing in an era with high average star formation (Madau and Dickinson, 2014). However, acquiring large samples of galaxy clusters at high redshift has proven difficult (van der Wel et al., 2004; Gobat et al., 2008). Additionally, the concept of a cluster is less clearly defined at earlier times. The progenitors of today's massive clusters such as Virgo and Coma are predicted to exist at $z = 2$ as clusters which are a small fraction of that mass (Chiang et al., 2013). If one identifies a hot ICM they can associate infalling galaxies with an overdense region on which they can quench. With the environment constrained, one can compare the relative quenched fraction across radius to determine how the ICM density affects quenching.

Pushing our observations of quenching in cluster environments into the early universe probes a region past where the dominant quenching mechanism appears to shift (Balogh et al., 2016; Trudeau et al., 2024). Recently, the GOGREEN survey has conducted an extensive study on galaxies from $z = 1$ to $z = 1.5$ (Balogh et al., 2017), finding that the quenching mechanism in galaxies at $z > 1$ is more difficult to explain with environment dominated quenching as seen in local universe galaxies, implying an early mass based quenching (Webb et al., 2020). Notably, massive quenched galaxies appear to quench earlier, at $z > 2$, possibly during a pre-infall stage. This is counteracted by a larger sample of lower mass galaxies rapidly quenching due to the dense environment during infall (McNab et al., 2021). This time scale roughly aligns to other observational evidence of a change in quenching mechanism at $z = 1.5$ (Nantais et al., 2017), showing an increase in the strength of environmental quenching they attribute to an increase in ICM density at this time.

Effectively, the local universe has a fairly consistent quenching due to the environment which is independent of galaxy mass (Baldry et al., 2006; Peng et al., 2010; van der Burg et al., 2018). This consistent quenching is not observed in the early universe. It appears that, in distant clusters, higher mass galaxies quench with greater efficiency (Reeves et al., 2021). This could be explained by a dominance of a mass quenching mechanism over environmental quenching. In fact, when observing a greater sample of galaxies from $z = 1.2$ to $z = 0.7$, it appears that the environmental quenching efficiency is relatively constant for galaxies of $log(\frac{<M_*>}{M_\odot}) > 10.26$ (Lemaux et al., 2019). This implies that environmental quenching of low mass galaxies drives the change in dominant quenching mechanism, not an increased quenching efficiency of high mass galaxies, as seen at $z < 0.5$ (Hou et al., 2013). In a more recent study with a larger sample size, it seems that the impact of environmental quenching may only start to dominate at $z < 1.5$ (Trudeau et al., 2024). Though the exact time frame where the dominant quenching mechanism shifts is unknown, what one can see is that galaxy clusters in the early universe appear to experience quenching primarily through mass enhancement, rather than through their environment.

Galaxies in the local universe have had more time to relax, accrete more mass, and heat the ICM, providing an environment readily able to quench through ram pressure stripping or galaxy galaxy interaction, as seen in the presence of post starburst, stripped, galaxies in local clusters (Brown et al., 2017; Watts et al., 2023; Brown et al., 2023). By observing galaxy clusters in the early universe of a similar ICM temperature and density, one can test to see if the observed variation in dominant quenching mechanisms is due to the natural evolution of a galaxy cluster, or due to an effect external to the cluster's composition. The observed mass quenching could be caused by pre-infall processing for example (Fujita, 2004; Li et al., 2012).

The identification of ram pressure stripped galaxies has been conducted morphologically from the local universe (Abramson et al., 2016; Boselli et al., 2016; Poggianti et al., 2017) out to intermediate redshifts (McPartland et al., 2016; Moretti et al., 2022; Boselli et al., 2019; Moretti et al., 2022). Finding ram pressure stripped galaxies by morphology relies on the identification of compressed edges or trailing tails indicative of a stripped galaxy. In these circumstances, long trails of ionized gas have been detected in the trailing edges of galaxies entering into a cluster environment (Boselli et al., 2016), as seen in Fig. 1.4. Additionally, the velocity of ram pressure stripped galaxies in their cluster environments exceeds 1000 km/s for those galaxies with stripping in their interior regions, with local ICM densities of $10^{-3}\,\mathrm{cm}^{-3}$ (McPartland et al., 2016). With the ram pressure scaling with density and the square of infall velocity, galaxies found near cluster centres tend to have more dramatically stripped tails (Jaffé et al., 2018). These galaxies likely have infall pathways which take them directly to the cluster centre, where the gas is most dense. Additionally, simulations show that galaxies in overdense infall regions, such as a filament, experience up to 100 times the ram pressure at the same radius as galaxies infalling outside of a filament (Bahé et al., 2013).

Using the treatment of Ram Pressure Stripping from Gunn and Gott (1972), as applied to an isothermal sphere (McCarthy et al., 2008), one obtains an analytic equation which has the form.

$$\rho_{ICM} v_{orb}^2 \geq \frac{\pi}{2} \frac{G M_{gal(R)} \rho_{gas}(R)}{R} \tag{1.7}$$

Here, ρ_{ICM} is the ICM density, v_{orb} is the velocity of the orbiting galaxy, G is the gravitational constant, $M_{gal}(R)$ is the mass of the galaxy contained within galactic central radius R, with a gaseous component at that radius of $\rho_{gas}(R)$. If this condition is met, then gas at a radius of R will experience a ram pressure stronger than the gravitational binding force from the galaxy. Under this treatment, ram pressure strips from outside to in (Boselli et al., 2019; Brown et al., 2023), removing hot gas first and cold gas at later times (Jaffé et al., 2018). Stripping of gas in the central regions of a galaxy indicates a strongly ram pressure stripped galaxy with the visual indications of recent quenching (Brown et al., 2017).

The exact interaction between the high energy cluster environment and their member galaxies at $z > 1.5$ is still an active area of study (Trudeau et al., 2024; Strazzullo et al., 2010). Investigating this interaction requires observing infalling galaxies in a cluster with a measured ICM density over radius.

1.5 General Properties of Galaxies

1.5.1 Mass distributions

The dark matter distribution in a single galaxy is similar to that in a galaxy cluster, in that it can be described by a NFW profile. However, the distribution of stars and gas in a galaxy can differ based on that in a cluster. Galaxies have a much broader range of morphological types, be that irregular, elliptical, or spiral (Hubble, 1926). One model describing the distribution of stars in a galaxy is the Sersic Profile given in Eq. 1.8 from Sersic (1968) and Graham and Driver (2005).

$$I(R) = I_e \exp\left\{ -b_n \left[\left(\frac{R}{R_e} \right)^{1/n} - 1 \right] \right\} \tag{1.8}$$

Here, I_e is the stellar light intensity at the effective radius R_e, n is the Sersic index describing how the slope of the distribution changes, and b_n is a normalization factor based on n. The distribution of gas in a galaxy is complex and multi-phasic, encompassing a

Figure 1.4: A false colour image of NGC 4569. Blue and green are CFHT MegaCam NGVS g and i band, red is $H_\alpha + [NII]$ narrow band. Adapted from Boselli et al. (2016)

variety of ionization levels, temperatures, densities, and atomic compositions. The most prevalent component is that of atomic hydrogen in the interstellar medium, or ISM. The distribution of the atomic hydrogen in a late type galaxy galaxy can be approximated by a simple exponential falloff given in Eq. 1.9 (Freeman, 1970).

$$n(R) = n_0 \exp\left(-\frac{R}{R_c}\right) \tag{1.9}$$

Here, n_0 is a peak particle number density, n(R) is the particle density at a radius from galaxy centre R, with a given scale radius R_c. More complex models of the gas dynamics do exist, and this is a simple case (Binney and Tremaine, 1987). I have modelled the star and dark matter mass growth over radius using the aforementioned models in Fig. 1.5. The stellar component is mostly contained within 10 kpc, whereas the dark matter halo extends much farther. This extended distribution of dark matter has been observed in local universe galaxies as the motion of material at the far edges of a galaxy do not appear to correspond to the gravitational attraction of its stellar component (Rubin et al., 1980).

1.6 XLSSC 122

Distant galaxy clusters identified through defined physical criteria offer an important opportunity to contribute to our knowledge of star formation and cessation in the early universe. In this context the discovery of XLSSC 122 as a $z = 1.98$ galaxy cluster discovered through the XMM-Newton Large Scale Structure Survey (XMM-LSS) (Willis et al., 2013, 2020) through thermal Bremsstrahlung X-ray emission (Mantz et al., 2014) and further supported by the detection of a Sunyaev Zeldovich decrement radio detection (Mantz et al., 2018), provides a prime example of such a distant cluster. The galaxies of XLSSC 122 were imaged under the Hubble Space Telescope cycle 25 (GO-15267, PI Rebecca Canning), with a spectroscopic identification of 37 cluster members (Willis et al., 2020), with 20 quenched galaxies (Noordeh et al., 2021) Fig. 1.6 shows a 3 colour image of the cluster core with the X-ray contours from Mantz et al. (2018). The observed temperature of XLSSC 122's ICM is $kT = 5 \pm 0.7\,\mathrm{keV}$, similar to the temperature of the Virgo cluster in the local universe, and will likely evolve into a similar mass as Virgo by $z = 0$ (Chiang et al., 2013). The morphology (Leste et al., 2024), dark matter halo history and star formation history (Trudeau et al., 2022) have been studied for the cluster core using previous HST cycle 25 observations. The star formation histories of these galaxies appear to extend into the very first Gyrs of the universe, as seen in Trudeau et al. (2022). Such quenched galaxies in cluster environments have been observed elsewhere at $z \approx 3.5 - 4$, with indications of rapid quenching in their star formation histories

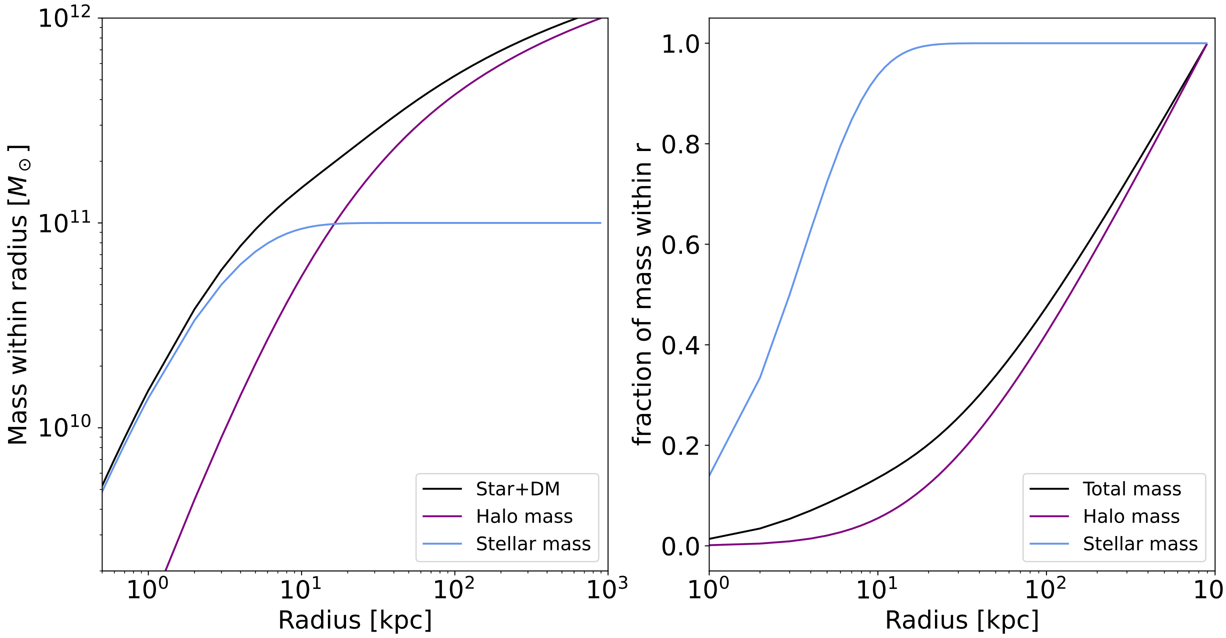

Figure 1.5: *left*: The mass contained within a radius R from a Sersic (Sersic, 1968) ($R_e =$ 3 kpc,n=1.5) stellar disk and a NFW (Navarro et al., 1997) ($R_s = 10$ kpc) dark matter profile for $log(\left(\frac{M_*}{M_\odot}\right) = 11$ and $log(\left(\frac{M_h}{M_\odot}\right) = 12$. *right*: The same as the left, but normalized by the integrated mass in each component.

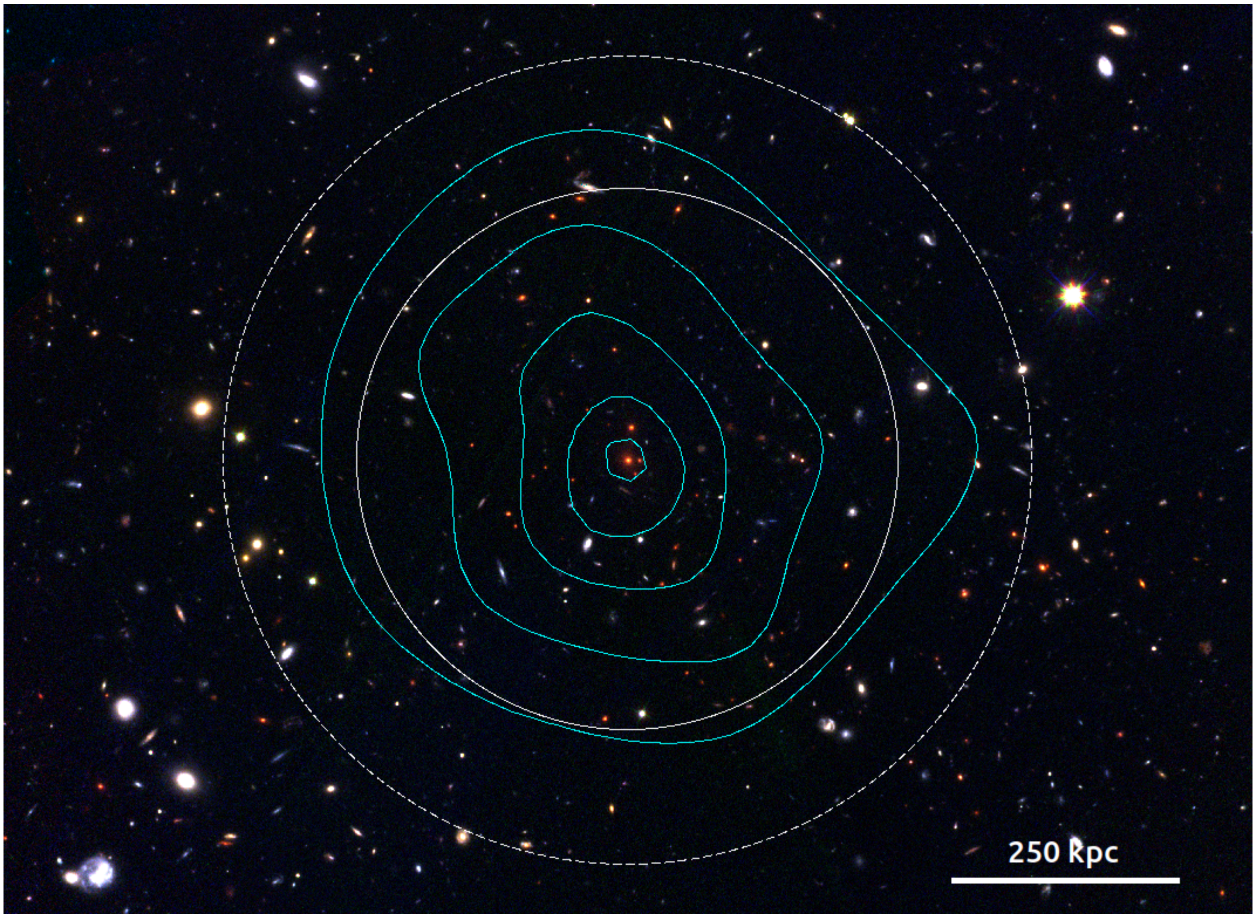

Figure 1.6: A 3 color image of XLSSC122, r,g,b = F140W, F105W, F814W. Central red large galaxy is the BCG, id = 313. Cyan contours are X-ray contours from (Mantz et al., 2018), The solid white line is $R_{500} = 295kpc$, the dashed white line is $R_{200} = 440kpc$.

(Valentino et al., 2020).

1.7 Thesis Summary

With new cycle 30 (GO-17172, PI Rebecca Canning) data from the Hubble Space Telescope, the outer regions of the galaxy cluster XLSSC 122 have been observed for the first time. My work focuses on the reduction and analysis of this data. I have doubled the detected number of galaxies in XLSSC 122. Additionally, I have identified post-starburst galaxies, and there is a peak in post-starburst feature galaxies near the cluster virial radius. This increase in post-starburst features occurs with an increase in the proportion of red galaxies. This appears to indicate that galaxies falling into XlSSC 122 are experiencing rapid quenching as they hit the intracluster medium. I also trace the galaxy number density as a function of clustercentric radius, and compare them to a fitted double power law and an NFW profile, finding a good fit to the former. I probe the spectroscopic incompleteness of red galaxies in XLSSC 122, and use this to estimate a luminosity function for XLSSC 122 red galaxies. Expanding the search of cluster members out to the outskirts of this cluster has yielded no significant overdensities in the observation footprint indicative of an infalling structure.

This thesis is split into two major parts. Chapter 2 covers the creation of a photometric catalogue of spectroscopically identified cluster members in the galaxy cluster XLSSC 122. Chapter 3 covers the initial analysis of the cluster member properties over clustercentric radius. Chapter 4 provides a summary and discussion of future work using this dataset, along with potential sources of uncertainty in the analysis.

1.8 Cosmology

In this work I assume a flat ΛCDM cosmology with $H_0 = 69.32\,\mathrm{km\,s^{-1}\,Mpc^{-1}}$, $\Omega_\mathrm{m} = 0.286$, and $\Omega_\Lambda = 0.714$ from Bennett et al. (2013). Magnitudes are expressed using the AB magnitude system.

Chapter 2

Catalogue

In this chapter I cover the calibration and photometry of the cycle 25 and 30 data from the Hubble Space Telescope (HST) for the galaxy cluster XLSSC 122. This involves the conversion of raw exposure images into calibrated images, the alignment and stacking of those images into mosaics based on filter, and the extraction of position and aperture matched photometry from those mosaics. I perform a spectroscopic reduction of the G141 grism data to identify cluster members. Classifications are conducted by fitting a set of models to extract redshift and key line absorption and emission features. The photometric extractions are then associated with the spectroscopic classification of post-starburst features and cluster membership. I compare the resulting catalogues with those of Willis et al. (2020) and find good agreement between extracted luminosities, colours, and sizes. The total number of cluster members identified in this catalogue is doubled to 74 galaxies from 37 previously identified in the cluster core. Spectroscopic incompleteness is considered and modelled with the creation of mock G141 two dimensional spectra. A diagram of the pipeline from raw data to spectroscopic catalogue is shown in Fig. 2.1.

2.1 Observations with the Hubble Space Telescope

This work builds off of data by Jon Willis and a 2017-2018 observation using the Hubble Space Telescope (HST, Willis et al., 2020). This data was obtained in cycle 25 using the F105W, F140W and G141 filters on the Wide Field Camera 3 (WFC3) IR instrument under HST-GO-15267. This present work includes the addition of data from HST cycle 30 using the F105W, F140W, G141, and F814W filters from the HST-WFC3 IR and HST/ACS instruments under HST-GO-17172. These pointings were obtained for target areas spanning out to 8 times the virial ($R_{200} = 295\,\mathrm{kpc}$) radius of the cluster as measured from the X-ray profile from Mantz et al. (2018). In total, these observations cover 9 fields, with the F814W

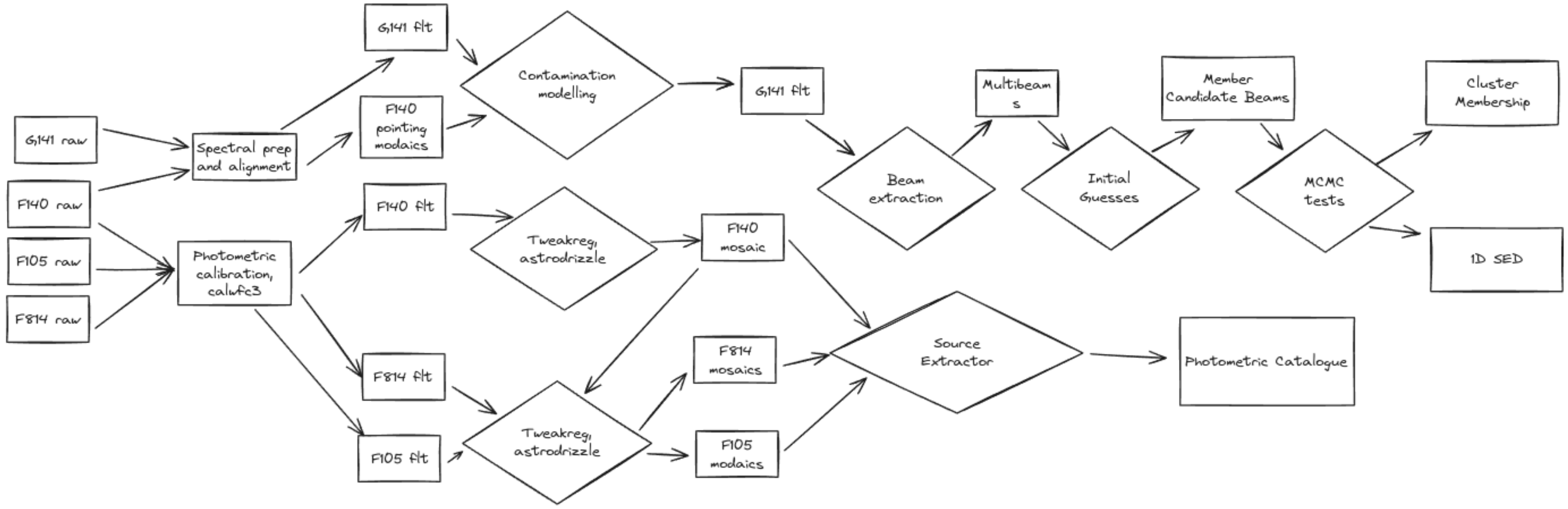

Figure 2.1: The spectroscopic pipeline steps taken to acquire a photometric catalogue of cluster members from the raw HST observations.

Target	RA [deg]	DEC [deg]	Cycle	G141EXP (s)	F105WEXP (s)	F140WEXP (s)	F814EXP^a (s)
Core	34.4341	-3.7587	25	26540	2611	5170	0
NE	34.4619	-3.7432	30	0	4235	0	3856
SE	34.4619	-3.7764	30	4011	4235	1011	7998
NW	34.4094	-3.7432	30	8023	4235	2023	12140
SW	34.4094	-3.7764	30	8023	4235	2023	12140
NE-Far	34.4535	-3.7438	30	3808	0	1011	4264
SE-Far	34.4535	-3.7770	30	3911	0	1011	4264
NW-Far	34.4178	-3.7438	30	4011	0	1011	4264
SW-Far	34.4178	-3.7770	30	4011	0	1011	4264

^{a}F814W exposures are offset from their target RA and DEC

Table 2.1: Details of the location, cycle, and filter exposure times from the HST cycle 25 and 30 observations of XLSSC 122. Target names are shortened and paraphrased from their original full target names.

band UVIS exposures taken in parallel imaging mode to overlap with the F140W and F105W IR exposures. These regions cover the centre of the cluster, 4 side regions, and 4 farther regions along the same axis as seen in Fig. 2.2. These observations provide spectroscopic and photometric data in at least 1 band for all fields as seen in Table 2.1. In this work I use both cycles together from raw to avoid biases present in different data reduction decisions.

The F140W filter is a photometric wide filter centred on 13923 Å with a width of 3840 Å (Dressel, 2021). For a galaxy at $z = 1.98$, it covers the rest frame 4000 to 5300 Å range, framing the low energy, red side of the 4000 Å break. The F105W filter is a photometric wide filter centred on 10552 Å with a width of 2650 Å (Dressel, 2021). For a galaxy at $z = 1.98$, it covers the rest frame 3000 to 4000 Å range, framing the high energy, blue side of the 4000 Å break. Together, these two filters are excellent at framing the colour bimodality of galaxies in XLSSC 122, as seen in Noordeh et al. (2021). These two filters are a part of the WFC3 instrument's IR channel, which collects the filtered light onto a charge coupled device (CCD), converting photons into electrons which can be read by the instrument. The pixel scale of the IR CCD is $0.135'' \times 0.121''$, across 1014×1014 pixels, with a field of view of $136'' \times 123''$ (Dressel, 2021). At $z = 1.98$, this corresponds with a field of view of 1150 kpc × 1050 kpc. An object with a width of 20 kpc would be spanned by 2-3 pixels. This resolution allows a morphological extraction from these galaxies, as seen in Leste et al. (2024).

The F814W filter is a photometric wide filter centred on 8333 Å with a width of 2511 Å(Stark, 2024). It covers the rest frame 2400 Å to 3217 Å range, framing the UV light from young stars in the galaxy. The addition of the F814W filter improves coverage of young stars, and therefore bluer galaxies. At this era, $z = 2$, the star formation rate in the universe is high, and young stars are present in abundance (Madau and Dickinson, 2014). The outer edges of a cluster are expected to host a large number of blue galaxies, well suited for the

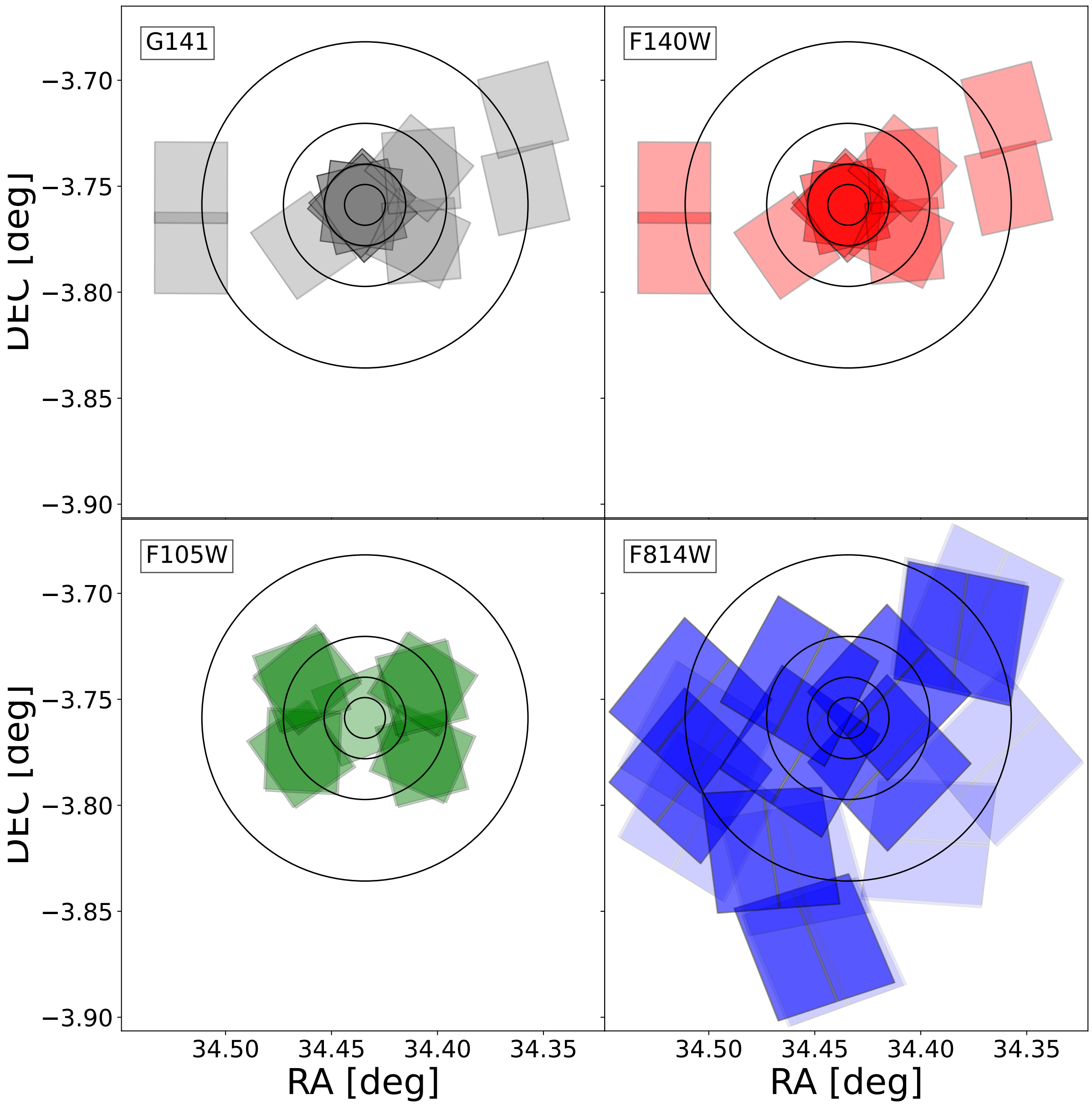

Figure 2.2: A map of the exposure area of the HST data used in this paper from cycles 25 and 30. Higher opacity indicates a greater number of exposures. G141 and F140W are missing exposures due to a failure to acquire guide stars in some targets. The concentric circles are centred on the centre of XLSSC 122, with radii of R_{500}, $2R_{500}$, $4R_{500}$, and $8R_{500}$

F814W filter. The ACS instrument hosting the F814W filter has multiple CCDs, $202'' \times 202''$ spread across 2 detectors of size 2048×4096 pixels, with a scale of $0.05'' \times 0.05''$ per pixel. This higher resolution using the F814W filter could be used in morphological analysis of the cluster members.

The G141 grism filter is a spectroscopic filter in the WFC3 IR channel. It has a wavelength range of 10750 Å to 17000 Å with a dispersion of 46.5 Å per pixel and a low spectral resolution of 130 at 14000 Å. The G141 grism fits between the ranges of F140W and F105W, covering the rest frame 4000 Å break as it stretches from 3600 Å to 5700 Å in the rest frame of a $z = 1.98$ galaxy. The G141 grism can be used to identify a strong 4000 Å break, along with the [OIII], H_β, H_δ, and H_γ lines to determine the redshift of the galaxy.

2.2 WFC3-IR/ACS-UVIS Calibration Pipeline

The F105W, F140W, and F814W images were processed using the Calwf3 reduction pipeline through the Grizli (Brammer, 2019) software wrapper. The reduction included bias subtraction, dark current subtraction, flat field and gain correction, cosmic ray rejection, and a non-linearity correction. The images were inspected between each reduction step, and default parameters were used to create the calibrated .flt images and weight maps.

The data from the IR instrument underwent a series of calibration steps to account for instrument and environmental effects. The header information used in Calwf3 (Dressel, 2021) allows one to toggle the individual calibration steps. I describe these steps, and the corresponding keywords, below.

2.2.1 Data Quality and Initialization

Before running any calibration step, a list of bad pixels for the detector is loaded and ordered by severity. This happens in the DQICORR step.

2.2.2 Bias and Gain Removal

Every pixel on the IR chip of WFC3 is given a bias to prime the quantum wells of the CCD. This creates a charge into which electrons enter and become trapped. Without this bias, the CCD would be inefficient at low photon counts. With a bias, when photons photoelectrically generate electrons, they are collected efficiently in the quantum well of the CCD pixels. In order to remove bias, a short period of the observation is taken at the start of the exposure, during which the primary source of signal is due to the bias itself. For the HST this exposure is about 2.9 seconds. Information taken from the zero read during the ZSIGCORR step is stored for later use. Subtracting this biased zero-read from the resulting exposure reduces the effect of the bias on the resulting counts. This happens in the BLEVCORR step.

The IR instrument is made out of a CCD with 4 quadrants, each quadrant has a unique scaling between incoming photons and output count number. This is well known for each quadrant, and can be removed by scaling the gain of each quadrant to a single value. This is done in the ZOFFCOR step.

The ACS instrument, for which I have the F814W filter, uses a similar reduction pipeline (Lucas and Ryon, 2022; Stark, 2024), but has a few differences. The ACS instrument lacks intermediate readouts over an exposure, and typically captures a larger number of cosmic rays, thus the ACS reduction pipeline relies more on the drizzling stage to remove cosmic rays. ACS also has a specific bias frame as reference for each file, instead of the zero read in WFC3.

2.2.3 Non-Linearity Correction

As a pixel fills with electrons over time, the chance decreases that an electron excited by a passing photon stays within the well. As such, the relationship between photons hitting the detector and stored electrons is non-linear. In the NLINCORR, saturated pixels are flagged and corrected, as the decrease in electrons as the pixel approaches saturation is well known. In the case of very high saturation, it is very difficult to reproduce the incident photon count, and a correction is far less accurate. In these cases the pixels are marked as highly saturated.

2.2.4 Dark Current Subtraction

A variety of objects, including the instrument itself deliver a low, but noticeable, number of photons which need to be corrected and removed to better observe distant objects. To estimate this effect, a set of dark images are taken, usually corresponding roughly to the exposure time of the file under calibration. The dark file is scaled and subtracted from the primary image in the DARKCORR step. The PHOTCORR step after this alters the header information of the files with the relevant information to convert between the data in the image and absolute fluxes. The UNITCORR step then converts the data in the image into counts per second, rather than total counts.

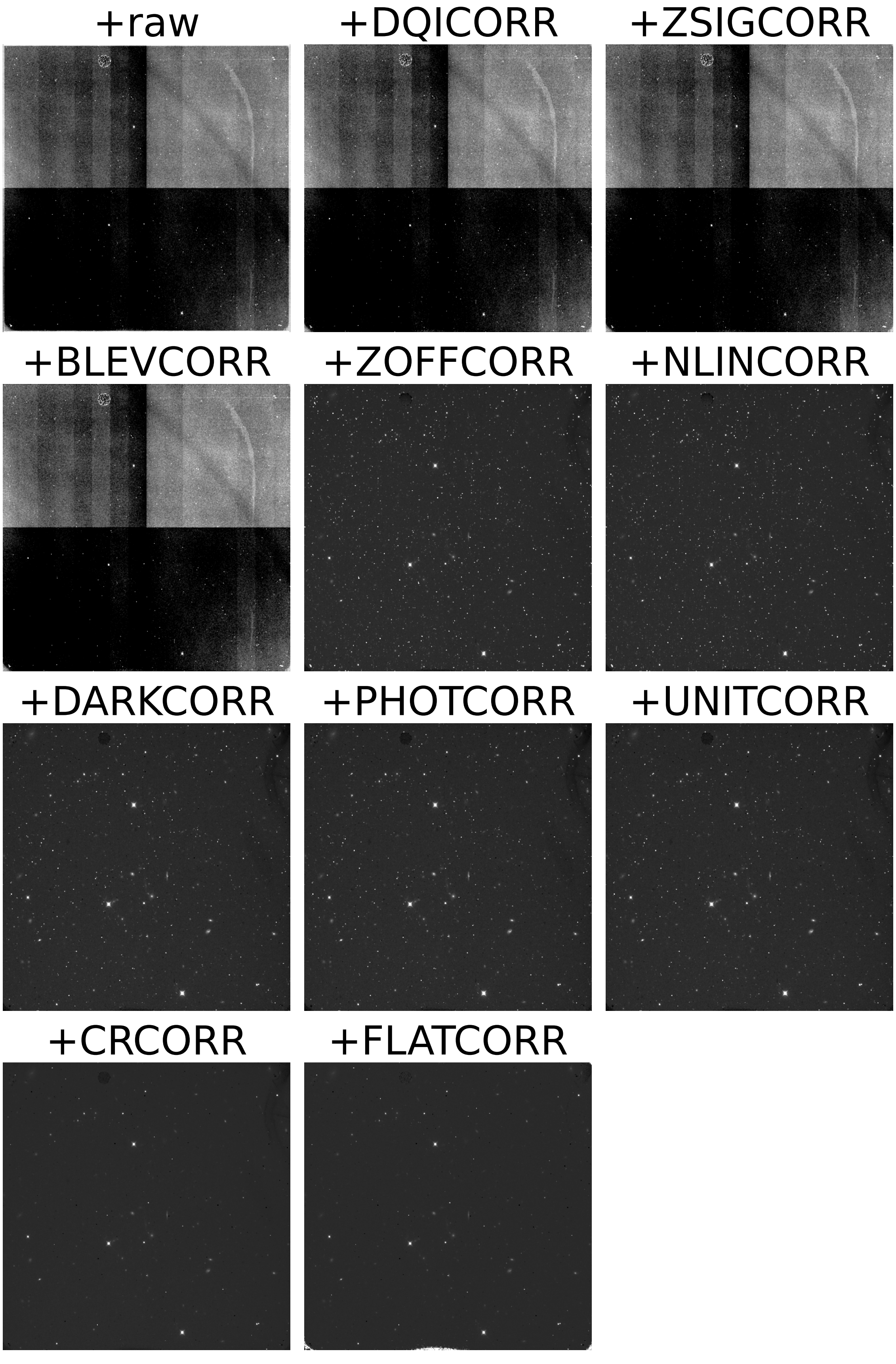

Figure 2.3: The intermediate images in the IR calibration pipeline, from raw to final image used in the drizzling stage.

2.2.5 Cosmic Ray Rejection

There are particles in space from distant objects which are not photons, but travel near the speed of light. These high energy particles, or cosmic rays, pass through the CCD and massively excite the wells, throwing off the steady counting of photons over the exposure. These cosmic rays can be found by looking at pixels which have rapidly increased in accumulated charge over time on the ramps, or those which are incredibly saturated with no obvious massive luminous object nearby. Cosmic rays are accounted for in the creation of a dithering pattern, which covers the same region with multiple pixels at different times. This way, a cosmic ray could hit a pixel during one exposure, and be absent in the other 3. The cosmic ray removal is handled in the CRCORR step.

2.2.6 Flat Field Correction

The pixels of a CCD, even after all of these steps, still behave differently when photons interact with them. To account for the pixel-to-pixel and large scale variation across the detector one takes a flat field. A flat field is effectively a uniformly illuminated exposure, where any observed pixel to pixel variations can then be attributed to detector based effects and corrected. This step is handled in the FLATCORR stage. The final, calibrated image, example in Fig. 2.4 is then ready for combination into a larger mosaic.

2.3 Drizzling

Each set of exposures is taken in a series of exposures with a small spatial separation between them. Part of this dithering pattern, the overlapping tiling of multiple same-filter observations at around the same time, is for cosmic ray removal, but it also allows image combination and subsampling. Combining images together through the drizzling technique returns a higher resolution, signal-to-noise ratio, and coverage than single images. This pattern then effectively reduces the contribution of error from a detector or exposure sequence. First, drizzling is considered in the observation proposal, where the pattern of observation is intentionally shifted for multiple exposures of the same region. If there is a lower quality region on an object of interest, it will be limited (ideally) to a smaller number of exposures. The Astrodrizzle software (Gonzaga et al., 2012) is used to combine these dithered exposures into a single image.

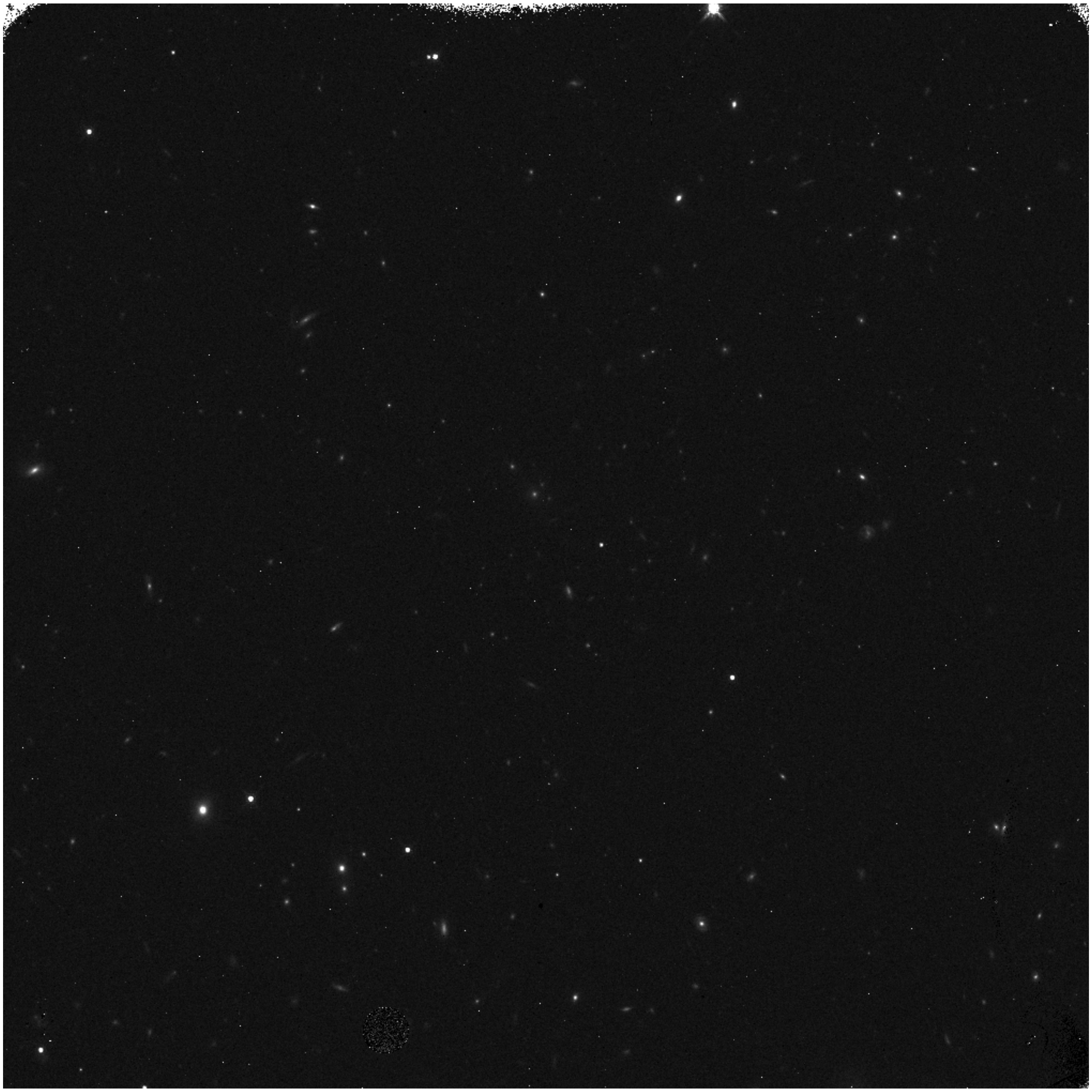

Figure 2.4: A sample F140W calibrated image, before drizzling step.

2.4 Subsampling

The images are matched in sky position, but they are different in detector space by nature. It is very likely that, even with matching and overlaying pixels, an object will be spread differently across pixels between images. For example, consider a case where your first image has the object at the centre of a pixel, the resulting distribution of light will be highest in this pixel, with that light decreasing into adjacent pixels. In a second case, your second image has the object at the corner of a pixel, distributing its light more evenly across 4 pixels. To account for this difference, Astrodrizzle creates a new pixel space, and populates this space by breaking down the dithered images into a finer resolution.

Subsampling is thus the process of turning each pixel into a grid of sub-pixels, which are then used to divide the light from the pixel into the new pixel space. In our examples before, an object in image 1 is entirely located within 1 pixel, but is captured in image 2 on the border between 4 pixels. Both of these images are sub-sampled, creating a sub grid of finer resolution than the initial. Now, each object has its centre resolved at higher resolution, but with no way to determine which parts of that finer grid carry the light. By matching the two objects' central locations, one can place the two sub-sampled grids on top of each other, and add them together. In the region of overlap there will be a contribution from all of the pixel from 1, and some fraction of the pixels from image 2. After drizzling multiple images, there will be a higher resolution image than before, with these sub-samples able to contribute different pieces of information about the object. In this example, the image where the object lies within primarily one pixel, the peak intensity and tight falloff is well characterized, whereas in the second image, the extent of that light is better captured. The final pixel scale I utilized was 0.06" per pixel, about half the resolution of the original WFC3 IR CCD pixel scale. This method does have a limit based on the increased signal-to-noise ratio with the addition of subpixels and the limit of the point spread function itself. In the first case you have the same amount of light spread over a larger number of pixels with correlated noise. In the second case an object projected on the CCD has passed through a filter which distorts and blurs the incoming light to some degree. Subsampling is useful if you have good signal-to-noise, as in the case of a multiple orientations with multiple exposures in a dither pattern, with an instrument with a point spread function smaller than it's pixel scale. These conditions are met with the HST observations presented in this work.

2.5 Image Mosaics

Finally, once these higher resolution stacked images are acquired, Astrodrizzle combines them into a single drizzled image. These drizzled images can be further stacked onto other drizzled images for overlap regions if they were taken for individual pointings. Astrodrizzle can also be run on the entire image set to acquire a full mosaic map with all drizzling done on overlapping regions. The processing of raw HST images was conducted using the grizli wrapper to run the CalWFC3 pipeline. This pipeline takes the raw and processes it sequentially with a given set of reference files corresponding to the location and time of the observation. This account for variations in the image quality over the Hubble Space Telescope's long life. A final calibrated image is shown in Fig. 2.4. As seen there, the features from varying quadrants, individual pixels, noise features, and cosmic rays have all been reduced. This leaves behind the signal of interest, the light coming from distant stars and galaxies. A sample drizzled image is shown in Fig. 2.5

2.6 Mosaics and Photometry

Contiguous mosaics for XLSSC 122 were created using the Astrodrizzle and Tweakreg packages from DrizzlePac (Gonzaga et al., 2012). These drizzled images combine overlapping images on a sub-pixel scale, increasing the signal-to-noise ratio and resolution. This initial drizzling did not require a thorough alignment, as images were taken as part of the same observation sequence using the same guide stars. These images were subsequently aligned to the source catalog of the drizzled Core region of XLSSC 122 from Willis et al. (2020) created using SExtractor (Bertin and Arnouts, 1996). As each image was added to the mosaic, its shifted catalog was used to align the next image. Final mosaics and inverse variance weight maps (IVM) for the F140W filter were created for 3 contiguous overlapping exposure regions as seen in the F140W filter exposure map footprint area Fig. 2.2, with relative astrometry within each contiguous region. A similar mosaic in F105W was created for the central region. The final mosaics and IVMs for the F814W band were created for overlap with the F140W contiguous regions, despite their span over the entire field. A false colour RGB image of the central region of XLSSC 122 is shown in Fig. 1.6

Initial catalogs using single image mode from SExtractor were extracted for each contiguous mosaic for each filter. Overlapping mosaics in different filters were matched with a tolerance of 0.3 arcseconds, or 5 pixels on the F140W mosaics to find the mean and standard deviation of the shift between objects in the mosaics. Mosaics were then shifted by the mean difference in sky positions between filters to match to the F140W mosaic after

Figure 2.5: A sample F140W drizzled image, before mosaicing step.

an iterative mean cut. This changed the reference point, the distance scale, and rotation of the image. Finally, aligned mosaics in F105W and F814W were resampled using SWARP (Bertin, 2010) to match the pixel scale and location of the F140W mosaics. This ensured that the information from the three overlapping filters have matching pixel locations.

Photometric information was extracted from each region by applying SExtractor to the mosaics and corresponding IVM image. Fluxes were computed from two apertures, a 13 pixel (0.78 arcseconds) fixed aperture and a variable elliptical aperture with a Kron factor of 0.8 as used in Willis et al. (2020). Extractions for F105W and F814W were made using SExtractor double image mode, using the F140W image as reference for astrometric position. In this way the aperture size and shape was identical between mosaics.

2.7 Grizli Spectral Extraction

The grizli (Brammer, 2019) software package is a python wrapper for Astrodrizzle (Gonzaga et al., 2012), Calwf3, SExtractor (through SEWPY), mastquery, astroquery, and axe among many others. In this project, grizli is used to make the final pipeline of image download, organization, calibration, drizzling, photometric extraction, spectroscopic extraction, and science image creation. The grizli software package works by calling a host of commands on an input footprint designating the files selected for analysis. This footprint is used to download the files and their corresponding calibration files. Then, the grizli auto script aligns the images by performing source matching through SEWPY. Once the images are aligned, grizli runs a pre-processing script which calls CALWF3 to perform photometric steps including but not limited to, bias removal, gain removal, data quality initialization, zero read subtraction, dark field subtraction, flat field division, non linearity correction, and cosmic ray removal.

In this project, spectroscopy was performed using the G141 slitless grism. A grism is a diffraction grated prism. Incident light to the grating is split scattered at varying angles dependent upon its wavelength by the diffraction grating. This spectrum is then redirected into a parallel path by the adjoining prism, where it is captured by a CCD. Light orthogonal to the dispersion axis is transmitted undispersed, and thus the spectral energy distribution (SED) is displayed as an extended region on a physical image. During each spectroscopic observing sequence, a photometric filter of a similar wavelength captures the light from that region at a time close to the observation. This image is used to identify the locations of objects for use in assigning spectra. In this project, the F140W filter serves as reference for the G141 filter due to it's similar wavelength range.

grizli begins spectrum extraction by matching F140W filter images to their corresponding G141 grism images. Once the objects are identified between images grizli identifies the region extended from the point source to find the first order spectrum, cutting it out as a subsample from the spatial image. The first order spectra is then background subtracted from the upper and lower regions of the image. Then, the middle portion is accumulated into a 1 dimensional spectral energy distribution (SED) following the method described in Horne (1986).

2.7.1 Contamination Modelling

The contamination model for a pointing is the interference from the dispersed spectra of a nearby object and is computed using the input segmentation map, catalogue, and science image. For each object, the spread of light is isolated and fitted using a 2nd order polynomial across the entire image. Then, as a followup, objects brighter than 24th magnitude are then narrowed in on and fit individually using a 4th order polynomial. This contamination model is the same size as the science image, but contains noiseless modelled spectra in place of real dispersed objects. When extracting an object in the science image, the contamination model is subtracted from the science image, excluding the object under extraction. Note that the contamination model does not remove all contamination, noise, irregular object shapes, and multiple stacked dispersions usually result in a region with higher variation than the background after model subtraction.

2.7.2 Beam Extraction

With the contamination model computed, it is now time to acquire the beams from the grism images. In this context, a beam is a rectangular cut out from the science image corresponding to the extracted source. The number of grism images indicates the number of resulting beams. In cycle 25 this was a maximum of 48 whereas in cycle 30 this is a maximum of 8.

To extract the beams, the object from the photometric image is matched to the position in the grism images. Then, a 20-30 pixel wide beam is extended outwards along the first order of the dispersed spectrum on the grism image. Smaller beam sizes are used for smaller objects, and larger for the BCG. Altering the beam size allows one to narrow regions where the contamination is affecting the main extraction itself or the background calculations (Boehm et al., 2024). The resulting beams are appear as cut out two dimensional spectra.

To obtain a 1 dimensional spectrum from the two dimensional spectrum, the beams are combined using the method detailed in Horne (1986), which effectively stacks all beams on top of each other and takes the weighted average, collapsing along the off-dispersion axis. This creates a single set of fluxes along the dispersion direction wavelengths.

2.7.3 Spectral Extraction and Classification

I extract spectroscopic information from the grism images using Grizli. The G141 spectroscopic images were calibrated using a similar process to the photometric images using Grizli and the calwf3 software as described in Sec. 2.2. Once calibrated, the G141 images images were then aligned to F140W images taken over the same fields. To do this, the intermediate F140W mosaics for each pointing were matched with each G141 image primarily overlapping that field. Then, a polynomial based contamination model was fit to each G141 image. By treating the spectroscopic extraction on a field-by-field basis, I sought to reduce the uncertainty added to the object position introduced by creating the mosaics between HST cycles. My interest here is the matching of the position of the object in the F140W field to the G141 fields, and the signal-to-noise ratio of the photometric images in the overlap regions was not my primary concern. I acknowledge that this does prevent the combination of spectral beams from overlapping fields due to the shift in their relative positions. Beams of width 20 pixels were extracted along the dispersion angle of each object and were averaged into a single 1 dimensional spectral trace.

I compute spectroscopic redshifts for objects, focusing on $z = 1.98$, using the G141 filter. The range of the G141 filter captures multiple rest frame optical features of $z = 2$ objects, including the the 4000 Å break and the [OIII]5007 Å emission line. Three template sets were fit to each object's beams, a continuum based set containing galaxy templates and absorption features in young and old stellar populations, the same continuum based set with 3 additional line complex templates (OII+Ne, OIII+Hb+Hg+Hd, and Ha+NII+SII+SIII+He+PaB), and the continuum based set with several additional individual line features including individual versions of each of the complex lines. The line features used include the Balmer emission and absorption lines, as well as several metal lines including oxygen, silicon, and neon along with several others. Template fitting was performed using a redshift grid between $z = 0 - 4.0$, with an initial course grid of $\delta z = 0.004$ and a finer grid of $\delta z = 0.0005$ around local minima. A sample fit to the no line template is shown in Fig. 2.6 and Fig. 2.7 for the BCG. Based on the result of these 3 template fits hereafter referred to as guess 1, guess 2, and guess 3, objects were visually inspected for best template fit and initial redshift guess. Objects were then placed into categories based on a number of selection cuts. These categories divided the objects based on reliability of the guess. Objects of category A and B are

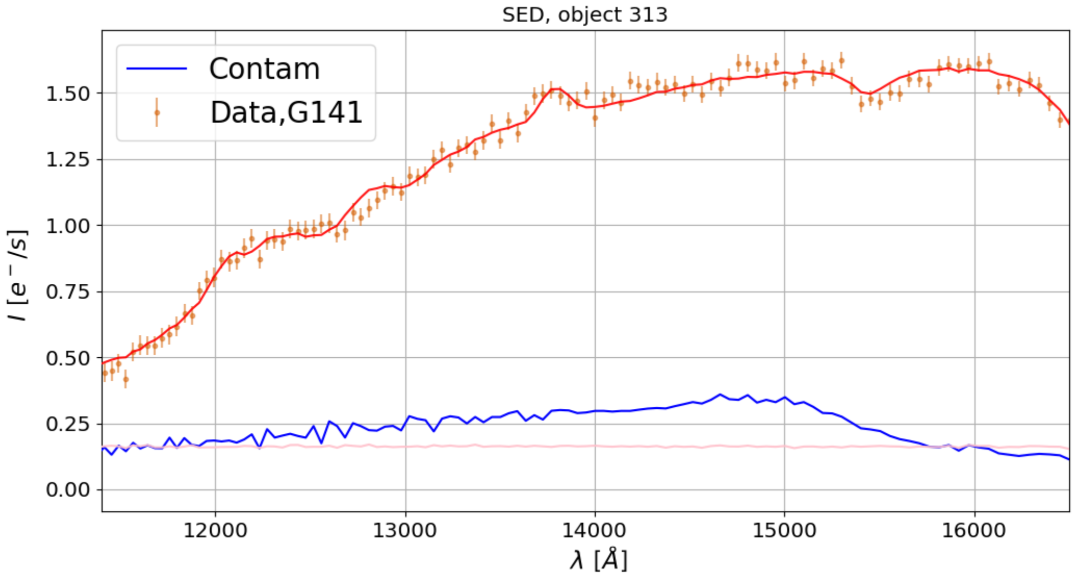

Figure 2.6: The optimally extracted one-dimensional SED for the brightest cluster galaxy (ID = 2659 in catalogue) of XLSSC 122 (orange) and a best χ^2 fit to the no-line template set. Contamination from nearby objects is shown in blue and the background is shown in pink.

bright, uncontaminated, high signal-to-noise ratio objects with a redshift guess within 0.1 of $z = 1.98$, only differing in whether the continuum guess and line complex guess agreed. Category C lacks a redshift guess within 0.1 of $z = 1.98$, but contains a peak in the χ^2 distribution in that same range in its top 3 local minima. Categories D and E were carefully inspected, containing either high contamination from nearby sources, or low signal-to-noise ratios. Category F, G, H, and I objects were not inspected as they contained none of their top 3 local minima in the χ^2 distribution near $z = 1.98$, were dimmer than 25th magnitude in F140W, lie in the stellar locus in FWHM/magnitude space, or have a signal-to-noise ratio less than 1 respectively.

I utilize Markov Chain Monte Carlo (MCMC) sampling in several places in this thesis, and I elaborate on this method here. The basic principle is to explore the parameter space and calculate a goodness-of-fit between the resulting model and the observed data. In many cases, I use the emcee python package (Foreman-Mackey et al., 2013) which I have compared with a custom built Metropolis Hastings method (Metropolis et al., 1953; Hastings, 1970). I do this as I am more familiar with the Metropolis Hastings method and I can have complete control over the acceptance criteria and exploration method. The same initial conditions apply to both applications of parameter estimation using MCMC from a given model which takes a set of input parameters and outputs data in a form comparable to observation. First, a set of bounds for the input parameters are set, outside of which the goodness-of-fit is set to $-\infty$. Then, a number of chain start locations, or walkers, are initialized within that space. For my work, I use a multivariate Gaussian with a mean away from the expected fit, and a scale equal to the 1 hundredth of the parameter range. Next, a new location is chosen from the position of the first. In my Metropolis Hastings model I draw a new point with a multivariate Gaussian of the same size as the initialization, with the central point located on the old point. Then, if the goodness-of-fit of the new point is greater than that of the old, the new point is accepted. If the goodness-of-fit is worse, it has a random chance of being accepted, this acceptance probability is equal to the ratio of the new to old likelihood. This acceptance threshold is the Metropolis Hastings algorithm, though in the last 70 years, more compelling algorithms have been developed which explore the space with greater speed and efficiency. For example the affine invariant ensemble sampler is better suited to exploring parameter spaces with an anisotropic shape between dimensions (Foreman-Mackey et al., 2013). Other methods use the gradient of the log-posterior, or a clever step path selection (Foreman-Mackey et al., 2013) to explore data sets with multiple high likelihood regions. The Metropolis Hastings method provides a good baseline, and I use an affine invariant ensemble sampler for my final fits. The likelihood function I use is the χ^2 distribution given

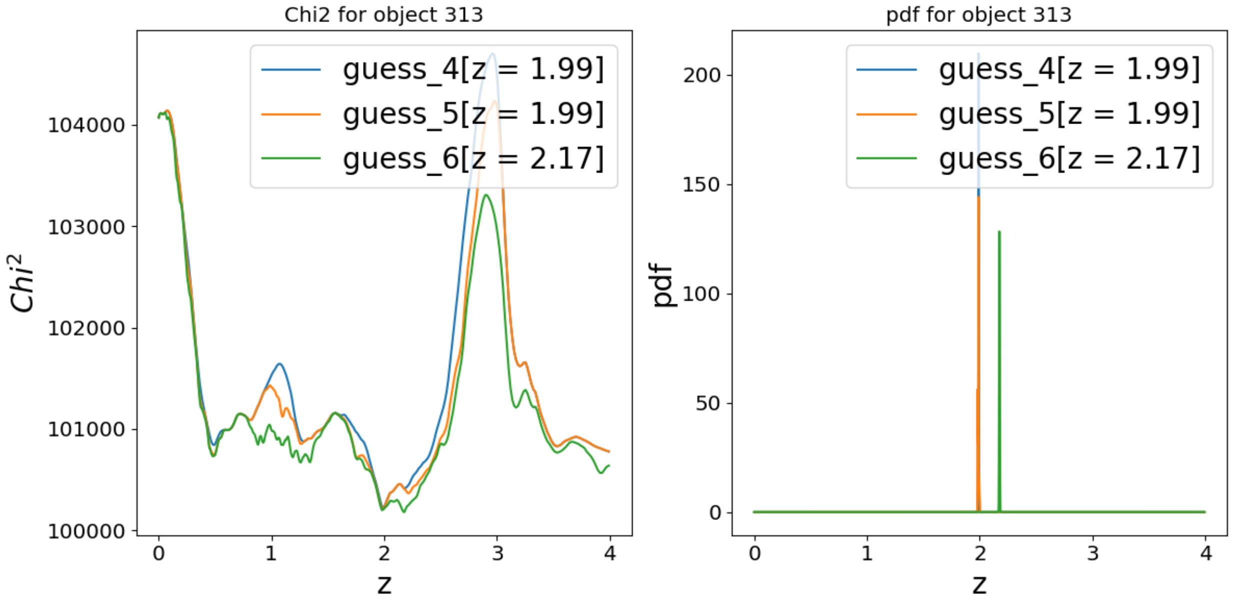

Figure 2.7: *Left:* The multiple template χ^2 over redshift fit test for the BCG (ID = 2659 in catalogue). Guesses 4, 5, and 6 are the no-line, complex, and line template fits in blue, orange, and green respectively. *Right:* The resulting probability distribution function given the χ^2 test on the left.

in Eq. 2.1

$$\chi^2 = -k \sum_{i=1}^{N} \frac{(D_i - M_i)^2}{\sigma_i^2} \tag{2.1}$$

where k is a normalizing factor, N is the total number of output dimensions i, D is an observed value along a dimension i, and M is the model value along a dimension i, and σ is the standard deviation of the observed value.

Returning to the spectral fitting, objects whose template fits appeared to roughly trace the data as determined by visual inspection were processed through a final template fit using the third template set containing individual lines with a Gaussian prior about the best initial guess. This was to identify galaxies which fit well at $z = 1.98$. If these galaxies could not be fit to $z = 1.98$ with a boost to the likelihood, I attempted a similar fit at different local minima in the initial χ^2 distribution. The objects which could be fit by a template combination at $z = 1.98$ were then passed through the same fitting process with a tophat prior between $z = 0.5$ and $z = 3.5$ to obtain a fit unbiased from the Gaussian prior. These final 2 template fits were performed using a MCMC method using the emcee python package (Foreman-Mackey et al., 2013) with 256-512 steps and 128-196 walkers. The final MCMC fit for the BCG yields the model shown in Fig. 2.8.

Objects were then visually inspected for goodness-of-fit, and rerun at varying initial positions, beam sizes, and beam selections to reduce contamination from nearby sources and avoid mediocre fits. A spectral signal-to-noise was computed between 1.3 and 1.55 μm as in Willis et al. (2020) as the average signal to noise per pixel over that range. Then, objects with a signal-to-noise ratio < 3 were inspected for the presence or absence of emission lines. Objects without emission features at this level of noise were discarded. Then, objects were divided into Gold, Silver, and Bronze cluster membership categories based on the integral of the redshift probability density function (p_{memb}) over the range $1.96 < z < 2.00$, as determined from Willis et al. (2020) as the $3\sigma_z$ observed frame velocity dispersion spread for a 5 keV galaxy in redshift space. With Gold defined as $p_{memb} > 0.5$, Silver defined as $0.1 < p_{memb} < 0.5$. The Bronze category for XLSSC 122 includes objects which would lie in the Gold or Silver categories except for their low signal-to-noise ratio. As noted by Willis et al. (2020) there is a foreground structure located at $z = 1.93$ in the vicinity of XLSSC 122. I conduct a similar fitting process for these objects to identify potential members, changing only the central redshift from $z = 1.98$ to $z = 1.93$, and define $p_{memb,2}$ as the redshift probability density function over the range 1.91 to 1.95. The details of the final categories for both structures are described in Table 2.2, I do not include a Bronze membership for the

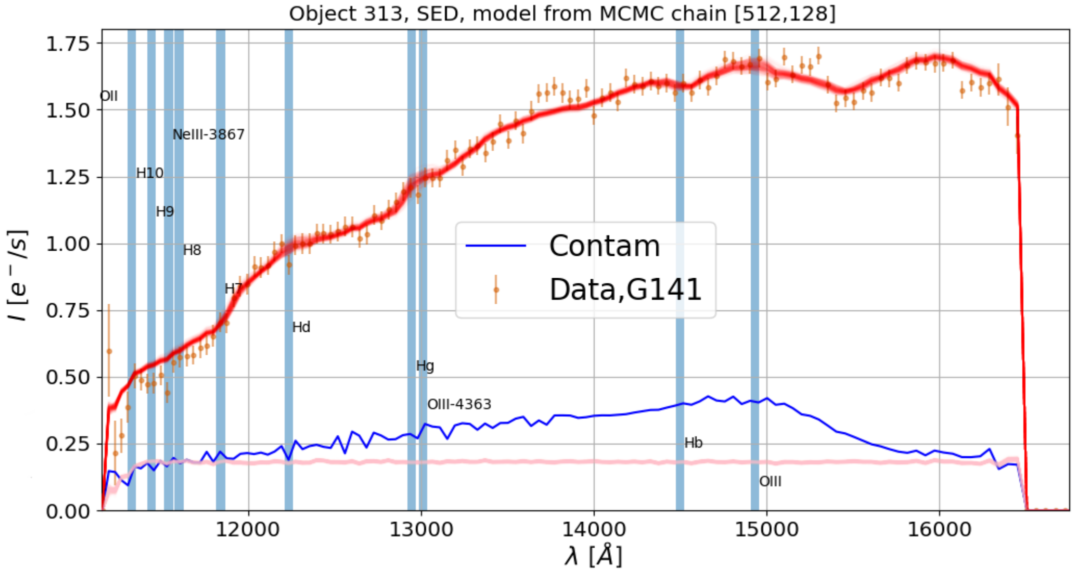

Figure 2.8: The final positions of the walkers expressed as model spectra overlayed on the 1-D SED (orange) of the BCG (ID = 2659 in catalogue). Contamination from the contamination model is shown in blue, and the background is modelled in pink. Overlayed are the lines considered in the fit, displaced to the redshift of the BCG in blue, with constant width for visual identification.

Table 2.2: Spectroscopic membership criteria for clusters in XLSSC 122 and CL J021741.7-034546.

Category	$p_{\mathrm{memb},1}$	$p_{\mathrm{memb},2}$	S/N
Gold	≥ 0.5	< 0.5	> 3
Silver	$\geq 0.1, < 0.5$	< 0.5	> 3
Bronze	≥ 0.1	< 0.5	$> 1, \leq 3$
Foreground Gold	< 0.5	> 0.5	> 3
Foreground Silver	< 0.1	> 0.1	> 3
Non-Member	< 0.1	< 0.1	> 3

1.93 structure. The distribution of redshifts in each category is given in Fig. 2.9. Note that there is overlap in the estimated redshift range of the foreground structure and XLSSC122. The reported zmcmc is the median of the locations of the final one third walkers. Objects labelled with a zmcmc outside of their p_{memb} range have walker locations outside of that range, drawing the median out of the range. The silver category shows the largest amount of objects outside of the range, with an extension out to z = 2.03. These objects have a peak outside of z = 1.96 to z = 2.0, but have at least 10% of their walker locations within that range.

2.7.4 Contaminated Beam Removal

In the central regions, objects are dispersed in multiple directions. In cases where one of these pointing angles leads to the contamination of 1 beam by a nearby object, the resulting redshift estimate will differ. To correct for this error, I extract the 1 dimensional spectra for each beam at all pointing angles and remove the beams with a contamination to signal ratio greater than 1. With the remaining lower contamination beams, I rerun the 1 dimensional spectra extraction and initial guesses, processing those guesses, running the MCMC template fit, and eventual category assignment as normal.

2.7.5 Difficulty in MCMC Runs

The intention of my pipeline was to preserve a similar spectroscopic process to the cycle 25 data when running on the cycle 30 data. However, I found that the cycle 30 data, given the larger area and lower number of grism exposures per object, was more difficult to fit. The spectra extracted from the cycle 30 grism images tended to have a lower signal-to-noise ratio and a more prevalent occurrence of contamination. The lower signal-to-noise ratio causes

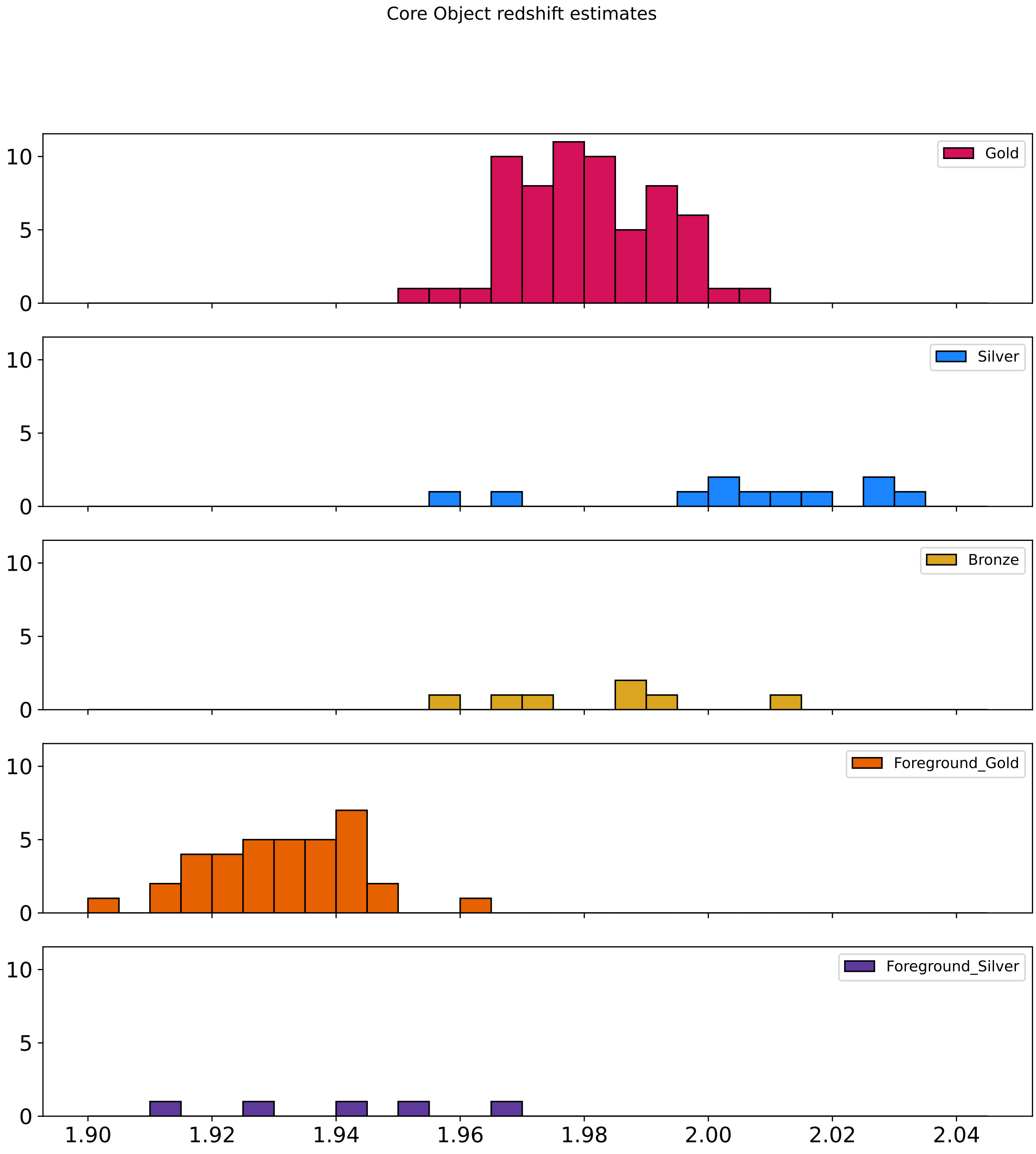

Figure 2.9: The redshift estimate histograms for each redshift classification.

a difficulty in fitting a spectra to low amplitude emission line peaks, and I relied more on the continuum template fitting. Additionally, cycle 25 observations have 4 unique pointing angles, allowing several opportunities to observe an object in different frames to account for contamination. The cycle 30 data, on the other hand, had a maximum of 2. In the central regions near the core the isolation of 1 of 2 pointing angles has allowed the confirmation of certain objects as belonging to the cluster. However, in the outer reaches, farther from the centre of the cluster, I found that the single grism exposure occasionally resulted in potential cluster members that were difficult to extract or fit a template to.

2.8 Comparisons with Prior Catalogues of XLSSC 122

I provide a comparison between the catalogue of the inner regions of XLSSC 122 from Willis et al. (2020) and the catalogue I have created in the previous steps. I find that among matched objects, differences in magnitude or FWHM between reductions is centred on zero with a scatter increasing to greater magnitudes. A comparison of the colour magnitude diagram is shown in Fig. 2.11, a comparison of the star galaxy separation plot is shown in Fig. 2.12. The individual magnitude and FWHM residuals is shown in Fig. 2.13 and Fig. 2.14. A map of the residual distance is shown in Fig. 2.10, with an internal distance offset consistent with a small uncertainty on the relative distance measurements. There is a shift in locations between catalogues showcased by the central density offset from 0, which can be explained by the use of different guide stars in my catalogue. My catalogue is in good agreement with that of Willis et al. (2020), with several improvements on previous measurements of FWHM, as seen in Fig. 2.12, where objects previously placed at an nonphysical 0 FWHM are shifted to the location of the stellar locus as 0.2. Using my pipeline, only 1 object is not identified as a cluster member of XLSSC 122 which was previously identified in Willis et al. (2020). Upon further analysis I deemed that this object was not a cluster member due to contamination from another galaxy. As the reduction pipeline has lead to a catalogue consistent with that of Willis et al. (2020) with noise, I use my new catalogue for consistency between measurements.

2.9 Spectroscopic Incompleteness

I estimate the spectroscopic incompleteness on the identification of cluster galaxies by creating mock G141 spectra and passing them through the spectral classification pipeline. A single template of an old stellar population included in the set of templates from Sec. 2.7.3 was used for the fits (Brammer et al., 2008). I estimate the background noise, object size,

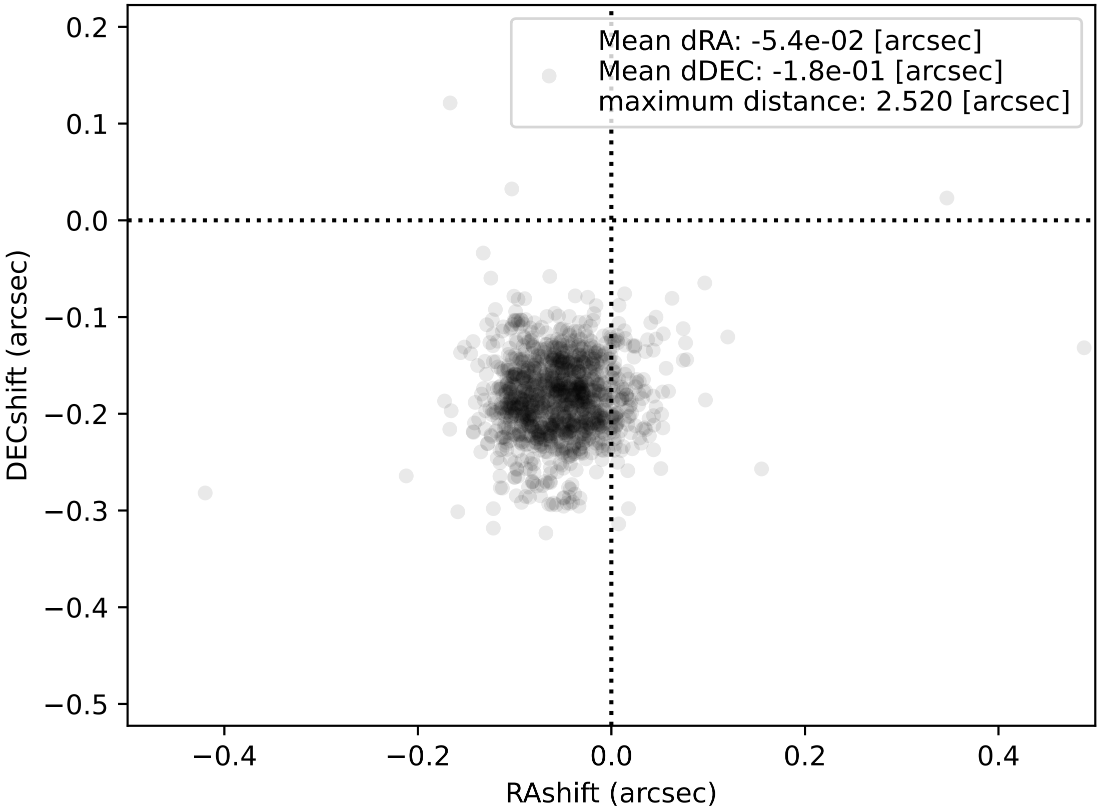

Figure 2.10: The difference in the position of points in my new catalogue and the old catalogue from Willis et al. (2020). Each black circle is the distance between an object in the first catalogue and its closest neighbour in the second catalogue

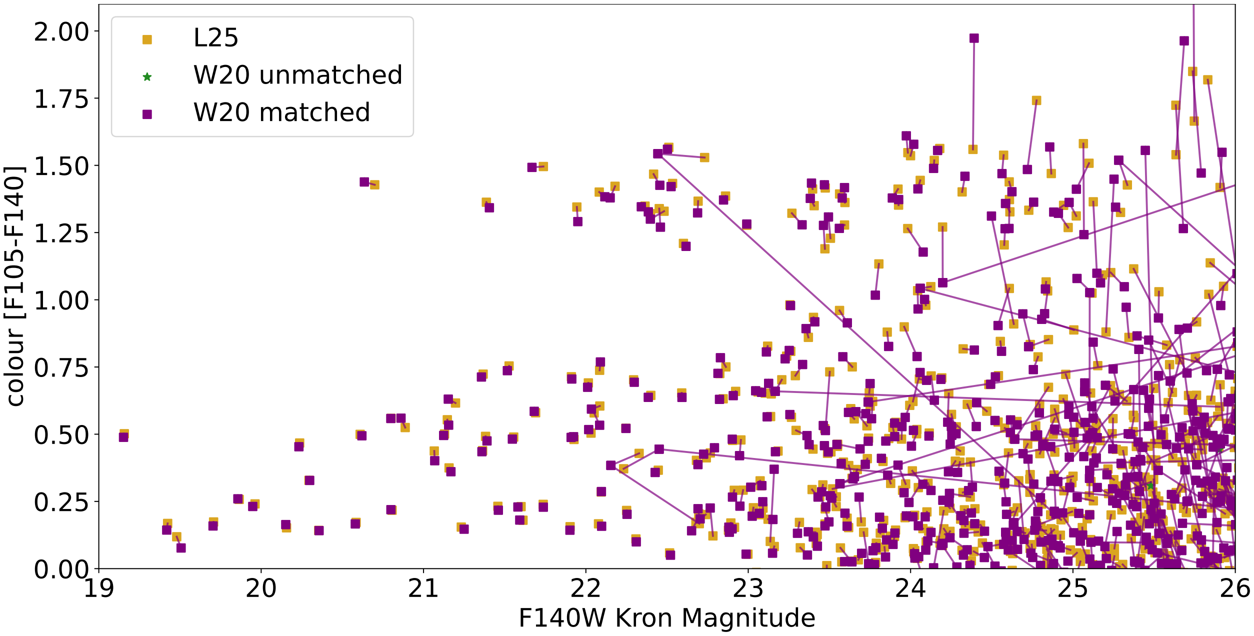

Figure 2.11: A comparison between the photometry from Willis et al. (2020) and my most recent catalogue.

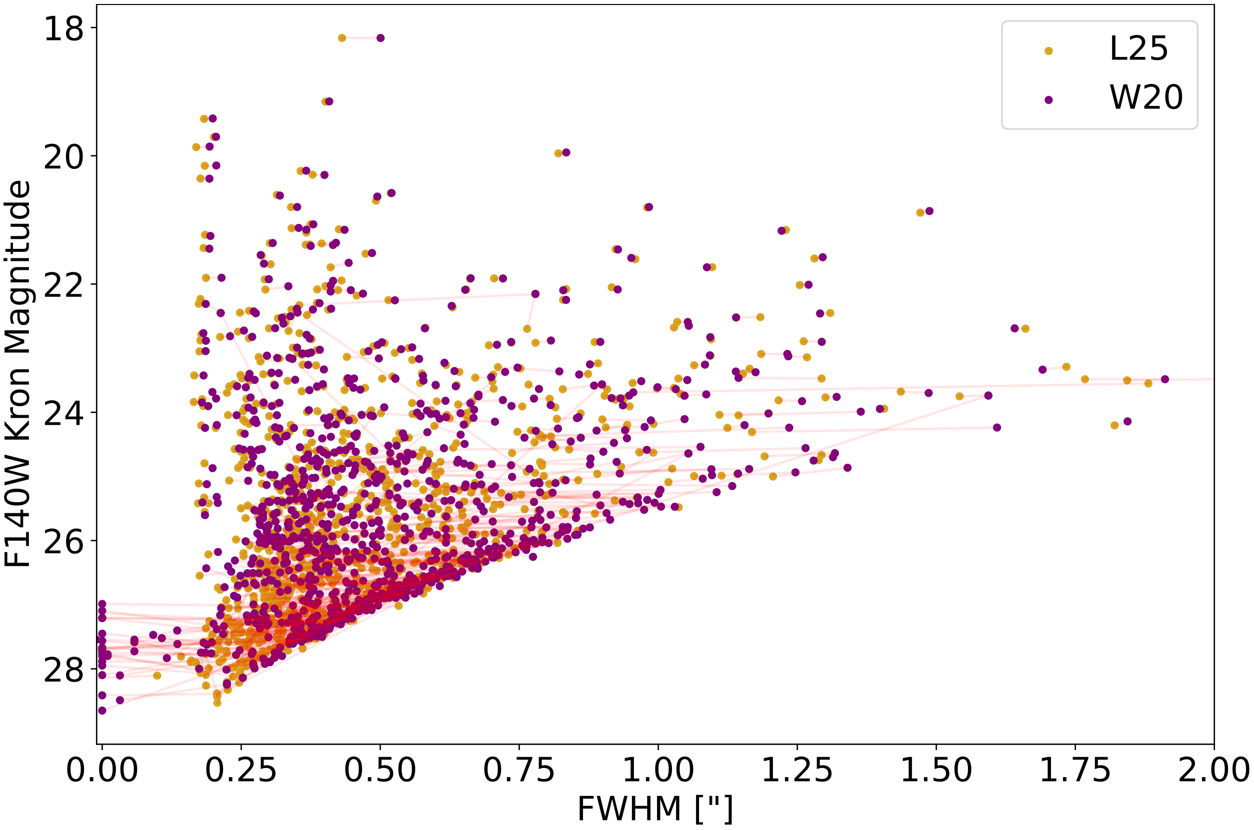

Figure 2.12: The star galaxy separation plot between matched objects in my catalogue to those of Willis et al. (2020).

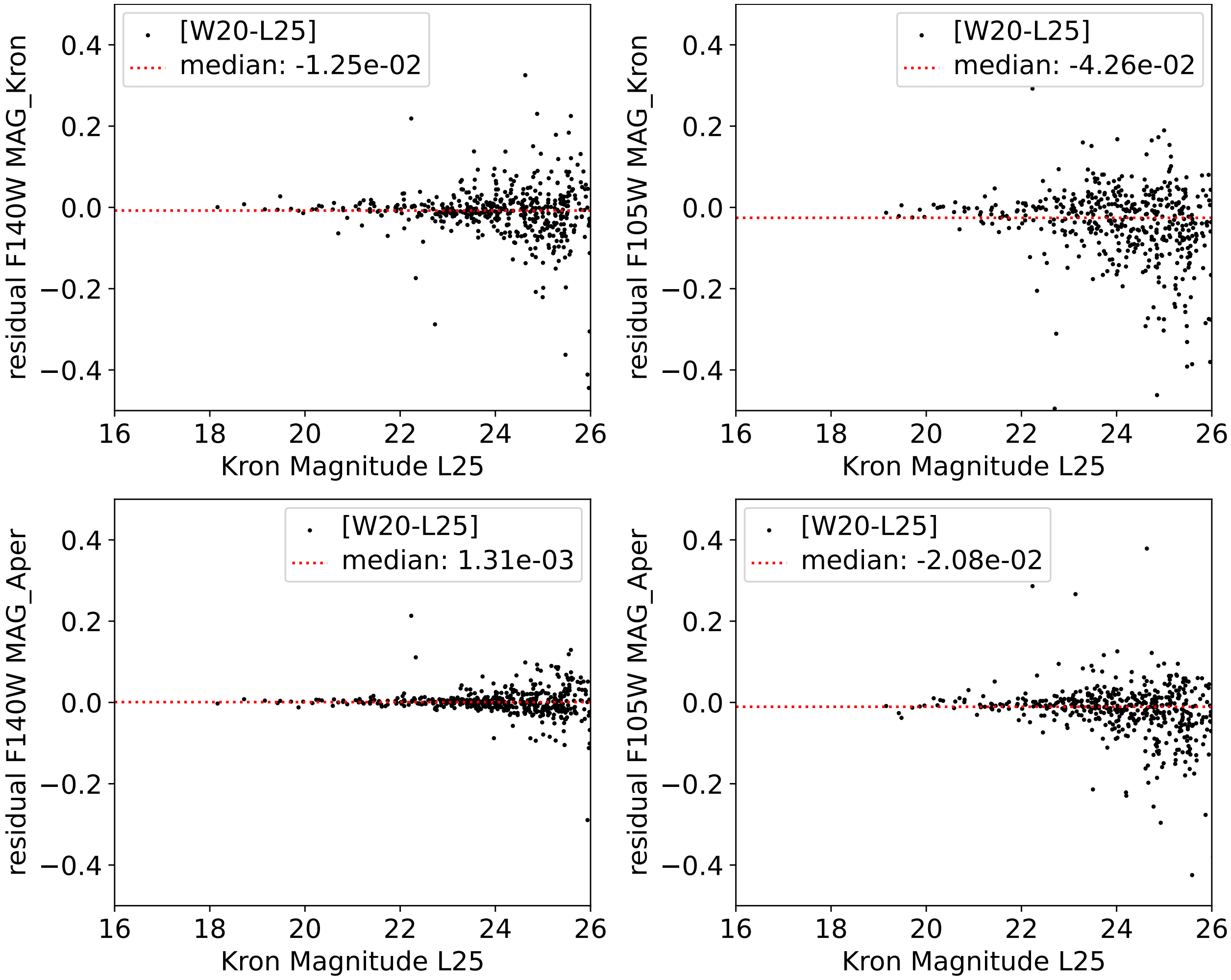

Figure 2.13: The photometric residuals between matched objects in my catalogue to those of Willis et al. (2020). The red line indicates the median residual.

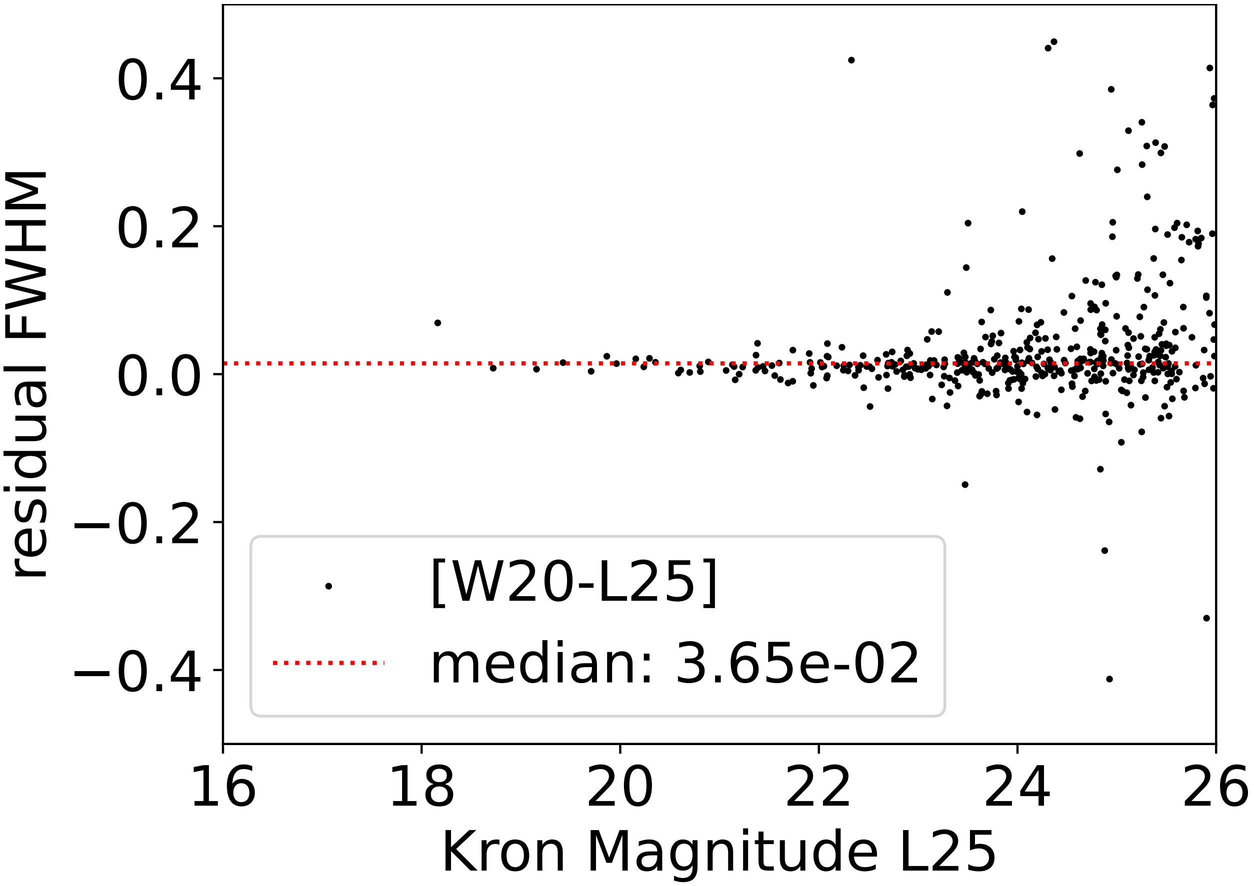

Figure 2.14: The FWHM residuals between matched objects in my catalogue to those of Willis et al. (2020). The red line indicates the median residual.

amplitude, and extent for the 2 cycles and 3 exposure regions by extracting regions above and below the primary beam for a given reference object. I take the median between all beams and their upper and lower regions, finding little variation between beams and upper and lower regions. The G141 data taken in cycle 25 was collected over 48 exposures of t $\approx$ 550 s each. The data taken in cycle 30 was collected over 4 or 8 exposures of t $\approx$ 1000 s each, leading to a different contribution of noise per beam. To estimate the amplitude of the signal for each beam, I extract the 1 dimensional spectra for 4 sample objects of F140W magnitudes 21 through 24 for both cycle 25 and cycle 30. I scale the amplitude of each simulated beam such that its integrated 1 dimensional flux is equal to a real object of that magnitude. To incorporate background error I add in a random Gaussian error according to the beam exposure time. To approximate the counting error of signal pixels I further add a random Gaussian centred on the pixel intensity with a standard deviation equal to the Poisson counting uncertainty. I then pass these simulated beams through my classification pipeline, stopping at the initial χ^2 grid search, using only the continuum templates. I show a comparison of my simulated optimally extracted spectra to an observed red galaxy at similar magnitude in Fig. 2.15. I classify any galaxy passing the local minimum test as being successfully identified. A plot of the spectroscopic completeness for the 3 exposure time regions across magnitude is shown in Fig. 2.16.

In running the spectroscopic incompleteness test, I noticed that there is an anomalously low completeness for objects of 22nd magnitude in the 4 beam low exposure time region as seen by the red points in Fig. 2.16. Because of this, the spectroscopic incompleteness for the low exposure time region is not monotonic, and I do not believe it to be physical. Going forward, when incorporating spectroscopic incompleteness, I interpolate over this data point, excluding it from consideration. Further, the low number of cluster members in these low exposure time regions means that this irregularity does not change the estimates of local overdensity, density profiles, or luminosity functions. The central region of the cluster, where most of the data for these relations originates from, contains few galaxies at this low exposure time range. A more thorough treatment of spectroscopic incompleteness would however, allow a further exploration of all galaxies in the cluster, as the current estimate was created solely with a simple old stellar population. I am currently assuming that the spectroscopic incompleteness is roughly equivalent between the red sequence and blue cloud. Considering the blue cloud members identified as cluster members extend to greater magnitudes and contain prominent emission features, this may be a conservative estimate. However, these galaxies are likely preferentially selected over blue galaxies lacking strong emission features.

The incorporation of spectroscopic incompleteness primarily increases the expected num-

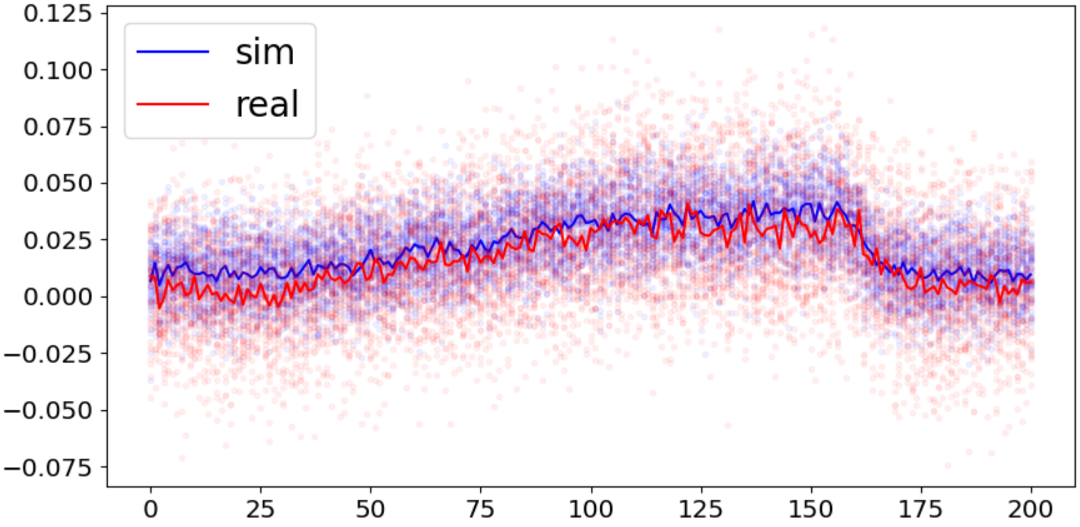

Figure 2.15: Simulated spectra (blue) compared to an observed spectra (red) for a magnitude 23 object in the F140W filter. Lines are the medians across beams and individual points are from individual beams. This is from the high exposure time region, containing 48 beams.

ber of low luminosity galaxies in the outer regions, which increases the expected density at larger distances from the cluster centre. This is incorporated in Sec. 3.1 and Sec. 3.4, but does not significantly alter the conclusions therein.

2.10 Post Starburst Identification

Several galaxies in the spectroscopic sample have visual Balmer absorption lines in their spectral fits, indicative of a post-starburst galaxy (Werle et al., 2022). Galaxies have been classified as post starburst based on their absorption feature strength in low to medium resolution spectra (Dressler et al., 1999). I find the line strength with the equivalent width calculated as Eq. 2.2 .

$$EW = \sum_{x} \left(1 - \frac{F_{x,s}}{F_{x,c}}\right) \tag{2.2}$$

Here, x indicates a spectral pixel, and F indicates the intensity at that pixel. The model corresponds to the best fit non-emission line model, which includes absorption features as an option. The continuum intensity is interpolated from the intensity on either side of the absorption feature.

I use a fixed width band centred on the redshifted line wavelength. I determined the band size after a visual inspection of several galaxies with prominent absorption features to cover the full trough, settling on 200 Å. Likewise, I select a fixed continuum band size to include a small number of points on either side. I used a simple linear interpolation between the mean values in the continuum bands on either side of the feature to construct the continuum. I place a conservative cut on the EW of $H_\beta > 0.1$ and $H_\delta > 0.3$ to acquire galaxies outside of the scatter of measured EWs around the origin. I apply a further cut on signal-to-noise $>$ 15 and F105-F140 colour $>$ 1.15, as the equivalent widths measured for these objects were dominated by noise or star formation emission features. An example extraction for a galaxy with PS features is shown in Fig. 2.17 and a plot of the EWs and those selected based on colour and signal-to-noise is shown in Fig. 2.18.

In Table 2.3, and Table 2.4 I show the galaxies classified as cluster members and their extracted photometric properties and spectroscopic features. The ids are unique across the combined cycle 25 and cycle 30 data, with duplicates in position assigned a single id, and photometry and spectroscopy from the lowest uncertainty spectral extraction. Shown also is the astrometric positions, magnitudes, and colours from the F140W, F105W, and F814W filters if available. The redshift shown is the spectroscopic redshift from Sec. 2.7.3, with CM indicating the membership classification as shown in Table 2.2. The PS column is those

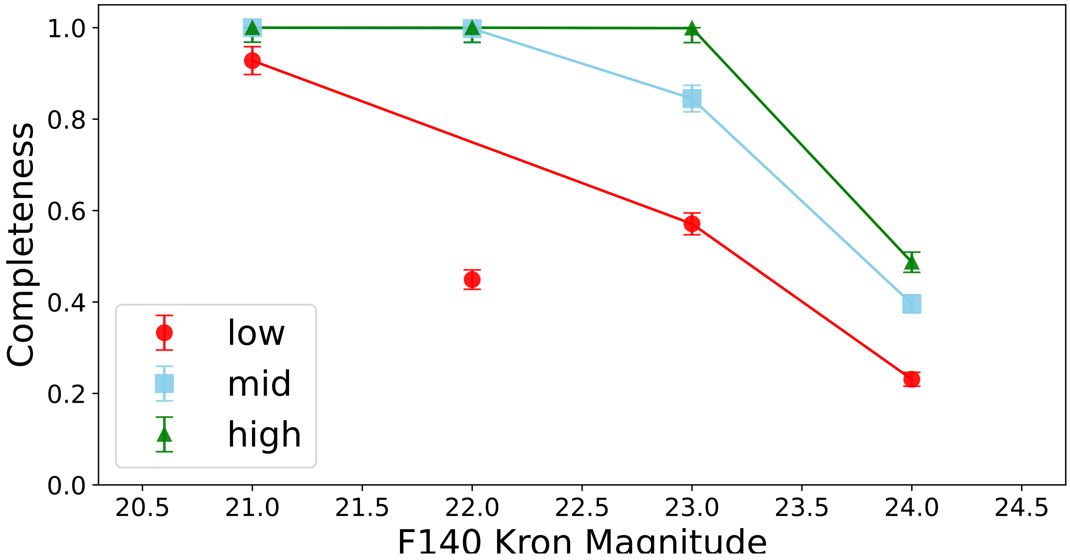

Figure 2.16: Simulated spectroscopic incompleteness across magnitudes and exposure time regions. Low exposure time regions those with exptime $< 4000\,\mathrm{s}$ from Table 2.1, mid exposure time regions are those with $\approx 8000\,\mathrm{s}$, and the only high exposure time regions are the cycle 25 G141 exposures with $\approx 26,500\,\mathrm{s}$.

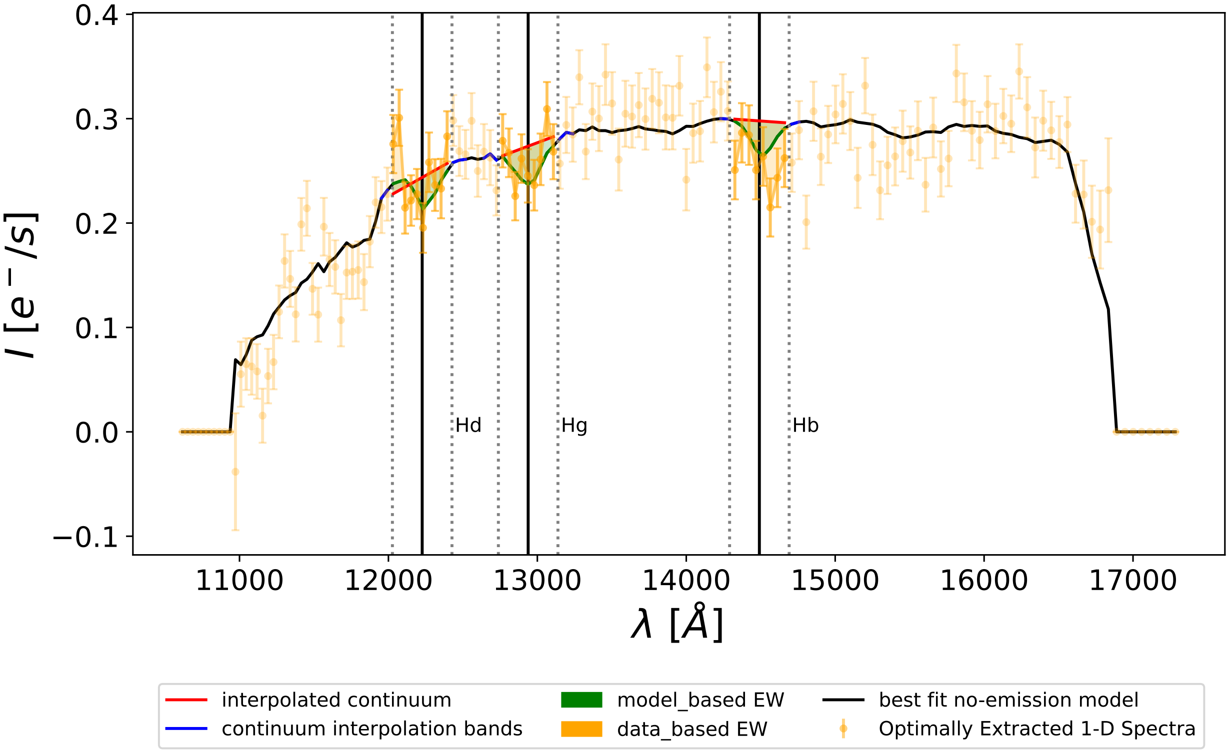

Figure 2.17: An outline of the EW extraction on a galaxy with PS features. The optimally extracted 1 dimensional spectrum (orange) and best fit non-emission model (black) are shown across the wavelength range of the G141 grism. 3 regions centred on $H_\beta, H_\gamma, H_\delta$ are shifted to the estimated redshift of the object from the spectral extraction stage. The green curve traces $F_{x,s}$ and the red line traces $F_{x,c}$ as described in Eq. 2.2. The green area is the area between the model and the interpolated continuum. The orange region is the area between the data itself and the interpolated continuum.

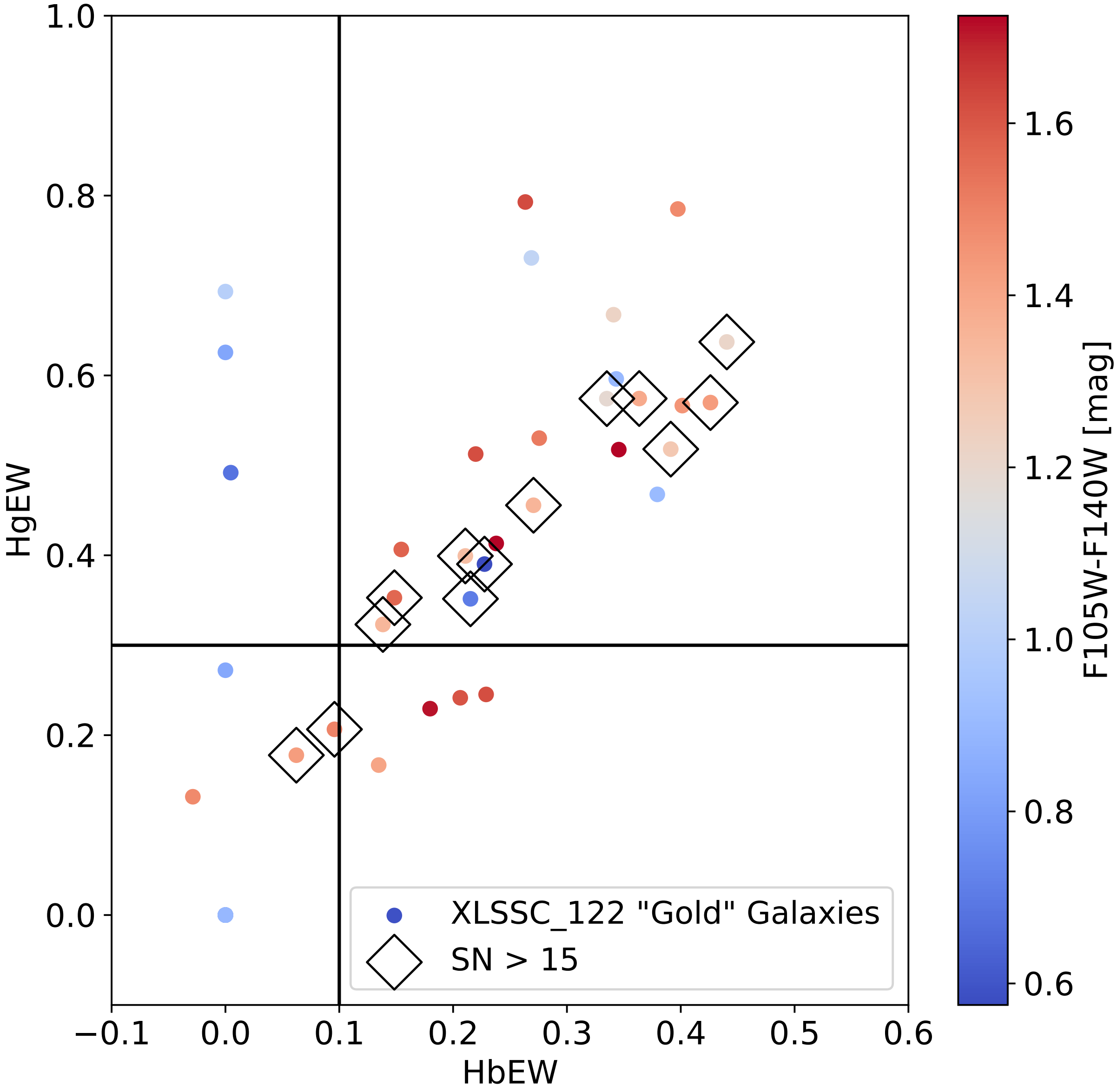

Figure 2.18: The Equivalent Widths of H_β and H_γ measured for Gold member galaxies of XLSSC 122. Objects are coloured by F105-F140W colour, with a red colouration if F105-F140W $>$ 1.15, which is the cut for PS classification. Galaxies with a signal-to-noise ratio $>$ 15 are outlined with black diamonds.

objects satisfying the post-starburst feature condition shown in Fig. 2.18.

Table 2.3: The reduced catalogue of photometric and spectroscopic information for the galaxy cluster XLSSC122. F140W kron magnitude, colours from 13 px (0.78 arcsecond) circular apertures, and colour errors are in AB magnitude.

id	RA [deg]	Dec [deg]	Redshift	PS	CM	M [F140W]	$M_\sigma[F140W]$	colour [F105-F140]	colour$_\sigma[F105-F140]$	colour [F814-F105]	colour$_\sigma[F814-F105]$
181	34.5157	-3.7852	1.967	n	G	23.24	0.03	nan	nan	nan	nan
186	34.5079	-3.7847	1.994	n	G	22.68	0.02	nan	nan	nan	nan
202	34.5014	-3.784	1.974	n	G	23.56	0.04	nan	nan	nan	nan
291	34.5124	-3.7771	2.006	y	G	22.83	0.02	nan	nan	nan	nan
603	34.5298	-3.7467	2.0	n	S	23.39	0.03	nan	nan	nan	nan
644	34.5215	-3.7342	1.976	n	G	22.85	0.02	nan	nan	nan	nan
776	34.5008	-3.7299	1.958	n	G	23.17	0.03	nan	nan	nan	nan
808	34.5248	-3.7347	1.999	n	G	22.18	0.01	nan	nan	nan	nan
811	34.5001	-3.7395	1.968	n	G	22.55	0.02	nan	nan	nan	nan
823	34.5032	-3.738	1.968	n	G	24.23	0.05	nan	nan	nan	nan
848	34.3645	-3.7702	2.003	n	S	22.37	0.02	nan	nan	nan	nan
934	34.3505	-3.7592	1.974	n	G	22.51	0.02	nan	nan	nan	nan
1012	34.3545	-3.7507	1.976	n	G	22.02	0.02	nan	nan	nan	nan
1066	34.3773	-3.7459	1.992	n	G	22.28	0.03	nan	nan	nan	nan
1141	34.3584	-3.7384	1.993	n	G	20.46	0.01	nan	nan	nan	nan
1230	34.3535	-3.7313	1.987	y	G	22.57	0.02	nan	nan	nan	nan
1396	34.3467	-3.7149	1.974	n	G	23.17	0.03	nan	nan	nan	nan
1499	34.3703	-3.7028	1.981	n	G	21.07	0.01	nan	nan	nan	nan
1654	34.4209	-3.7932	1.986	n	G	23.3	0.02	0.08	0.03	-0.06	0.02
1735	34.4118	-3.7894	1.989	n	B	23.94	0.03	0.08	0.03	0.14	0.03
1894	34.3983	-3.7838	1.995	n	G	22.89	0.01	0.61	0.03	0.07	0.03
1910	34.4202	-3.7827	1.99	n	G	22.78	0.01	1.55	0.02	1.67	0.11
1988	34.4477	-3.7809	1.975	n	G	23.69	0.03	0.06	0.03	0.02	0.01
2082	34.4791	-3.7775	1.988	y	B	23.48	0.03	0.32	0.04	0.35	0.04
2146	34.4465	-3.7755	1.98	n	G	24.3	0.03	0.4	0.03	-0.07	0.02
2176	34.4132	-3.7741	1.98	n	G	23.07	0.01	1.41	0.02	2.24	0.16
2235	34.4448	-3.7728	1.986	n	G	22.9	0.01	0.48	0.01	0.32	0.02
2322	34.4405	-3.7703	1.982	n	G	24.04	0.02	0.5	0.02	0.26	0.03
2333	34.4224	-3.77	1.98	y	G	22.6	0.01	1.21	0.01	1.19	0.03
2334	34.3974	-3.7702	1.997	n	G	22.95	0.01	1.42	0.02	1.34	0.08
2336	34.43	-3.7703	1.98	n	G	23.9	0.01	0.12	0.01	0.42	0.02
2359	34.4211	-3.7692	1.982	n	G	24.28	0.02	0.53	0.02	0.33	0.04
2397	34.4503	-3.7687	1.961	n	S	24.28	0.02	0.2	0.02	0.4	0.03
2411	34.435	-3.7679	1.988	n	G	22.51	0.01	1.57	0.01	1.84	0.09
2414	34.4472	-3.768	1.986	n	G	22.53	0.01	1.43	0.01	1.33	0.07
2442	34.4419	-3.7666	1.987	n	G	23.59	0.01	1.28	0.03	1.08	0.11
2453	34.4276	-3.7674	1.973	n	B	24.37	0.02	0.4	0.02	0.41	0.03
2456	34.4527	-3.7671	1.99	n	G	23.59	0.02	1.23	0.03	1.0	0.11
2479	34.4434	-3.7666	1.972	n	B	24.24	0.02	0.65	0.03	0.45	0.07
2508	34.4688	-3.7658	1.983	n	G	22.98	0.03	0.25	0.04	0.19	0.04
2514	34.4441	-3.7656	1.974	n	G	23.1	0.01	0.65	0.01	1.3	0.06
2515	34.4233	-3.7658	1.997	n	B	23.98	0.02	1.26	0.03	1.21	0.13
2535	34.4723	-3.7658	1.961	n	G	23.91	0.04	0.38	0.04	0.29	0.05
2573	34.419	-3.7638	1.98	n	G	23.55	0.02	0.46	0.02	0.42	0.03
2590	34.4223	-3.7635	1.982	n	G	21.94	0.0	1.35	0.01	1.17	0.03
2605	34.4187	-3.7637	1.982	n	G	24.12	0.02	0.5	0.02	0.28	0.03
2633	34.433	-3.7631	1.979	n	G	23.56	0.01	1.39	0.02	1.9	0.15
2648	34.4131	-3.763	1.979	n	G	23.33	0.01	0.39	0.01	0.22	0.01

id	RA [deg]	Dec [deg]	Redshift	PS	CM	M [F140W]	$M_\sigma[F140W]$	colour [F105-F140]	colour$_\sigma[F105-F140]$	colour [F814-F105]	colour$_\sigma[F814-F105]$
2659	34.4342	-3.7587	1.986	n	G	20.7	0.0	1.43	0.01	1.6	0.03
2678	34.4353	-3.7624	1.968	n	G	23.95	0.02	0.29	0.02	0.27	0.02
2683	34.4171	-3.7621	1.982	n	G	23.96	0.02	0.9	0.02	0.89	0.07
2687	34.4325	-3.7618	2.002	n	S	23.47	0.01	1.42	0.03	1.97	0.18
2699	34.4733	-3.7619	2.001	n	S	24.3	0.05	0.36	0.05	0.62	0.05
2721	34.4394	-3.7603	1.978	n	G	23.4	0.01	0.44	0.02	0.47	0.03
2722	34.4385	-3.7607	1.974	y	G	22.99	0.01	1.28	0.01	1.57	0.06
2775	34.4341	-3.7576	1.986	n	G	21.74	0.01	1.5	0.01	1.73	0.06
2781	34.4338	-3.7588	1.985	n	G	22.48	0.01	1.33	0.02	1.43	0.07
2826	34.4398	-3.7582	1.98	n	G	23.98	0.01	1.55	0.03	73.43	99.0
2827	34.4306	-3.7576	1.98	n	G	23.47	0.02	1.19	0.04	1.44	0.19
2830	34.425	-3.758	1.997	y	G	23.4	0.01	1.41	0.02	1.57	0.11
2887	34.4477	-3.756	1.991	n	G	23.8	0.02	1.13	0.03	1.45	0.22
2912	34.4347	-3.7548	1.979	n	G	23.41	0.01	1.35	0.02	1.65	0.12
2958	34.4356	-3.7531	1.968	n	G	22.74	0.01	0.41	0.01	0.68	0.01
3037	34.4325	-3.7499	1.989	y	G	22.4	0.01	1.32	0.01	1.7	0.06
3049	34.4369	-3.7501	1.988	y	G	22.86	0.01	1.39	0.01	2.02	0.12
3050	34.41	-3.75	1.993	n	G	22.99	0.01	0.49	0.01	0.46	0.01
3053	34.4389	-3.75	2.0	n	S	24.31	0.02	0.44	0.02	0.4	0.04
3058	34.4359	-3.7495	1.988	y	G	22.36	0.01	1.35	0.01	1.59	0.07
3114	34.4336	-3.7477	1.969	n	G	23.87	0.01	0.48	0.02	0.25	0.02
3161	34.4017	-3.7458	1.986	n	G	23.61	0.02	0.47	0.02	0.24	0.03
3188	34.4434	-3.7449	1.982	n	G	23.51	0.01	1.23	0.02	1.38	0.08
3203	34.3944	-3.7442	1.994	n	G	24.03	0.03	0.4	0.03	0.19	0.03
3222	34.4275	-3.743	1.966	n	G	22.96	0.01	0.48	0.01	0.5	0.02
3273	34.4089	-3.7412	1.957	n	B	24.31	0.03	0.1	0.03	0.11	0.03
3283	34.4459	-3.741	1.975	n	G	23.7	0.02	0.17	0.02	0.18	0.01
3383	34.4002	-3.7355	1.976	n	G	22.01	0.01	1.19	0.01	1.11	0.02
3407	34.4016	-3.7347	1.967	n	B	24.34	0.03	0.07	0.03	0.3	0.03
3457	34.417	-3.7307	1.994	n	B	23.81	0.02	0.25	0.02	0.4	0.02

Table 2.4: The reduced catalogue of photometric and spectroscopic information for the galaxy cluster CL J021741.7-034546. F140 kron magnitude, colours from 13 px (0.78 arcsecond) circular apertures, and colour errors are in AB magnitude.

id	RA [deg]	Dec [deg]	Redshift	PS	CM	M [F140W]	$M_\sigma[F140W]$	colour [F105-F140]	colour$_\sigma[F105-F140]$	colour [F814-F105]	colour$_\sigma[F814-F105]$
345	34.502	-3.7708	1.932	nan	FG	23.09	0.03	nan	nan	nan	nan
481	34.5085	-3.7567	1.925	nan	FG	22.37	0.02	nan	nan	nan	nan
536	34.511	-3.7521	1.935	nan	FG	23.7	0.03	nan	nan	nan	nan
687	34.5179	-3.7386	1.911	nan	FG	22.92	0.02	nan	nan	nan	nan
786	34.5031	-3.73	1.93	nan	FG	22.46	0.02	nan	nan	nan	nan
789	34.5093	-3.731	1.918	nan	FG	21.81	0.01	nan	nan	nan	nan
892	34.3593	-3.7624	1.945	nan	FG	20.98	0.01	nan	nan	nan	nan
946	34.3697	-3.7578	1.918	nan	FG	21.11	0.01	nan	nan	nan	nan
985	34.343	-3.7537	1.92	nan	FG	22.0	0.04	nan	nan	nan	nan
1038	34.3514	-3.7487	1.925	nan	FG	22.75	0.02	nan	nan	nan	nan
1173	34.37	-3.7364	1.936	nan	FG	21.29	0.01	nan	nan	nan	nan
1432	34.3664	-3.7117	1.936	nan	FG	21.92	0.01	nan	nan	nan	nan
1457	34.3615	-3.7089	1.904	nan	FG	21.1	0.01	nan	nan	nan	nan
1891	34.3985	-3.7837	1.941	nan	FG	22.79	0.01	0.42	0.01	0.62	0.02
1947	34.4213	-3.7822	1.95	nan	FS	24.08	0.03	0.13	0.03	0.11	0.02
2015	34.4271	-3.7797	1.92	nan	FG	23.66	0.03	0.53	0.04	0.57	0.05
2097	34.4533	-3.7729	1.942	nan	FG	19.11	0.0	0.2	0.01	0.15	0.0
2148	34.4597	-3.7746	1.941	nan	FS	22.35	0.02	0.44	0.02	0.65	0.03
2178	34.3951	-3.7747	1.928	nan	FG	24.13	0.02	0.63	0.03	0.1	0.04
2194	34.3946	-3.7725	1.927	nan	FG	22.06	0.01	0.19	0.02	0.18	0.02
2253	34.4569	-3.7727	1.968	nan	FS	22.94	0.02	0.02	0.02	0.17	0.01
2256	34.4438	-3.7719	1.923	nan	FG	22.25	0.01	0.52	0.01	0.57	0.01
2275	34.4226	-3.7717	1.94	nan	FG	23.62	0.01	0.38	0.01	0.14	0.01
2518	34.4232	-3.7661	1.937	nan	FG	24.28	0.02	0.4	0.02	0.19	0.02
2540	34.4464	-3.7653	1.939	nan	FG	23.06	0.01	0.66	0.01	1.12	0.05
2554	34.4316	-3.7645	1.931	nan	FG	22.25	0.01	0.22	0.01	0.34	0.01
2568	34.4466	-3.7644	1.917	nan	FG	23.92	0.02	1.41	0.04	4.3	4.58
2598	34.4195	-3.7626	1.946	nan	FG	21.39	0.0	1.36	0.0	1.75	0.03
2612	34.416	-3.7631	1.933	nan	FG	22.08	0.01	1.4	0.01	1.68	0.04
2630	34.4743	-3.7636	1.926	nan	FS	23.73	0.03	0.07	0.03	0.05	0.02
2652	34.419	-3.7628	1.954	nan	FS	24.32	0.02	0.82	0.02	0.81	0.08
2655	34.4265	-3.7625	1.937	nan	FG	22.69	0.01	1.37	0.01	1.95	0.07
2666	34.4602	-3.7625	1.928	nan	FG	23.09	0.02	0.35	0.02	0.36	0.01
2675	34.4205	-3.7614	1.941	nan	FG	22.42	0.01	1.47	0.01	1.78	0.06
2700	34.4297	-3.7616	1.937	nan	FG	23.89	0.02	0.52	0.02	0.29	0.03
2715	34.4172	-3.7613	1.937	nan	FG	23.6	0.01	1.36	0.02	1.97	0.16
2727	34.4178	-3.76	1.935	nan	FG	22.77	0.01	0.43	0.01	0.29	0.01
2728	34.449	-3.7605	1.932	nan	FG	23.37	0.01	0.86	0.02	1.09	0.07
2769	34.4218	-3.7589	1.944	nan	FG	22.08	0.0	0.74	0.01	0.45	0.01
2771	34.434	-3.7592	1.926	nan	FG	22.73	0.01	1.53	0.03	1.19	0.1
2785	34.4362	-3.7594	1.939	nan	FG	24.18	0.02	1.56	0.05	2.77	0.73
2804	34.4538	-3.7584	1.926	nan	FG	23.77	0.02	0.62	0.03	0.79	0.07
3015	34.4456	-3.7514	1.931	nan	FG	23.47	0.01	0.52	0.01	0.48	0.02
3018	34.4519	-3.751	1.934	nan	FG	23.64	0.02	0.34	0.02	0.42	0.03
3064	34.4504	-3.7492	1.926	nan	FG	22.85	0.01	0.63	0.01	1.23	0.02
3065	34.4002	-3.7491	1.912	nan	FS	22.94	0.02	0.6	0.02	0.59	0.03
3350	34.408	-3.7367	1.878	nan	FS	22.69	0.01	0.22	0.02	0.29	0.02

Chapter 3

Properties of Galaxies in XLSSC 122, From Core to Outskirts

This chapter presents an updated photometric and spectroscopic catalogue of cluster members including new cycle 30 observations of the cluster outskirts out to 10 virial radii. With the addition of this data, I can observe the properties of member galaxies across a range of environmental densities, tracing how these galaxies are affected by their infall into the cluster environment. The inclusion of fields out past 10 virial radii of the cluster allow us to include a comparison to a region which approximates to the $z = 1.98$ field. With a single, well characterized cluster with a wealth of radio, x-ray, and optical observations I have a clearly defined dataset with which to compare the influence of a cluster environment on its member galaxies, from cluster centre to outskirts. In the following sections I show how a fast quenching model could describe the observed bimodal colour distribution of member galaxies in the cluster. I explore a model of ram pressure stripping as a potential cause for such rapid quenching. I also investigate the luminosity function of the red sequence galaxies in XLSSC 122, finding a consistent profile with other high redshift clusters. Finally, I look at the potential for infalling structures in the cluster, detecting no significantly overdense regions in the outskirts.

3.1 Cluster Membership and Spatial Distribution

Here, I identify and catalogue cluster members as described in Chapter 2. In XLSSC 122 I identify 63 gold members, 11 silver members, and 8 bronze members, adding 37 members in the gold and silver categories in addition to those found in Willis et al. (2020). These galaxies are added primarily in the regions observed by the most recent cycle 30 observations, but include a few galaxies in the cycle 25 region. This is because I have re-reduced the cycle 25 observations for consistency between objects. This density falloff can be observed in my map of the objects divided by category found in Fig. 3.1, which shows the distribution of cluster galaxies across the F140W observing fields. The highest concentration of cluster members still lies in the centre, corresponding to the cycle 25 data taken in 2017/2018, with a gradual drop off of object density into the cycle 30 data, with fewer objects in the farther fields. The falloff, though due in part to the decreasing density of cluster members with larger distance from cluster centre, is compounded with the reduced depth of the exposures in those regions.

One way of expressing the inner and outer behaviour of the density profile of a galaxy cluster is to use a double power law (Zhao, 1996).

$$\sigma_{DPL} = \frac{f_0}{(\frac{1}{x^a}) + (\frac{s}{x^b})}, x = \frac{r}{R_s} \tag{3.1}$$

Where $\sigma_{DPL}(r)$ is the surface density at a radius r from the cluster centre given a normalizing constant f_0, an inner slope a, outer slope b, smoothing factor s, and scale radius R_s. I first compare the total density over radius shown in Fig. 3.2, I also fit a double power law, as well as a NFW profile given in Equation 3.1. The total density over radius is the corrected number of objects inside of a corrected area drawn by a circle of radius R. The corrected number takes into account spectral completeness, such that each object counts as $\frac{1}{c}$, where c is the spectral completeness associated with the objects (interpolated) magnitude and exposure region. The corrected area is the area within the circle covered by the G141 filter. The resulting density then corrects for low density due to both spectroscopic incompleteness and regions with missing exposure. In the outer regions, a slope of -3.9 appears to fit the observed density over radius as fit with a double power law, with a more flat slope of -0.4 in the inner region. However, the NFW profile, which in projected space is expected to have a flatter slope in the inner regions and a slope of -2 in the outer regions, does not fit the observed number density over radius of cluster members. A lower number of objects in the outer regions could be influencing a good fit to a NFW profile, which is also used as a model of dark matter halo distribution. The high radius regions which are not well matched by the NFW profile fit are areas with lower exposure time, which could lead to a lower number of detected galaxies despite a treatment for spectroscopic incompleteness. The treatment of the galaxy number density over radius as a proxy for the dark matter distribution is mostly guided by the tendency for cluster members to trace the cluster NFW profile (Zwicky, 1933; Wang et al., 2018). I note however, that the variations in galaxy position, interaction histories, and dynamical effects such as ram pressure stripping, could lead to a collision or pressure influenced system which may not behave like the dark matter distribution.

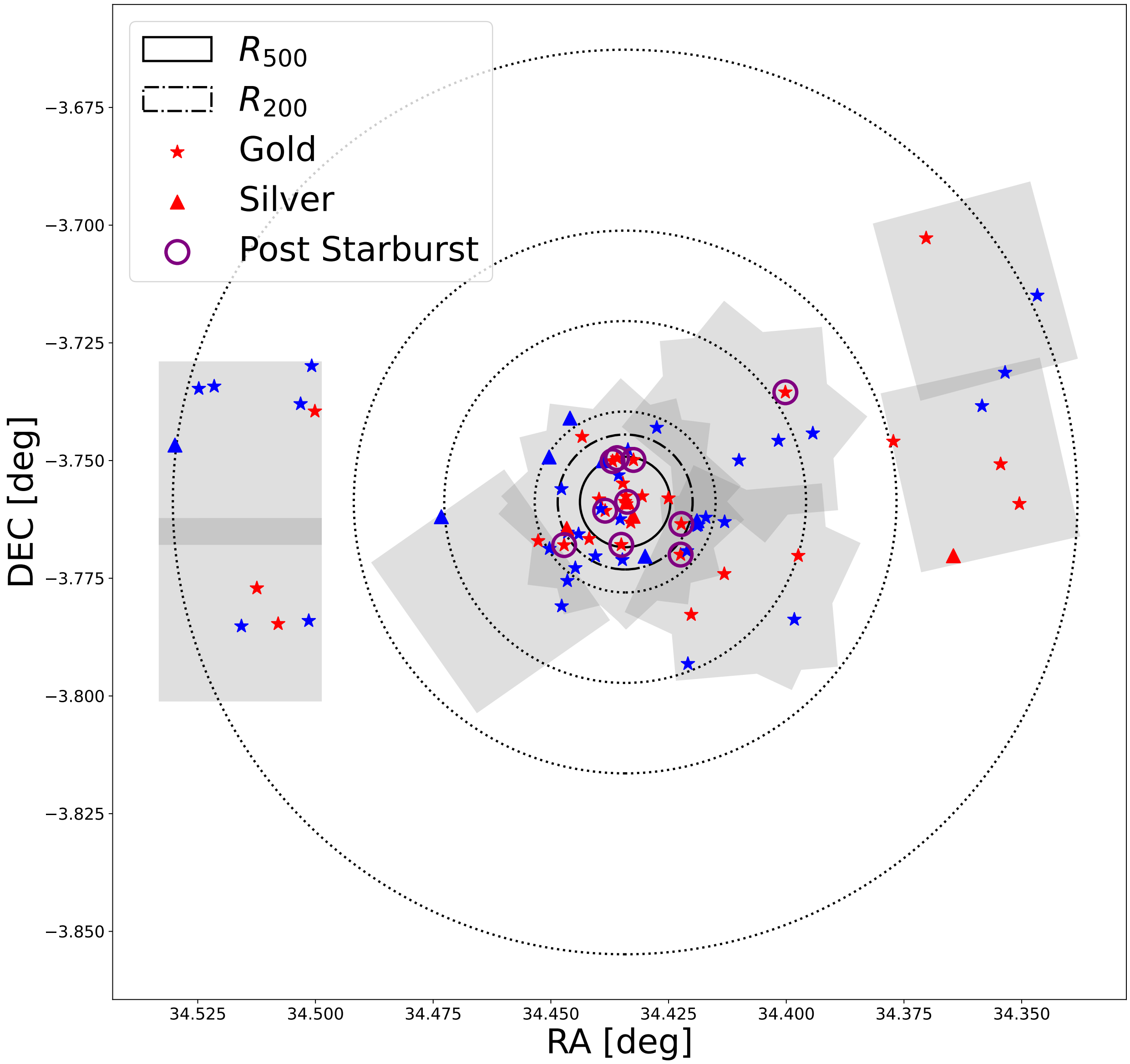

Figure 3.1: A map of XLSSC122's cluster members. The grey outlines indicate regions with G141 coverage, where spectroscopic cluster membership can be determined. Gold and silver members are shown as stars and triangles respectively. Cluster members are coloured red or blue based on the colour cuts in F105W-F140W = 1.15 in the central region, and F814W-F140W = 1.85 in the far regions. post-starburst galaxies are indicated by a purple circle.

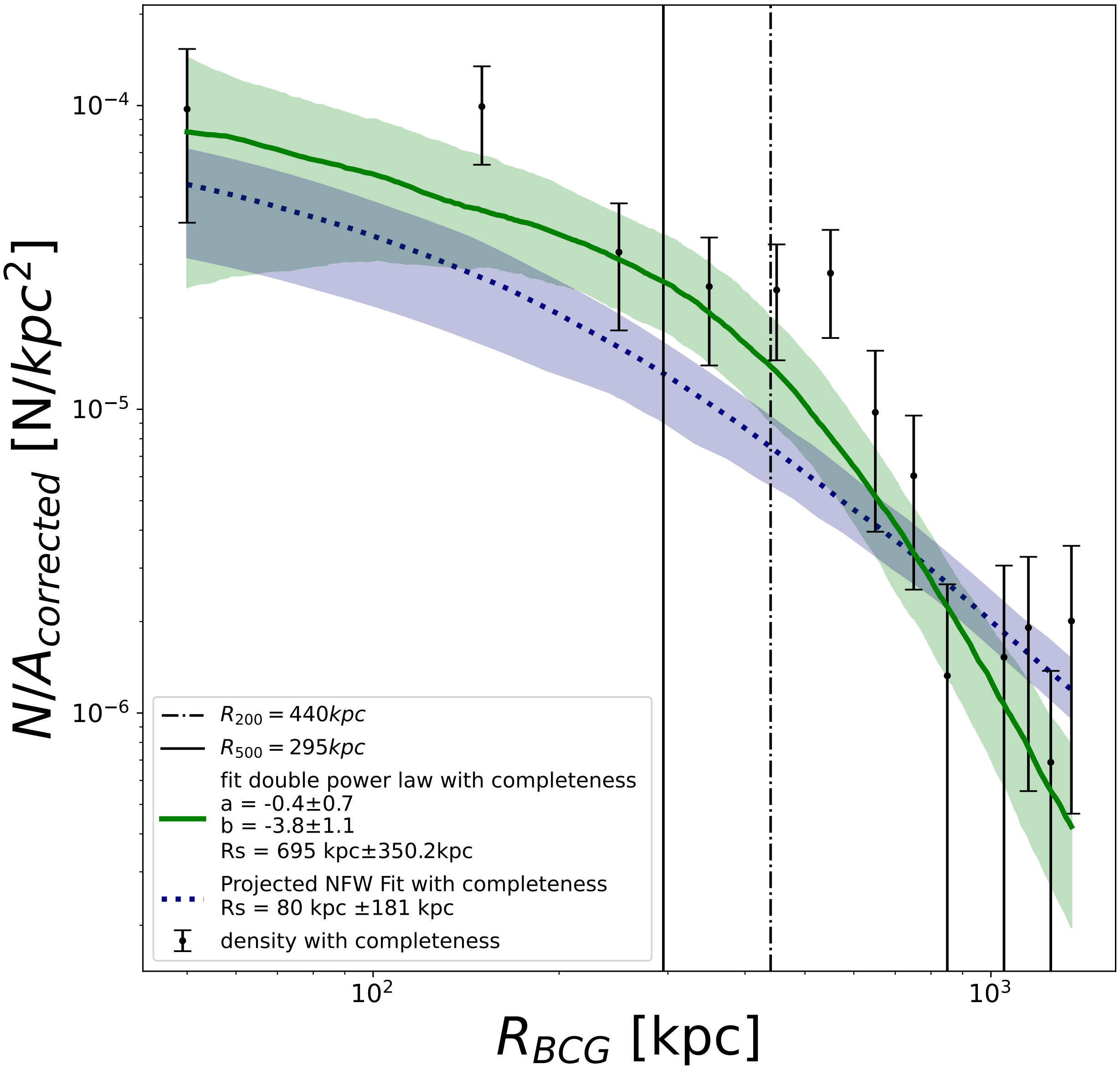

Figure 3.2: The number density of objects in XLSSC122 over the distance from the cluster centre. The density measured here takes into account the missing exposure area as well as spectroscopic incompleteness. A projected NFW profile (Navarro et al., 1997) (blue), and a double power law (green) are fit using a χ^2 goodness-of-fit estimate. I find an outer slope of b = -3.8 ± 1.1 and an inner slope of a = -0.4 ± 0.7 for a fit double power law best approximates the density profile. The fit NFW profile with $R_s = 80$ kpc ± 181 kpc does not have a steep enough distant slope to capture the data. Overlayed are $R_{500} = 295\,\text{kpc}$ and $R_{200} = 440\,\text{kpc}$. Errors are based on propagated $\sqrt{N}$ counting uncertainty.

I then compare the distribution of galaxies in the cluster based on radius and local density in order to determine if any local overdensities indicative of an infalling group or substructure are present. Local density is computed here as $\phi_5 = \frac{\sum_i^5 \frac{1}{c_i}}{\pi \cdot d_5^2}$, where d_5 is the transverse distance from the object to its 5th nearest neighbour and c_i is the spectroscopic completeness, similar to the total density case.

For the double power law I fit to the local density over radius as given in Fig. 3.3 I find a best fit inner slope of a = 0.0 ± 0.2, b = -1.6 ± 0.2, and R_s = 209 kpc ± 82 kpc. fits the data. The outer slope is steeper if the points are not adjusted for incompleteness.

3.2 Colour Bimodality and Red Fraction

The colour of an object is correlated with its stellar population, which is tied to the age of the object, the star formation history, merger history, and redshift. The colour as a function of magnitude in two different pairs of photometric bands is shown in Fig. 3.4 and Fig. 3.5, where I can identify the red and blue populations, and very few intermediate colour galaxies, consistent with other studies of high z galaxies (Strazzullo et al., 2016). These 2 populations are distinct and identifiable with a simple colour cut of F105W-F140W = 1.15 and less distinct but separable with a colour cut of F814W-F140W = 1.85 as used in Noordeh et al. (2021) for the CANDELS field, where the arbitrary colour cut of 1.85 is selected on the basis that their their analysis remains relatively unchanged for a cut 0.2 redder or bluer. Going forward I will be using both colours, with the idea that F105W-F140W has a more distinct red and blue separation, while F814W-F140W has coverage over all fields out to larger radii. The clear separation between colours, especially in F105W-F140W, which separates the red and blue starlight at $z = 1.98$, shows us two distinct stages in the star formation histories of the member galaxies. I see this in Fig. 3.7, where I show the median spectra between the red and blue populations. These spectra have been normalized to a common mean intensity in the rest frame 5200 Å range. I find a median rest frame [3800-4000 Å] region ≈ 3 times greater in the blue population than the red, the region where young blue stars are expected. I also observe the clear presence of O[III]5007 Å emission features in the blue spectrum twice as large as the underlying continuum of the red and blue galaxies. I conclude that these populations are drawn from 2 distinct stellar populations, the blue population containing younger stars with their O[III] emission features, and the red containing older stars with their lack of emission features.

I observe a change in red fraction from 0.44 to 0.78 in the relative number distribution of red and blue galaxies in XLSSC 122 over radius. The red fraction over radius is shown

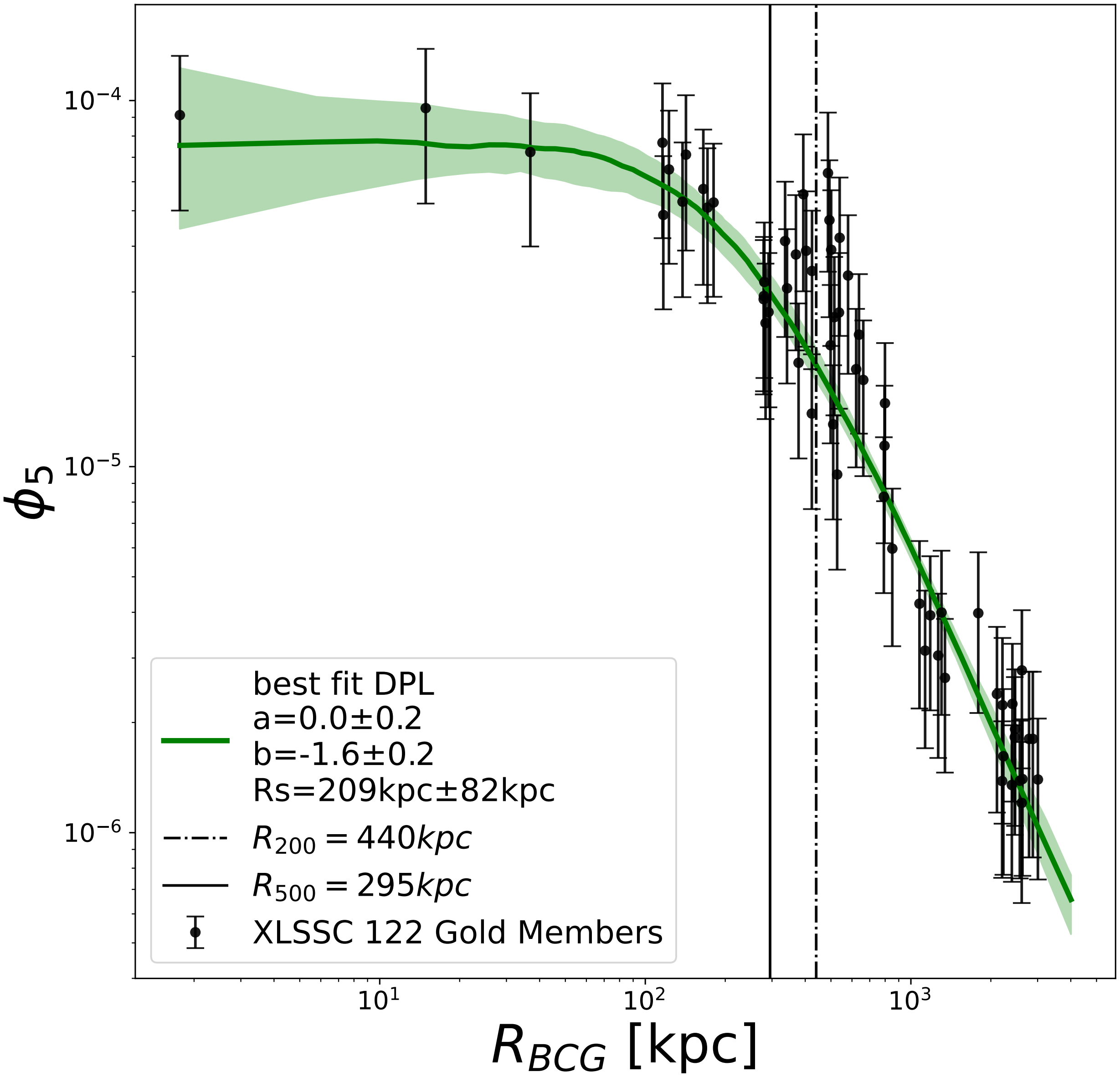

Figure 3.3: The incompleteness corrected ϕ_5 local density of each object compared to the distance from the cluster centre (scattered points). A double power law fit is shown in green, The solid line is the median, and the shaded region shows the 16th and 84th percentiles of a χ^2 goodness-of-fit estimate. The best fit line follows a = 0.0 ± 0.2, b = -1.6 ± 0.2, and R_s = 209 kpc ± 82 kpc. Overlayed are $R_{500} = 295\,\text{kpc}$ and $R_{200} = 440\,\text{kpc}$. Uncertainties in ϕ_5 are based on the propagated $\sqrt{N}$ counting uncertainty.

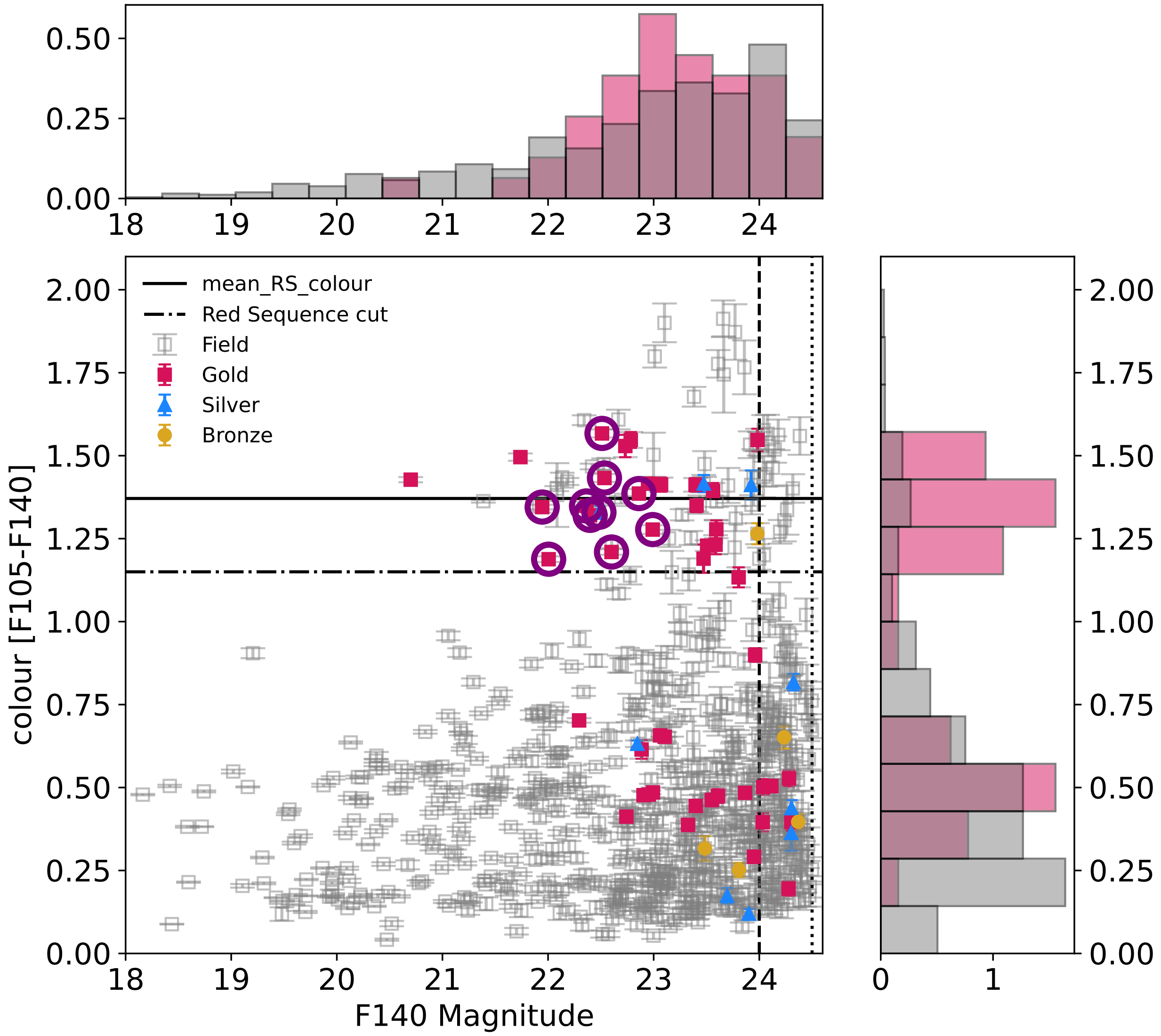

Figure 3.4: A Colour-Magnitude Diagram of the full XLSSC 122 photometric field. Red, blue, and bronze points are gold, silver, and bronze members respectively. Membership is spectroscopically estimated within $z = (1.96, 2.00)$. Grey points represent all photometrically extracted objects in the area. Vertical lines designate the 24 and 24.5 magnitude limits on cluster membership from prior core observations. The dash-dot horizontal line at 1.15 in colour indicates the red-sequence blue-cloud cut. The solid horizontal black line indicates the mean colour of the gold red sequence members. The histograms indicate the normalized number density of cluster members (red) vs non-cluster-members (grey) in intervals of 0.25 over colour and magnitude space corresponding to the CMD.

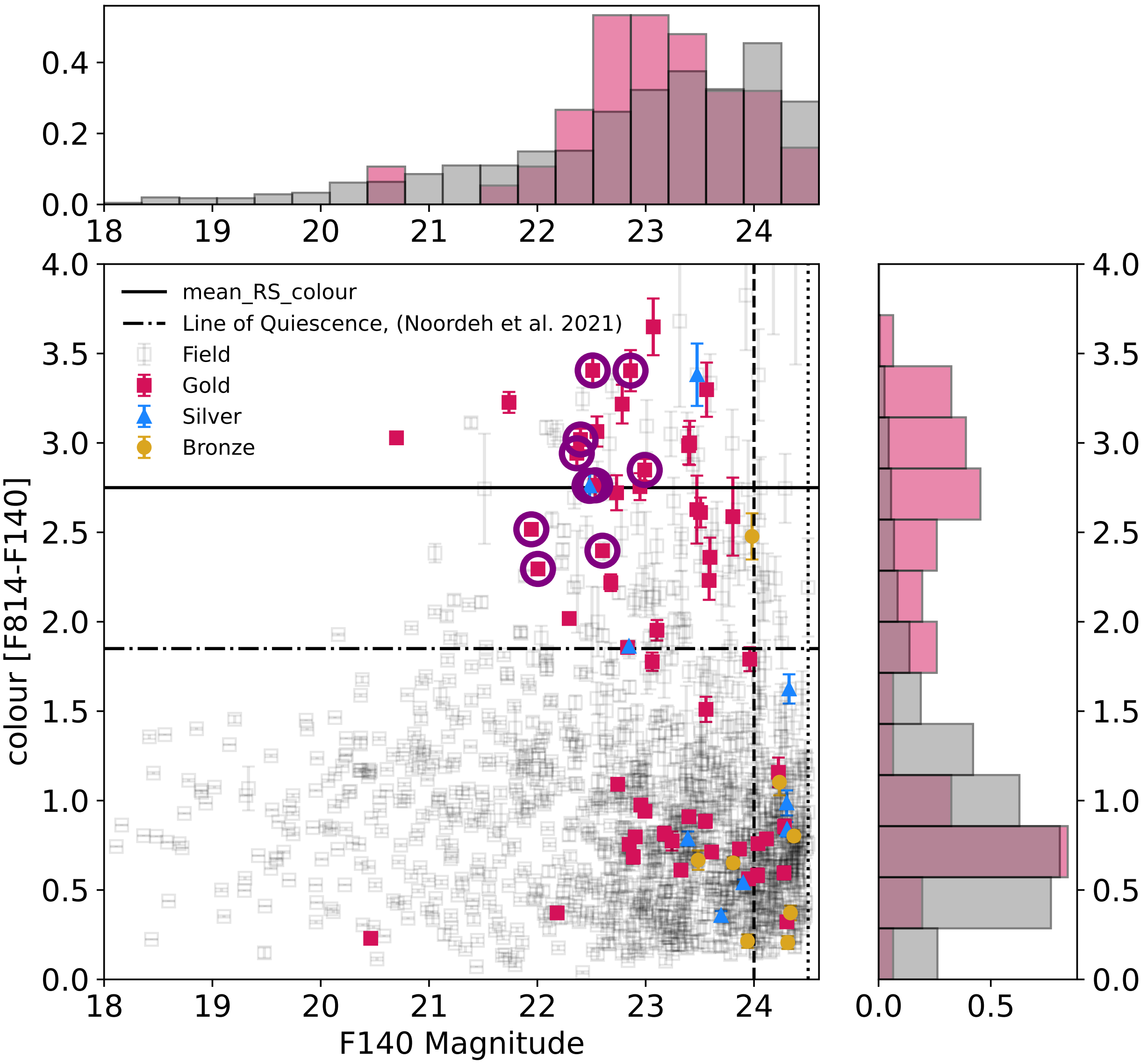

Figure 3.5: A Colour-Magnitude Diagram of the full XLSSC 122 photometric field. Red, blue, and bronze points are gold, silver, and bronze members respectively. Membership is spectroscopically estimated within $z = (1.96, 2.00)$. Grey points represent all photometrically extracted objects in the area. Vertical lines designate the 24 and 24.5 magnitude limits on cluster membership from prior core observations. The dash-dot horizontal line at 1.85 in colour indicates the red-sequence blue-cloud cut from Noordeh et al. (2021) given as a quenched cut. The solid horizontal black line indicates the mean colour of the gold red sequence members. The solid horizontal black line indicates the mean colour of the gold red sequence members. The histograms indicate the normalized number density of cluster members (red) vs non-cluster-members (grey) in intervals of 0.25 over colour and magnitude space corresponding to the CMD.

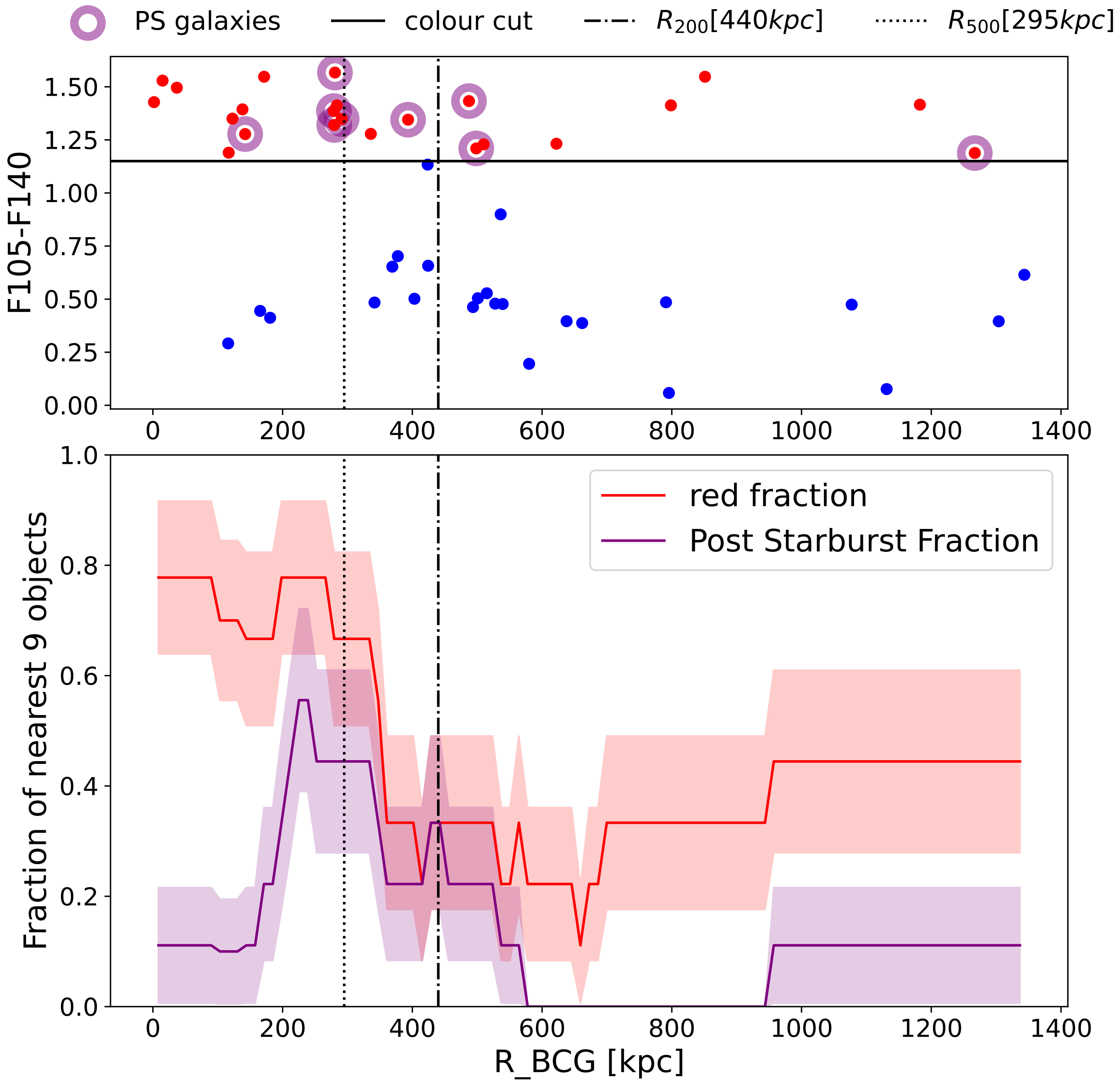

Figure 3.6: The red fraction and post-starburst fraction of galaxies in XLSSC 122 as a function of distance from the cluster centre. each point corresponds to the red fraction or post-starburst fraction of the 9 nearest galaxies to that radius. The red and purple regions indicate a 1 σ binomial uncertainty. The top panel shows each object's colour and radius, with red and blue points indicating red and blue galaxies as defined by a 1.15 colour cut. Objects with a purple circle are designated as post-starburst galaxies by a cut on $Hb > 0.1$ and $Hg > 0.3$

in Fig. 3.6 with the 2 colour cut populations, along with a scattering of the points in colour-radius space. I use a rolling bin method here to estimate red fraction, which helps to bridge the different scales in number density. I note that this red fraction varies with radius as seen in Noordeh et al. (2021) for galaxies in XLSSC 122. The red fraction nearly doubles within the virial radius from 0.44 ± 0.17 in the outskirts to 0.78 ± 0.14 in the core. Noordeh et al. (2021) use the CANDELS (Koekemoer et al., 2011; Brammer et al., 2012; Skelton et al., 2014; Momcheva et al., 2016) field to compare between the field and cluster environments. CANDELS is an HST field with galaxies in the $z = 1.9 - 2.1$ range taken with the F814W and F140W filters. The CANDELS field quenched fraction is reported as 0.20 ± 0.02 in Noordeh et al. (2021) when split along F814W-F140W $= 1.85$, which is lower than the quenched fraction observed at the very outskirts of XLSSC 122. However, the outer edges of galaxy clusters at $z > 1.4$ appear to experience quenching enhancements relative to galaxies in lower density environments (Werner et al., 2022).

I have observed that the fraction of red galaxies to total galaxies in XLSSC 122 varies as a function of radius, plateauing near the virial radius of the cluster. This may be the radius where interactions between infalling galaxies and the cluster environment lead to quenching, with a corresponding high red fraction. At the virial radius of a galaxy cluster, the galaxy is within an environment far more dense than the surrounding universe. This entry may send a pressure shock (ram pressure stripping) through the galaxy (Gunn and Gott, 1972; Brown et al., 2017). Though not the only quenching mechanism, dominant ram pressure stripping adds to the natural quenching occurring in galaxies over time. At z = 2, there is a high amount of star formation in galaxies as compared to z = 0 (Madau and Dickinson, 2014), but this reflects an average trend. Individual galaxies are interacting, consuming their star forming material, or otherwise experiencing quenching effects without the interference of a cluster environment.

3.3 Post-Starburst Galaxies

I classify 10 galaxies as post starburst out of the 63 galaxies in the gold category of the new catalogue of XLSSC 122. The median PS and non-PS populations are shown in Fig. 3.8. The PS galaxies show Balmer absorption and a lack of emission features, that, taken together indicate recent quenching in a star forming galaxy (Paccagnella et al., 2017). The non-PS galaxies do exhibit [OIII]5007 Å and H_β emission, but at lower intensity than the blue galaxy population shown in Fig. 3.7. This is not unexpected as both the old, quenched population, and the young, star forming population are combined into the non post-starburst category,

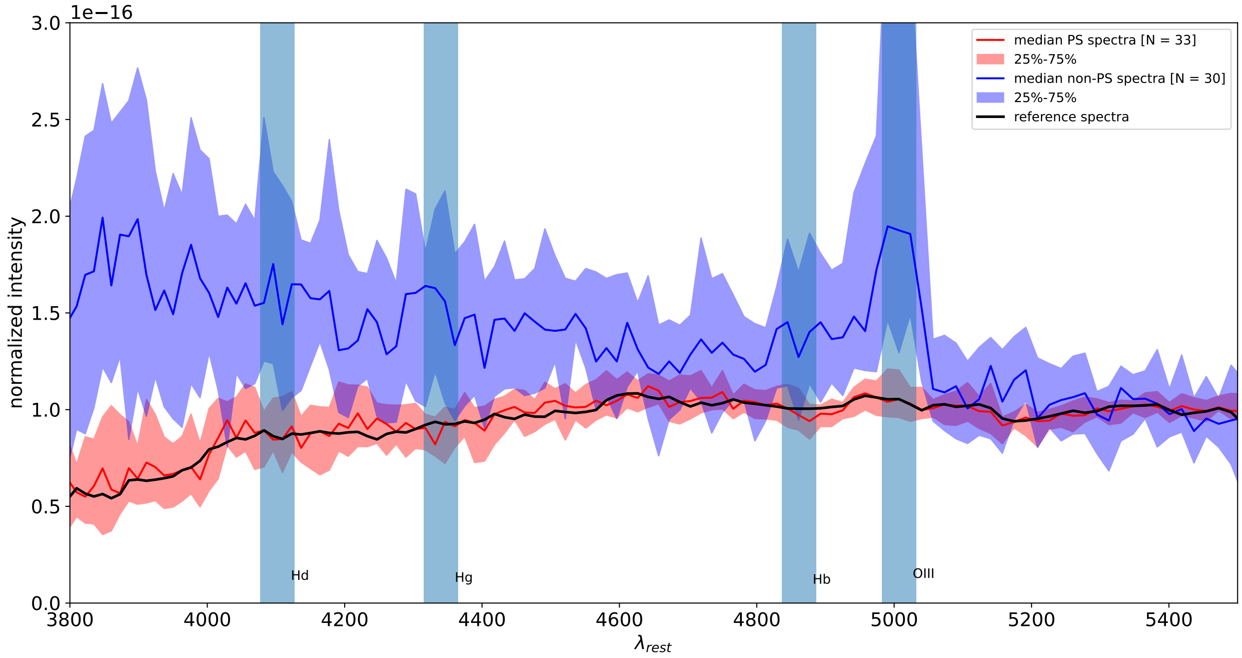

Figure 3.7: The sensitivity corrected and normalized spectra . The median red and blue galaxy spectra as divided by a cut of F814W-F140W = 1.85 for all 63 gold cluster members of XLSSC 122 are shown in red and blue respectively. All spectra are normalized to the BCG of XLSSC 122 (in black) at 5300 Å. Shaded regions indicate the 1st and 3rd quartiles.

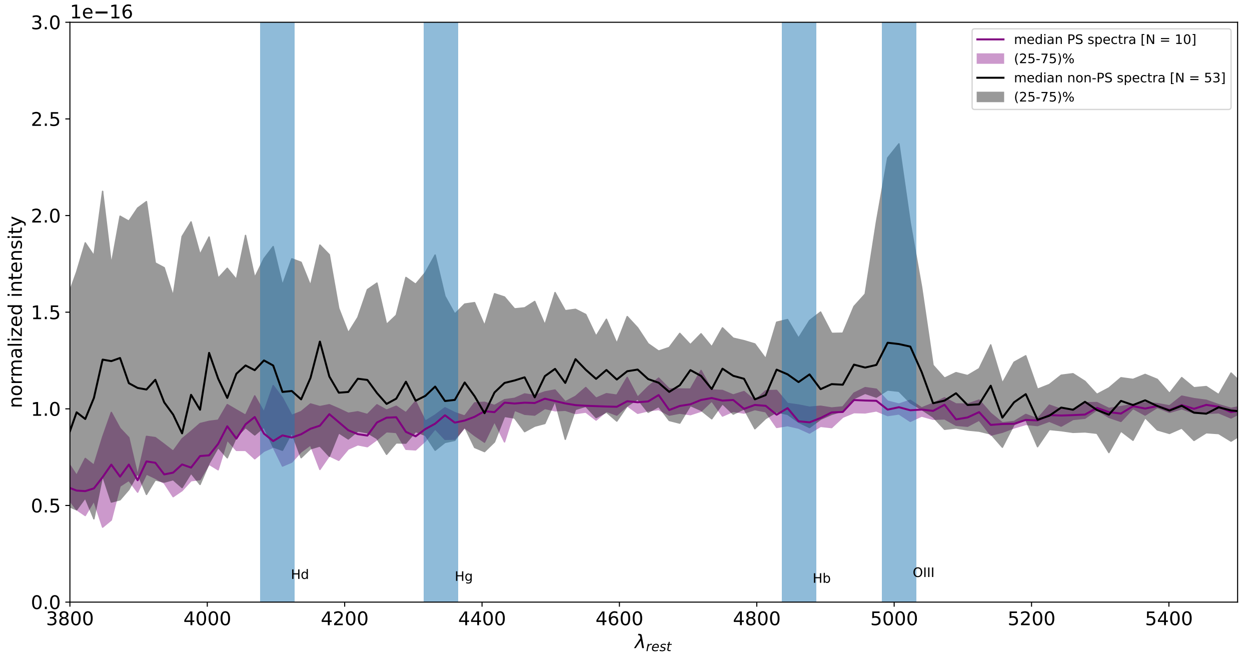

Figure 3.8: The sensitivity corrected and normalized median spectra for the gold members in XLSSC 122. The median PS and Non-PS galaxy spectra as divided by a cut of Hb > 0.1 and Hg > 0.3 shown in purple and black respectively. All spectra are normalized to the BCG of XLSSC 122 (in black) at 5300 Å

smoothing away the star forming features. The post-starburst vs cluster member fraction as a function of radius, as seen in Fig. 3.6, shows a peak in post-starburst fraction around the virial radius of XLSSC 122. This coincides with the radius of the red fraction increase, just within the virial radius. This coincidence could be explained with a rapid quenching theory, which I expand upon in in Sec. 3.4.1.

From Sec. 1.4, there is a decay time of about 500 million years between the cessation of star formation and the decay of most of the young stars. With the identification of post-starburst galaxies defined in Sec. 2.10 there are several galaxies classified as post starburst. There is an increase in the fraction of these post-starburst galaxies at around the same radius as the red fraction increase, shown in Fig. 3.6, further supporting the theory of star formation enhancement and rapid quenching of galaxies entering the cluster environment.

3.4 Red Sequence Luminosity Distribution

I compute the luminosity function in XLSSC 122's red cluster members in Fig. 3.9. The number of counts at each magnitude is the result of binning the magnitudes in the 3 different exposure time regions. I normalize by area, to account for the varying counting area of the 3 regions. Each magnitude point is then scaled by a factor of $\frac{1}{c}$, where c is the interpolated completeness at that magnitude and exposure time. The 3 scaled luminosity functions are then added together to form Fig. 3.9. I then fit a Schecter function in magnitude space shown in Eq. 1.6 (Schechter, 1976) using a χ^2 goodness-of-fit test sampled with an MCMC walker set.

I provide a comparison to the luminosity function of other clusters at z $\approx$ 1 from Chan et al. (2019) in Fig. 3.9. I perform a correction between the F140W [1.4 μ] filter and the rest frame F160W [1.5 μ] HST filter to estimate the H band used in Chan et al. (2019). I find a correction factor including both distance modulus and k correction of -45.767 from $m_{\mathrm{F140W},z=2}$ to $M_{\mathrm{F160W},z=0}$ using an old stellar population template from Brammer et al. (2008). The scale magnitudes for the GOGREEN galaxy clusters, both high and low mass, are about 1 magnitude smaller than the XLSSC 122 fit scale magnitude. This implies that the largest galaxies in XLSSC 122 are 1 magnitude dimmer than the largest galaxies in GOGREEN, or $\approx$ 2.5 times as massive assuming a fixed mass to light ratio. GOGREEN clusters have an M_{200} halo mass of about $2 \times 10^{14}\ M_{\odot}$ for low mass clusters and $6.5 \times 10^{14}\ M_{\odot}$ for high mass clusters (Chan et al., 2019). Considering $M_{500} = 6.3 \times 10^{13}\ M_{\odot}$ for XLSSC 122, the GOGREEN low mass galaxy clusters are about 3 times more massive than XLSSC 122, and the GOGREEN high mass galaxy clusters are about 10 times more massive. These

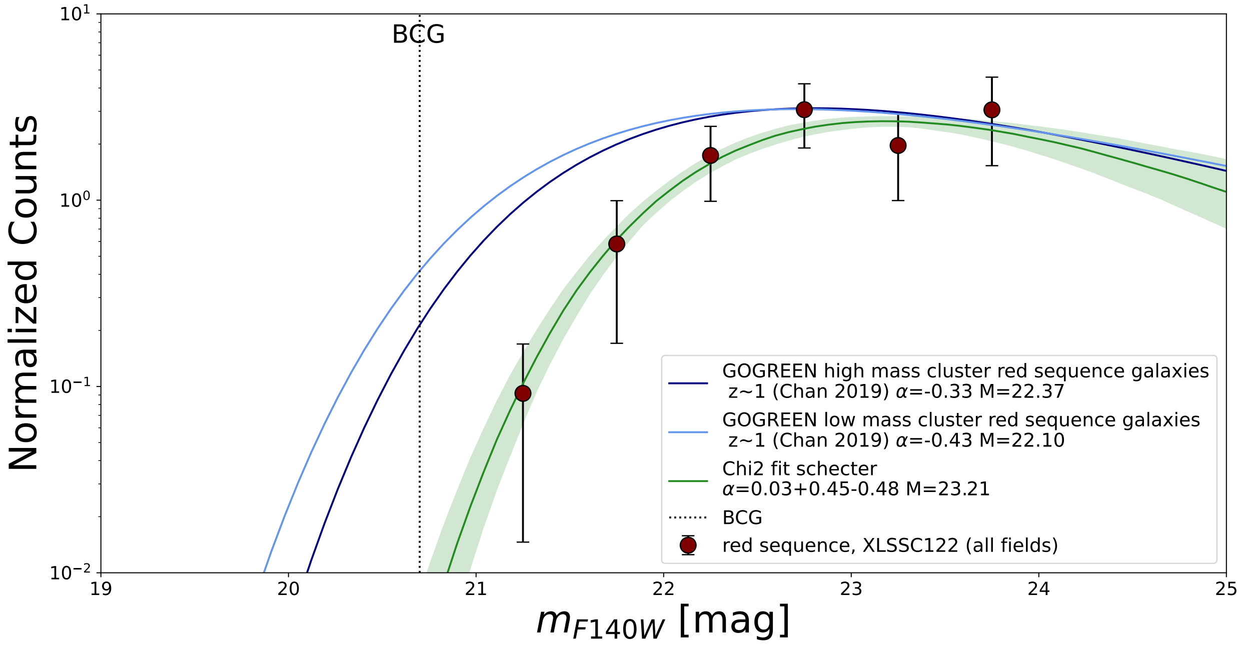

Figure 3.9: The H band completeness and area corrected rest magnitude luminosity (maroon) fit with a Schechter (1976) function as given in Eq. 1.6 (green). Uncertainty on counts is propagated from the combined Poisson counting uncertainty. The green shaded region indicates the 16th and 84th percentiles of the Schecter χ^2 goodness-of-fit final walker positions. Curves are normalized for comparison.

ratios are also overestimates, as GOGREEN clusters are measured in M_{200}. The observed difference in scale magnitudes is on the scale of the difference in halo mass between the clusters.

Comparing this luminosity distribution, to the stellar mass distribution of galaxies in the GOGREEN survey (van der Burg et al., 2020), I see a downwards slope in the low mass tail, consistent with their trend for quiescent galaxies in cluster environments. This downward slope does extend into a region of high incompleteness (<50% for the medium and low exposure time regions past F140W = 23.5) and is sensitive to small variations in the count or completion correction. I have altered the binning and interpolation method of the incompleteness, finding that the resulting low mass slope varied between $\alpha = 0.5$ and $\alpha = -0.5$. I am assuming here that the mass to light ratio is relatively consistent between red galaxies. The luminosity distribution of XLSSC 122 is similar to galaxy clusters at a lower redshift, with similar low mass slope and a scale magnitude that is consistent with the mass difference between clusters. It appears then that XLSSC 122 has a galaxy population which evolves at similar mass and luminosity ratios to mature clusters at lower redshift. This indicates that XLSSC 122 may be a mature galaxy cluster, at a farther stage of its evolution than other clusters at $z = 2$.

3.4.1 Environmental Quenching in XLSSC 122

I measured the red fraction and post-starburst fraction in XLSSC 122, tracing the evolution of galaxies as a function of the distance from the cluster BCG. I observe an increase in the red fraction and PS fraction in Fig. 3.6 corresponding to a density increase seen in Fig. 3.2. In other words, XLSSC 122 member galaxies in denser environments are more likely to be red, and there is a density and radius range where post-starburst features are most prevalent. For comparison, clusters in the local universe appear to quench galaxies during infall (Werner et al., 2022), which could lead to an enhanced population of post-starburst galaxies at a distance from the cluster centre (McNab et al., 2021). In order to investigate whether the observations in XLSSC 122 are consistent with this scenario, I follow the model of ram pressure stripping given in McCarthy et al. (2008) to estimate whether ram pressure stripping is consistent with the observed post-starburst galaxy appearance at this radius in this cluster. Mechanisms such as galaxy-galaxy interaction, AGN and stellar heating, or the heating of the CGM may have a quenching effect, but occur over longer time scales (Dressler, 1980; Peng et al., 2010).

XLSSC 122 has an estimated average temperature of $\mathrm{kT} = 5 \pm 0.7\,\mathrm{keV}$ (Mantz et al., 2018). An individual ionized particle within the virial radius would follow the kinetic theory of gasses in thermal equilibrium, with a three dimensional velocity equal to $\sqrt{3}\sigma_v$, where σ_v, the velocity dispersion, is given in Eq. 3.2

$$\sigma_v^2 = \frac{kT}{\mu m_p} \tag{3.2}$$

derived from equating the kinetic and thermal energy of the gas shown in Eq. 3.3.

$$\frac{1}{2}m < v^2 >= \frac{3}{2}kT \tag{3.3}$$

Here, μ is the mean molecular mass, and m_p is the mass of a proton. For, XLSSC 122, I use $kT = 5000\,\mathrm{eV}$, $\mu = 0.608$ (H:He = 3:1), and $m_p = 1.602 \cdot 10^{-27}\,\mathrm{kg}$ (Mantz et al., 2018). With this, I find $v_{vir} = 1500\,\mathrm{km/s}$. I will assume that at any radius $r < r_{vir} = 440\,\mathrm{kpc}$, $v = v_{vir}$, and for any $r \geq r_{vir} = 440\,\mathrm{kpc}$, $v = \frac{v_{vir}}{\sqrt{r/r_{vir}}}$. I use the ram pressure stripping condition from McCarthy et al. (2008), given in Eq. 1.7. Galaxies in cluster environments with infall velocities of $v > 1000\,\mathrm{km/s}$ indicate signs of ram pressure stripping at the virial radius in some circumstances, as seen in Hansen et al. (2007).

I use the ICM density profile as found by Mantz et al. (2018), the velocities I calculate above and ρ_{gas} from Eq. 1.9 with scale radius $r_d = 3.5\,\mathrm{kpc}$. From previous studies of the cluster core (Trudeau et al., 2022) I know the general stellar masses of the galaxies in XLSSC 122. Using this and a conversion from stellar mass to halo mass from Behroozi et al. (2013b,a) for galaxies at $z = 2$, I can estimate the mass profiles of infalling galaxies. I use an NFW profile (Navarro et al., 1997) with a varying scale radius Rs from van der Wel et al. (2014) given in Eq. 3.4.

$$R_{eff,z=2} \approx \left(\frac{M_*}{5 \times 10^{10} M_\odot}\right)^\alpha \tag{3.4}$$

Here R_{eff} is the effective radius of the stellar mass according to a Sersic (1968) profile, α is a mass scaling parameter. At $z = 2$, I use $\alpha = 0.6$ for spherical galaxies, and $\alpha = 0.76$ for disk galaxies, from the fits to observations from van der Wel et al. (2014). I use a Sersic index n = 1.5 for both galaxy types (Shibuya et al., 2015). For the NFW scale radius, $R_s = \frac{R_{vir}}{c}$. I use the evolution of the concentration parameter c from Dutton and Macciò (2014), which at $z = 2$ can be estimated by $c \approx 10^{0.65}\left(\frac{M_h}{10^{12} M_\odot}\right)^{-0.05}$. For the virial radius one can approximate a virial halo at $R_{vir} = R_{200}$, with resulting mass $M = 4\pi R_{vir}^3 \rho_{crit} \Delta_c / 3$ (Mo et al., 2010) with $\Delta_c = 200$. Thus, $R_{vir} \propto M^{-\frac{1}{3}}$. I will assume that the virial radius can then be estimated at z = 2 by Eq. 3.5 derived from Mo et al. (2010).

$$R_{vir,z=2} \approx \frac{200}{3}\left(\frac{M_{vir}}{10^{12}M_{\odot}}\right)^{\frac{1}{3}} \tag{3.5}$$

Here, M_{vir} is the mass contained within the virial radius. The constant of 200 is for $z = 0$, and the factor of $1 + z = 3$ comes from the scaling of the Hubble parameter with redshift. I consider the gas profile for the galaxies I model using Eq. 1.9. I show the change in stripping radius as a function of clustercentric distance in Fig. 3.11. In this case I have chosen three galaxies with masses spanning the range of estimated stellar mass of XLSSC 122 cluster members from Trudeau et al. (2022). post-starburst galaxies identified near the virial radius have magnitudes between 22 and 23 in F140W. Given the mass to light conversion in Fig. 3.10 from Trudeau et al. (2022), these post-starburst galaxies currently lie between the $\log(M_*) = 10.25$ and $\log(M_*) = 11$ galaxies in Fig. 3.11. With the three example galaxies, I find the stripping radius of the lowest mass ($log(M_*) = 9.24$) is $< 100\,\mathrm{kpc}$ once it has reached $\approx 650\,\mathrm{kpc}$ from the cluster centre. And is stripped to $< 5\,\mathrm{kpc}$ shortly after R_{500}. This suggests that the lowest mass galaxies in XLSSC 122 under this model lack a star formation reservoir in the CGM or outer ISM once they enter the cluster virial radius. An intermediate mass galaxy ($log(M_*) = 10.25$) is stripped past 10 kpc at R_{500}, and does not strip within 5 kpc until it hits the centre. It would require further work to estimate how much of an effect this partial loss of gas envelope would have on the star formation and prevalence of post-starburst features in the galaxy. Finally, a high mass galaxy ($log(M_*) = 11$) does not begin stripping past 10 kpc until it is 100 kpc from the cluster centre, and may have lost a sizable amount of its outer gas reservoir by the time post-starburst features are observable, but no stripping of the inner 10 kpc until close passage into the cluster. The picture painted by these models would appear to support the effects of ram pressure stripping on the medium to low mass galaxies in XLSSC 122 past the virial radius of the cluster, as noted in galaxy clusters in the local universe for galaxies $M_* \approx 10^{8-9}M_{\odot}$ (Moretti et al., 2022) galaxies and $M_* \approx 10^{10}M_{\odot}$(Poggianti et al., 2017; Boselli et al., 2019) galaxies. Further, strong ram pressure stripping seems unlikely, consistent with a lack of galaxies with strong post-starburst features.

Observationally, the depletion of the CGM and thus the removal of the gas supply for star formation, can deplete a low mass ($log(M_*) \approx 10$) galaxy in less than 1 Gyr (van der Burg et al., 2018). The stripping of the CGM, as well as the molecular and atomic ISM of galaxies of stellar mass $log(M_*) \approx 10 - 11$ has also been observed upon infall into cluster environments in the Virgo cluster, which is an environment with a similar density, if not

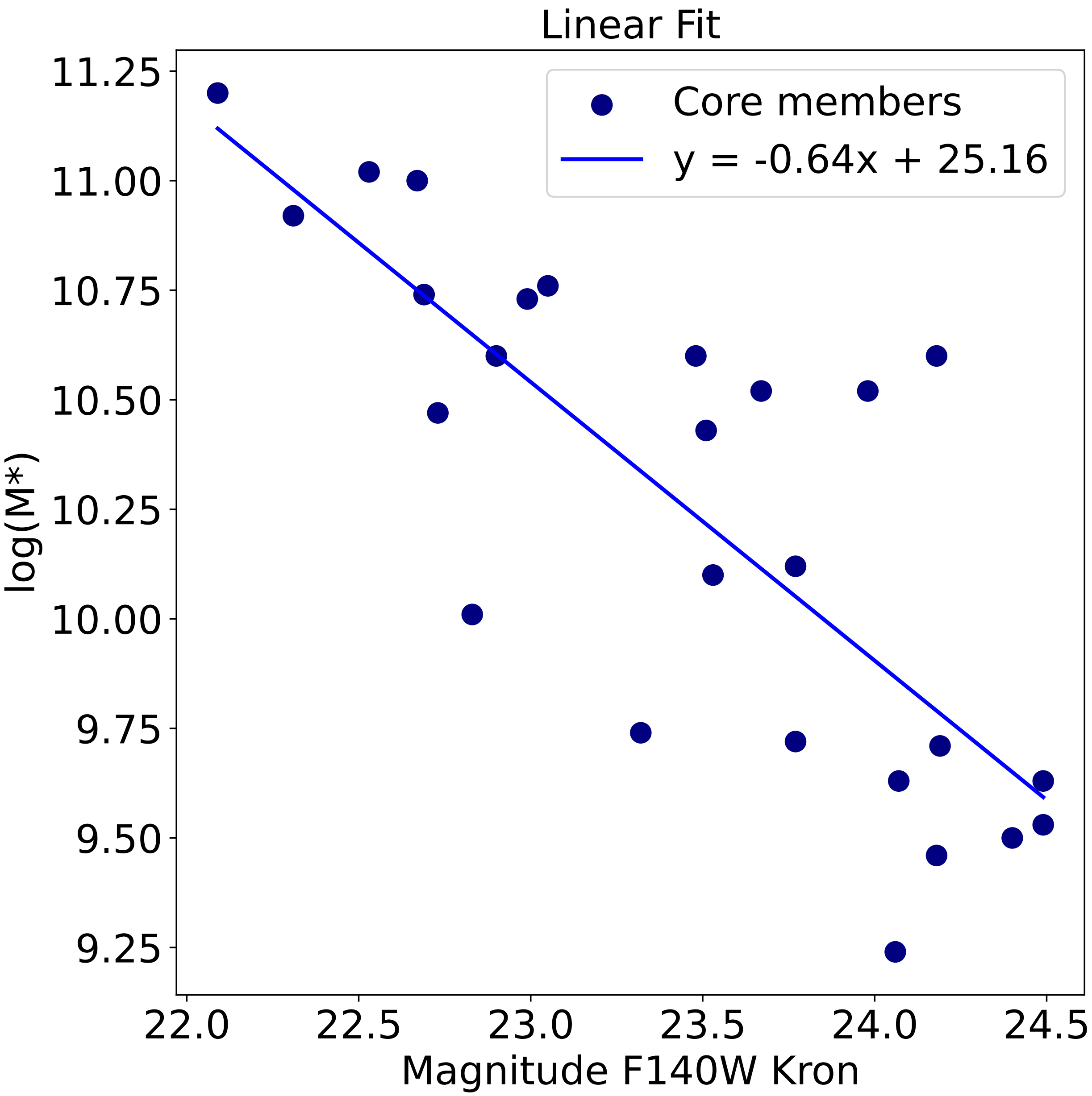

Figure 3.10: Magnitude to stellar mass of galaxies from Trudeau et al. (2022) (navy) with an overlayed best χ^2 fit line (blue).

infall velocity (Watts et al., 2023).

Consider the case of ram pressure stripping galaxies in the Virgo cluster (Crowl and Kenney, 2008), where galaxies have identifiable PS features with stripping radii of $\approx 3-5\,\mathrm{kpc}$. In XlSSC 122, it appears that the low mass galaxies may experience this level of stripping if within $r < 100\,\mathrm{kpc}$, whereas, a galaxy of mean mass compared to the cluster members of XLSSC 122 will never experience this level of stripping, but will lose its gas reservoirs with a stripping radius of 10 kpc at a distance of 200 kpc to the cluster centre.

3.4.2 Lack of Filamentary Structure or Infalling Groups in XLSSC 122

Within a filamentary structure of dark matter, containing galaxies tracing its extent (Bond et al., 1996), one might expect to see streams or clumps of galaxies entering into a cluster environment over time, as observed in the local group (Kraljic et al., 2018), and out to $z = 1.1$ (Okabe et al., 2019). These groups would be local overdensities of galaxies offset from the cluster centre, as seen in Dressler et al. (2013). Before entering into a cluster environment, these galaxies would already exist in a range of overdense regions, experiencing a cluster-like pre-processing, or accelerated evolution (Fujita, 2004). In the local universe, environmental pre-processing in filaments and groups prior to infall into a cluster has been observed (McNab et al., 2021).

As seen in Fig. 3.12 I find that the local galaxy density falls off with radius in a manner consistent with a double power law as given in Eq. 3.1, with a small peak around the virial radius. The locations of these objects with high local density are shown in Fig. 3.12, where they occupy two distinct locations. These objects, although the most overdense in comparison to a radial density falloff, are not strong indicators of a local structure. However, the local density estimate ϕ_5 relies on their being at least 5 objects in an overdensity to appear as a strong overdensity, so smaller overdense regions could be missed by this simple estimate. Out intention here is to provide a simple test of whether there is a clear overdensity of galaxies that does not follow the radial density falloff of the cluster itself. Considering the low number sample of galaxies and photometric and spectroscopic measurements taken in multiple exposure time ranges, I did not consider a 2σ overdensity sufficient to identify if there is or isn't a substructure falling in to XLSSC 122.

The spherically symmetric galaxy number density profile of XLSSC 122 may indicate that XLSSC 122 is not relying on an infall of material from a cosmic filament, but has already carved out its own space, in which it has been evolving for a considerable portion of the age of the universe before observation. However, I note that this non-detection relies on a

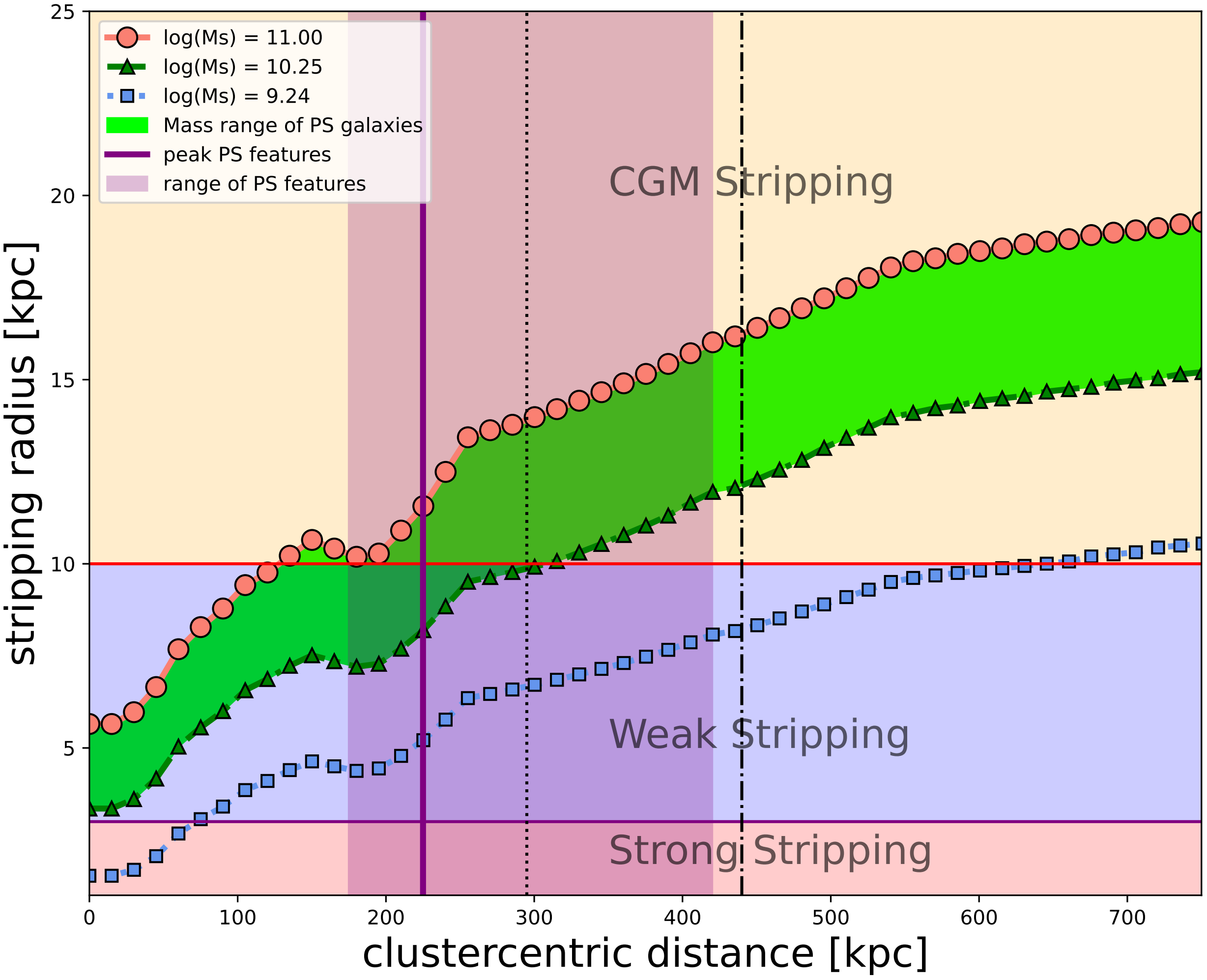

Figure 3.11: Ram pressure stripping radius for a variety of input galaxy masses. Overlayed are $R_{200} = 440\,\mathrm{kpc}$, $R_{500} = 295\,\mathrm{kpc}$, and the peak of PS features and approximate range of visible PS features as seen in Fig. 3.6. The lime region indicates the mass range in which PS galaxies are found in XLSSC 122. Shaded vertical bands are place at rough boundaries. Stripping within 3 kpc is present in many ram pressure stripped and post-starburst galaxies with clear features. Stripping within 10 kpc has removed the CGM gas reservoir required for star formation, and is cutting into the current star forming material. Anything from 10 kpc to 100 kpc is stripping the CGM, and probably won't add to a rapid quenching until it gets close to the stellar component, but still contributes to an accelerated quenching timescale. Anything past 100 kpc still retains a CGM for plenty of star formation.

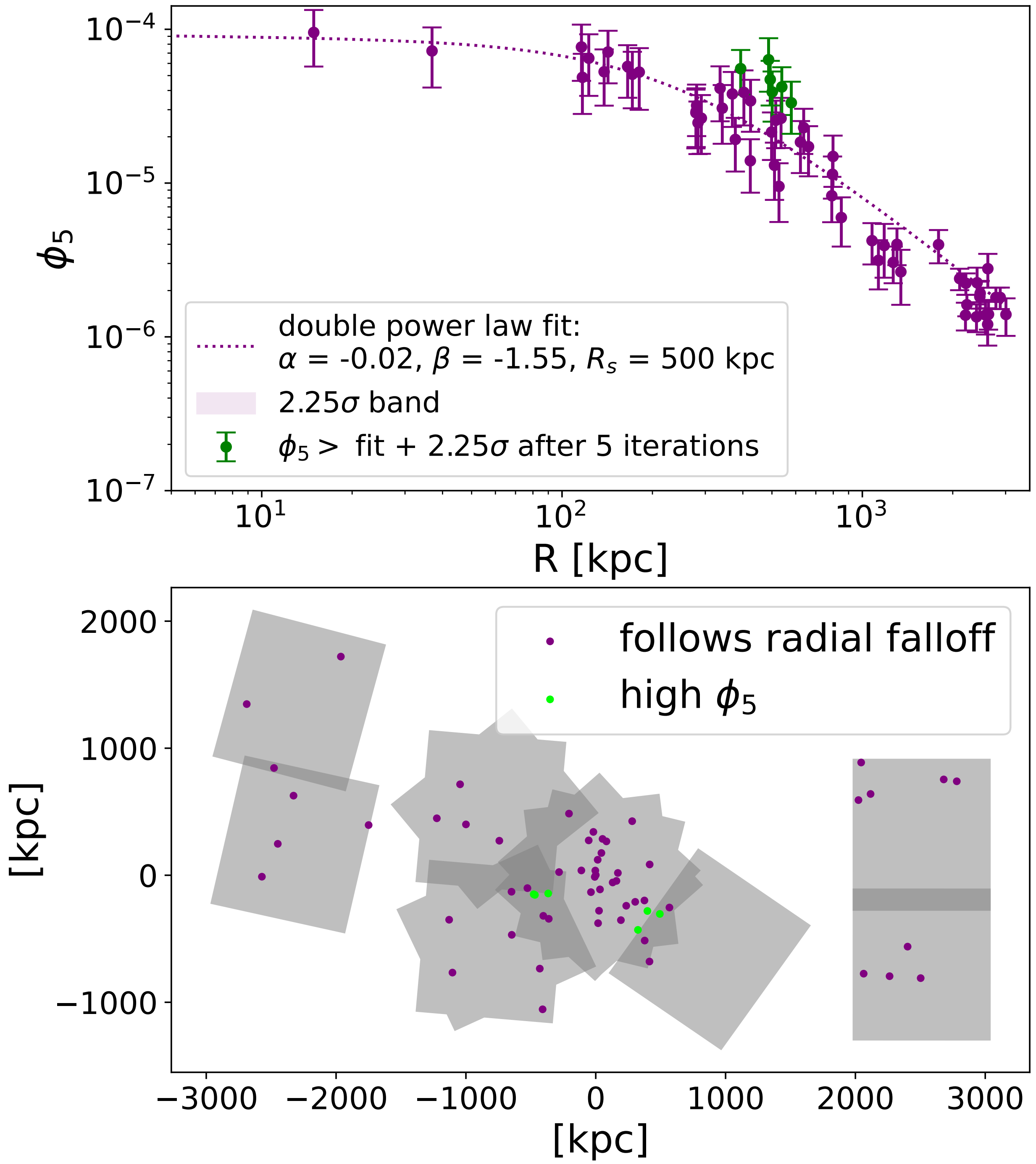

Figure 3.12: *Top*: The number density of objects in XLSSC122 over the distance from the cluster centre. The density measured here takes into account the missing exposure area as well as spectroscopic incompleteness. A double power law (purple) is fit using an iterative χ^2 goodness-of-fit estimate similar to Fig. 3.3. The iterative portion removes any object more than $2.25\sigma_{\phi_5}$ from the fit line (green) for future fits. *Bottom*: A map of XLSSC 122 cluster members, showing the location of the high ϕ_5 (green) objects compared to those who follow the double power law radial falloff (purple).

measure of local density requiring 5 closely spaced galaxies, the majority of which will be low brightness galaxies of F140W magnitude > 22, as seen in Fig. 3.9. At larger radii, past R_{200}, an infalling group or filament could exist within a region with low completeness. I have estimated the incompleteness in the inner regions, with more confidence in the NW and SW regions, and folded it into the estimate of local density given in Fig. 3.3, and similarly find no significant overdensity.

3.5 Summary and Conclusion

In this section I present an updated and expanded photometric and spectroscopic catalogue of galaxies within the cluster XLSSC 122. This catalogue contains new information out to $10R_{vir}$ of XLSSC 122. I trace radial colour, post-starburst galaxy classification, and density relations. In summary:

1. I have increased the total number of spectroscopically confirmed cluster members to 74 in the Gold and Silver member categories for XLSSC 122.

2. XLSSC 122 contains a high fraction of red galaxies overall at $49\% \pm 12\%$, with upwards of 80% red fraction within the closest 9 galaxies to the BCG. For comparison, the Virgo cluster has a core red fraction of 90% (Roediger et al., 2017).

3. The clear colour bimodality indicates a rapid cessation of star formation upon entry into the cluster environment, with a strongly quenched core population.

4. Given the apparent spherically symmetric arrangement of cluster galaxies around the core, I do not report a detection of any infalling groups or filaments. If there is no infalling structure, this would imply that XLSSC 122 is a mature galaxy cluster which has entered into a more relaxed state.

5. I observe an increase in post-starburst fraction at the virial radius. This could indicate the prevalence of a ram pressure stripping quenching mechanism, an environmental quenching mechanism not typically expected to be a dominant quenching mechanism in the early universe. I use a toy model of ram pressure stripping and find the observed post-starburst features are consistent with a ram pressure stripping scenario leading to starvation in middle to high mass galaxies, and rapid quenching for low mass galaxies.

6. The coinciding red fraction increase upon approaching the cluster core shows that these galaxies quench fast and stay quenched. The falloff of post-starburst members near

the centre of the cluster implies that these galaxies have not had recent star formation. Since I have detected post-starburst galaxies elsewhere with the same G141 footprint depth, it appears that these galaxies have been quenched for longer than the detection time of a post-starburst galaxy, or at least 0.5 Gyr (Werle et al., 2022).

Chapter 4

Future Work

The creation of a full photometric and spectroscopic catalogue was the primary focus of this work. However, a much more extensive investigation of XLSSC 122 can build off this catalogue.

4.1 Improving the Pipeline of Cluster Membership

When creating the cluster catalogue, I made use of G141 observations treated as individual regions between targets. However, some galaxies lie in the space between 2 or even 3 fields. In my estimate of spectroscopic completeness, I am likely missing several galaxies due to the completeness level in the lowest exposure time regions. By combining these regions and stacking their observed spectra, a higher signal-to-noise ratio, and higher rate of detection would be achieved. I opted not to risk the addition of beams due to the difficulty in aligning objects between fields. By aligning each set of grism exposures to the same common reference, one could increase the number and or clarity of cluster members in the outskirts regions.

During the acquisition of the cycle 30 data, the HST failed to acquire guide stars which rendered several exposures unusable. A request for additional F105W exposures in the outer regions was made in response to the failure. F105W photometry, not present in the outer regions, is low in time cost and will allow for a direct colour comparison for the most distant galaxies from XLSSC 122.

4.2 New Observations of XLSSC 122

A study of the cluster core (Trudeau et al., 2022) estimated the star formation histories of member galaxies, finding that some red galaxies in the core formed most of their stars in the very early universe. The star formation history estimate presented there, accounting for different instruments and filters, was outside the scope of this work. A more complete investigation of the cluster member star formation histories for outskirts galaxies, however, would help explain when these galaxies formed stars. A future study could look at the variation in estimated age and characteristic time from the cluster core to outskirts. Are there a high number of old galaxies in the cluster core compared to the outskirts? If some galaxies in the cluster core formed their stars quickly in the early universe, then is the same true for outskirts galaxies, and is this shift connected to the changing density environment?

The current spectroscopic information from the G141 grism, though a powerful redshift estimator at $z = 2$, lacks the fine resolution required to accurately trace the star formation histories of these galaxies. The identification of galaxies with post-starburst features such as absorption lines was difficult with the low signal-to-noise ratio of these low resolution spectra. With a higher resolution infrared spectrograph one could make a post-starburst classification with more certainty, and identify spectroscopic members, especially those with strong emission lines, with greater certainty. Additionally, higher resolution data would allow a more precise prediction of the galaxy star formation histories (Slob et al., 2024) through stellar population synthesis model fitting (Conroy et al., 2009; Conroy and Gunn, 2010). Specifically, the James Webb Space Telescope is the only space-based instrument capable of this task, as ground based spectroscopic instruments are unable to acquire spectral observations of sufficient signal-to-noise down to a magnitude of 24.5, and the JWST NIRSpec instrument has a high enough spectral resolution to properly sample the velocity dispersion to a rest frame velocity of 100 km/s. Such an observation with JWST NIRSpec's G140M/F100LP filter pair would provide a spectral resolution an order of magnitude higher than the HST G141/F140W filter pair used in this work covering rest frame Balmer lines, O[III]5007 and O[III]4959, and D4000. Such an observation, in addition to providing a better estimate of star formation histories of some of the first galaxies in the universe, would also reach a resolution capable of estimating the velocity dispersion and dynamic mass to light ratio for member galaxies. Additionally, kinematics of cluster members could reveal whether observed galaxies are travelling at speeds capable of experiencing ram pressure stripping, as opposed to the current naive case of direct radial infall into XLSSC 122 presented in my ram pressure stripping estimates. The galaxies have already been spectroscopically identified, such a study would be targeted and efficient. This type of study could identify which quenching mechanism lead to the creation of the quenched galaxy population in XLSSC 122.

4.3 Morphological Analysis

One key topic of further study in XLSSC 122 using the existing data set would be the investigation of galaxy-cluster and galaxy-galaxy interactions. These interactions have effect they have on the morphologies of interacting galaxies. It has been observed in XLSSC 122 that there is a high number of bulge dominated galaxies as compared to disk dominated galaxies in the core of XLSSC 122 (Leste et al., 2024). With the new smaller scale F814W images of the cluster, one could look for disturbed or compressed morphologies indicative of interactions within the cluster environment. One could also look to see what these red bulge dominated galaxies look like in the bluer filter. These morphological features could be compared to the star formation history and post-starburst features to see if the observed galaxies with post-starburst features appear to have condensed edges indicative of ram pressure stripping, or disturbed shapes indicative of galaxy interaction.

4.4 Incompleteness Estimate Improvements

The incompleteness, the chance that a given galaxy will be classified as a member galaxy of XLSSC 122, was estimated assuming a single stellar population of a red quiescent galaxy. This estimate is useful for identifying the proportion of galaxies missed in the areas outside the core of the cluster, where the identification of galaxies is more difficult due to lower exposure times. This incompleteness is important for measuring the density of cluster members in a given spatial region, or in the luminosity function. Both of these are valuable indications of infalling structure and galaxy evolution respectively. The spectroscopic incompleteness estimate could be improved by the inclusion of additional templates of star formation history. For example, adding galaxies with a blue, star forming template, or galaxies with a variety of dust obscuration would determine if there is a difference in spectroscopic completeness is different between red and blue galaxies. If the completeness for these two populations is different, the current estimate of density could be over or under-counting cluster members. My hypothesis is that the current spectroscopic completeness estimate is an overestimate, as the blue star forming galaxies are more distinct even at higher magnitudes due to their clear star forming emission lines. Another avenue of improvement would be taking into account the sky position of an object, some objects in more crowded regions could currently have an overestimated spectroscopic completeness. A crowded field increases the chances that an object will not be identified as a cluster member due to contamination. As is, the estimate used in this work is drawn from a very specific sample and broadly applied, and could be strengthened with a more thorough characterization.

4.5 Galaxy Quenching Model Expansion

In this work I created a toy ram pressure stripping model to explore whether an interaction with the ICM upon galaxy infall could rapidly quench the star formation in a galaxy. The model is relatively simple, containing a very approximate distribution of gas in the galaxy in a single exponential profile with a single scale radius. In reality, a galaxy's gaseous component is inhomogeneous and varies with the mass and morphology of the galaxy. The molecular gas in a galaxy has more mass per particle and is more concentrated than the atomic hydrogen component (Brown et al., 2017; Watts et al., 2023), and is more difficult to strip from a galaxy. Alternatively, the CGM contains energized atomic hydrogen, which requires less energy input to remove from a galaxy, but contains pockets of gas ranging several orders of magnitude in temperature space. I allow the mass of the stellar and DM halos to vary, in a manner consistent with $z = 2$ galaxies (van der Wel et al., 2014; Dutton and Macciò, 2014; Mo et al., 2010). The stripping condition presented and used to estimate the stripping radius is also simplified, assuming a single configuration of galaxy, that of a stellar disk. In reality the distribution of stars and gas in a galaxy can vary based on the morphology and evolutionary stage of a galaxy. The final tracer of quenching, the stripping radius, is also arbitrary, and is tenuously connected to the observed post-starburst features. The observed post-starburst features are weak, perhaps because the spectral binning is so broad. However, constructing a mock absorption feature strength from a simulated quenching galaxy would provide a more direct test of quenching efficacy.

I have not modelled other quenching mechanisms in this work. The location of these post-starburst galaxies near the virial radius of the cluster lead me to model ram pressure stripping with no consideration of intermediate quenching mechanisms such as starvation due to depletion of the circumgalactic medium. A more thorough comparison could take into account galaxy galaxy interactions, including the removal of the CGM through frequent near miss interactions, or the direct merging of galaxies. To go even farther, a comparison of the halo infall histories of similar galaxy clusters, as explored in Leste et al. (2024), could provide a more detailed context for which quenching mechanisms are possible.

4.6 What Have We Learned

I have created a revised, expanded, photometric catalogue of spectroscopically identified cluster members in XLSSC 122. The coincident red fraction plateau and PS fraction peak indicate a rapid quenching mechanism occurring in member galaxies near the virial radius of the cluster. I have shown that a ram pressure stripping could describe this rapid quenching, considering the density increase at the virial radius and the composition and infall velocities of cluster members. Given the regularity of the local density profile over radius, I do not detect a significant overdensity. Any infalling group or filament would have to be composed of low mass galaxies in greater quantities. These two observations, of an apparent lack of infalling structure and presence of environmental quenching, in addition to the similar luminosity functions between XLSSC 122 and lower redshift mature galaxy clusters, indicates that XLSSC 122 is a mature galaxy cluster with member galaxy evolution similar to local universe clusters.

Bibliography

M. G. Abadi, B. Moore, and R. G. Bower. Ram pressure stripping of spiral galaxies in clusters. *Monthly Notices of the Royal Astronomical Society*, 308:947–954, Oct. 1999. ISSN 0035-8711. doi: 10.1046/j.1365-8711.1999.02715.x.

G. O. Abell. The Distribution of Rich Clusters of Galaxies. *The Astrophysical Journal Supplement Series*, 3:211, May 1958. ISSN 0067-0049. doi: 10.1086/190036.

A. Abramson, J. Kenney, H. Crowl, and T. Tal. HST Imaging of Dust Structures and Stars in the Ram Pressure Stripped Virgo Spirals NGC 4402 and NGC 4522: Stripped from the Outside In with Dense Cloud Decoupling. *The Astronomical Journal*, 152:32, Aug. 2016. ISSN 0004-6256. doi: 10.3847/0004-6256/152/2/32.

Y. M. Bahé, I. G. McCarthy, M. L. Balogh, and A. S. Font. Why does the environmental influence on group and cluster galaxies extend beyond the virial radius? *Monthly Notices of the Royal Astronomical Society*, 430:3017–3031, Apr. 2013. ISSN 0035-8711. doi: 10.1093/mnras/stt109.

I. K. Baldry, M. L. Balogh, R. G. Bower, K. Glazebrook, R. C. Nichol, S. P. Bamford, and T. Budavari. Galaxy bimodality versus stellar mass and environment. *Monthly Notices of the Royal Astronomical Society*, 373:469–483, Dec. 2006. ISSN 0035-8711. doi: 10.1111/j.1365-2966.2006.11081.x.

M. L. Balogh, S. L. Morris, H. K. C. Yee, R. G. Carlberg, and E. Ellingson. Differential Galaxy Evolution in Cluster and Field Galaxies at z~0.3. *The Astrophysical Journal*, 527:54–79, Dec. 1999. ISSN 0004-637X. doi: 10.1086/308056.

M. L. Balogh, J. F. Navarro, and S. L. Morris. The Origin of Star Formation Gradients in Rich Galaxy Clusters. *The Astrophysical Journal*, 540:113–121, Sept. 2000. ISSN 0004-637X. doi: 10.1086/309323.

M. L. Balogh, I. K. Baldry, R. Nichol, C. Miller, R. Bower, and K. Glazebrook. The Bimodal Galaxy Color Distribution: Dependence on Luminosity and Environment. *The Astrophysical Journal*, 615:L101–L104, Nov. 2004. ISSN 0004-637X. doi: 10.1086/426079.

M. L. Balogh, S. L. McGee, A. Mok, A. Muzzin, R. F. J. van der Burg, R. G. Bower, A. Finoguenov, H. Hoekstra, C. Lidman, J. S. Mulchaey, A. Noble, L. C. Parker, M. Tanaka, D. J. Wilman, T. Webb, G. Wilson, and H. K. C. Yee. Evidence for a change in the dominant satellite galaxy quenching mechanism at z = 1. *Monthly Notices of the Royal Astronomical Society*, 456:4364–4376, Mar. 2016. ISSN 0035-8711. doi: 10.1093/mnras/stv2949.

M. L. Balogh, D. G. Gilbank, A. Muzzin, G. Rudnick, M. C. Cooper, C. Lidman, A. Biviano, R. Demarco, S. L. McGee, J. B. Nantais, A. Noble, L. Old, G. Wilson, H. K. C. Yee, C. Bellhouse, P. Cerulo, J. Chan, I. Pintos-Castro, R. Simpson, R. F. J. van der Burg, D. Zaritsky, F. Ziparo, M. V. Alonso, R. G. Bower, G. De Lucia, A. Finoguenov, D. G. Lambas, H. Muriel, L. C. Parker, A. Rettura, C. Valotto, and A. Wetzel. Gemini Observations of Galaxies in Rich Early Environments (GOGREEN) I: Survey description. *Monthly Notices of the Royal Astronomical Society*, 470:4168–4185, Oct. 2017. ISSN 0035-8711. doi: 10.1093/mnras/stx1370.

M. Bartelmann and P. Schneider. Weak gravitational lensing. *Physics Reports*, 340:291–472, Jan. 2001. ISSN 0370-1573. doi: 10.1016/S0370-1573(00)00082-X.

P. S. Behroozi, R. H. Wechsler, and C. Conroy. The Average Star Formation Histories of Galaxies in Dark Matter Halos from z=0-8. *The Astrophysical Journal*, 770(1):57, May 2013a. ISSN 0004-637X, 1538-4357. doi: 10.1088/0004-637X/770/1/57.

P. S. Behroozi, R. H. Wechsler, and C. Conroy. On the Lack of Evolution in Galaxy Star Formation Efficiency. *The Astrophysical Journal*, 762(2):L31, Jan. 2013b. ISSN 2041-8205, 2041-8213. doi: 10.1088/2041-8205/762/2/L31.

E. F. Bell, C. Wolf, K. Meisenheimer, H.-W. Rix, A. Borch, S. Dye, M. Kleinheinrich, L. Wisotzki, and D. H. McIntosh. Nearly 5000 Distant Early-Type Galaxies in COMBO-17: A Red Sequence and Its Evolution since z~1. *The Astrophysical Journal*, 608:752–767, June 2004. ISSN 0004-637X. doi: 10.1086/420778.

C. L. Bennett, D. Larson, J. L. Weiland, N. Jarosik, G. Hinshaw, N. Odegard, K. M. Smith, R. S. Hill, B. Gold, M. Halpern, E. Komatsu, M. R. Nolta, L. Page, D. N. Spergel,

E. Wollack, J. Dunkley, A. Kogut, M. Limon, S. S. Meyer, G. S. Tucker, and E. L. Wright. Nine-year Wilkinson Microwave Anisotropy Probe (WMAP) Observations: Final Maps and Results. *The Astrophysical Journal Supplement Series*, 208:20, Oct. 2013. ISSN 0067-0049. doi: 10.1088/0067-0049/208/2/20.

E. Bertin. SWarp: Resampling and Co-adding FITS Images Together. *Astrophysics Source Code Library*, page ascl:1010.068, Oct. 2010.

E. Bertin and S. Arnouts. SExtractor: Software for source extraction. *Astronomy and Astrophysics Supplement Series*, 117:393–404, June 1996. ISSN 0365-01380004-6361. doi: 10.1051/aas:1996164.

J. Binney and S. Tremaine. *Galactic Dynamics.* Princeton University Press, Jan. 1987.

G. R. Blumenthal, S. M. Faber, J. R. Primack, and M. J. Rees. Formation of galaxies and large-scale structure with cold dark matter. *Nature*, 311:517–525, Oct. 1984. ISSN 0028-0836. doi: 10.1038/311517a0.

G. R. Blumenthal, S. M. Faber, R. Flores, and J. R. Primack. Contraction of Dark Matter Galactic Halos Due to Baryonic Infall. *The Astrophysical Journal*, 301:27, Feb. 1986. ISSN 0004-637X. doi: 10.1086/163867.

V. A. Boehm, N. K. Lewis, C. E. Fairman, S. E. Moran, C. Gascón, H. R. Wakeford, M. K. Alam, L. Alderson, J. Barstow, N. E. Batalha, D. Grant, M. López-Morales, R. J. MacDonald, M. S. Marley, and K. Ohno. The HUSTLE Program: The UV to Near-Infrared HST WFC3/UVIS G280 Transmission Spectrum of WASP-127b, Oct. 2024.

J. R. Bond, L. Kofman, and D. Pogosyan. How filaments of galaxies are woven into the cosmic web. *Nature*, 380:603–606, Apr. 1996. ISSN 0028-0836. doi: 10.1038/380603a0.

A. Boselli, J. C. Cuillandre, M. Fossati, S. Boissier, D. Bomans, G. Consolandi, G. Anselmi, L. Cortese, P. Cote, P. Durrell, L. Ferrarese, M. Fumagalli, G. Gavazzi, S. Gwyn, G. Hensler, M. Sun, and E. Toloba. Spectacular tails of ionised gas in the Virgo cluster galaxy NGC 4569. *Astronomy & Astrophysics*, 587:A68, Mar. 2016. ISSN 0004-6361, 1432-0746. doi: 10.1051/0004-6361/201527795.

A. Boselli, B. Epinat, T. Contini, V. Abril-Melgarejo, L. A. Boogaard, E. Pointecouteau, E. Ventou, J. Brinchmann, D. Carton, H. Finley, L. Michel-Dansac, G. Soucail, and P. M. Weilbacher. Evidence for ram-pressure stripping in a cluster of galaxies at z

= 0.7. *Astronomy and Astrophysics*, 631:A114, Nov. 2019. ISSN 0004-6361. doi: 10.1051/0004-6361/201936133.

A. Boselli, M. Fossati, and M. Sun. Ram pressure stripping in high-density environments. *Astronomy and Astrophysics Review*, 30:3, Dec. 2022. ISSN 0935-4956. doi: 10.1007/s00159-022-00140-3.

G. Brammer. Grizli: Grism redshift and line analysis software. *Astrophysics Source Code Library*, page ascl:1905.001, May 2019.

G. B. Brammer, P. G. van Dokkum, and P. Coppi. EAZY: A Fast, Public Photometric Redshift Code. *The Astrophysical Journal*, 686:1503–1513, Oct. 2008. ISSN 0004-637X. doi: 10.1086/591786.

G. B. Brammer, P. G. van Dokkum, M. Franx, M. Fumagalli, S. Patel, H.-W. Rix, R. E. Skelton, M. Kriek, E. Nelson, K. B. Schmidt, R. Bezanson, E. da Cunha, D. K. Erb, X. Fan, N. Förster Schreiber, G. D. Illingworth, I. Labbé, J. Leja, B. Lundgren, D. Magee, D. Marchesini, P. McCarthy, I. Momcheva, A. Muzzin, R. Quadri, C. C. Steidel, T. Tal, D. Wake, K. E. Whitaker, and A. Williams. 3D-HST: A Wide-field Grism Spectroscopic Survey with the Hubble Space Telescope. *The Astrophysical Journal Supplement Series*, 200:13, June 2012. ISSN 0067-0049. doi: 10.1088/0067-0049/200/2/13.

T. Brown, B. Catinella, L. Cortese, C. d. P. Lagos, R. Davé, V. Kilborn, M. P. Haynes, R. Giovanelli, and M. Rafieferantsoa. Cold gas stripping in satellite galaxies: From pairs to clusters. *Monthly Notices of the Royal Astronomical Society*, 466:1275–1289, Apr. 2017. ISSN 0035-8711. doi: 10.1093/mnras/stw2991.

T. Brown, I. D. Roberts, M. Thorp, S. L. Ellison, N. Zabel, C. D. Wilson, Y. M. Bahé, D. Bisaria, A. D. Bolatto, A. Boselli, A. Chung, L. Cortese, B. Catinella, T. A. Davis, M. J. Jiménez-Donaire, C. D. P. Lagos, B. Lee, L. C. Parker, R. Smith, K. Spekkens, A. R. H. Stevens, V. Villanueva, and A. B. Watts. VERTICO. VII. Environmental Quenching Caused by the Suppression of Molecular Gas Content and Star Formation Efficiency in Virgo Cluster Galaxies. *The Astrophysical Journal*, 956:37, Oct. 2023. ISSN 0004-637X. doi: 10.3847/1538-4357/acf195.

G. L. Bryan and M. L. Norman. Statistical Properties of X-Ray Clusters: Analytic and Numerical Comparisons. *The Astrophysical Journal*, 495(1):80, Mar. 1998. ISSN 0004-637X. doi: 10.1086/305262.

H. Butcher and A. Oemler, Jr. The evolution of galaxies in clusters. V. A study of populations since Z 0.5. *The Astrophysical Journal*, 285:426–438, Oct. 1984. ISSN 0004-637X. doi: 10.1086/162519.

A. Cavaliere and R. Fusco-Femiano. X-rays from hot plasma in clusters of galaxies. *Astronomy and Astrophysics*, 49:137–144, May 1976. ISSN 0004-6361.

J. C. C. Chan, G. Wilson, G. Rudnick, A. Muzzin, M. Balogh, J. Nantais, R. F. J. van der Burg, P. Cerulo, A. Biviano, M. C. Cooper, R. Demarco, B. Forrest, C. Lidman, A. Noble, L. Old, I. Pintos-Castro, A. M. M. Reeves, K. A. Webb, H. K. C. Yee, M. H. Abdullah, G. D. Lucia, D. Marchesini, S. L. McGee, M. Stefanon, and D. Zaritsky. The Rest-frame \$H\$-band Luminosity Function of Red Sequence Galaxies in Clusters at \$1.0 < z < 1.3\$. *The Astrophysical Journal*, 880(2):119, Aug. 2019. ISSN 1538-4357. doi: 10.3847/1538-4357/ab2b3a.

Y.-K. Chiang, R. Overzier, and K. Gebhardt. Ancient Light from Young Cosmic Cities: Physical and Observational Signatures of Galaxy Proto-Clusters, Dec. 2013.

C. Circosta, V. Mainieri, P. Padovani, G. Lanzuisi, M. Salvato, C. M. Harrison, D. Kakkad, A. Puglisi, G. Vietri, G. Zamorani, C. Cicone, B. Husemann, C. Vignali, B. Balmaverde, M. Bischetti, A. Bongiorno, M. Brusa, S. Carniani, F. Civano, A. Comastri, G. Cresci, C. Feruglio, F. Fiore, S. Fotopoulou, A. Karim, A. Lamastra, B. Magnelli, F. Mannucci, A. Marconi, A. Merloni, H. Netzer, M. Perna, E. Piconcelli, G. Rodighiero, E. Schinnerer, M. Schramm, A. Schulze, J. Silverman, and L. Zappacosta. SUPER. I. Toward an unbiased study of ionized outflows in z $\sim$ 2 active galactic nuclei: Survey overview and sample characterization. *Astronomy and Astrophysics*, 620:A82, Nov. 2018. ISSN 0004-6361. doi: 10.1051/0004-6361/201833520.

C. Conroy and J. E. Gunn. The Propagation of Uncertainties in Stellar Population Synthesis Modeling. III. Model Calibration, Comparison, and Evaluation. *The Astrophysical Journal*, 712:833–857, Apr. 2010. ISSN 0004-637X. doi: 10.1088/0004-637X/712/2/833.

C. Conroy, J. E. Gunn, and M. White. The Propagation of Uncertainties in Stellar Population Synthesis Modeling. I. The Relevance of Uncertain Aspects of Stellar Evolution and the Initial Mass Function to the Derived Physical Properties of Galaxies. *The Astrophysical Journal*, 699:486–506, July 2009. ISSN 0004-637X. doi: 10.1088/0004-637X/699/1/486.

H. H. Crowl and J. D. P. Kenney. The Stellar Populations of Stripped Spiral Galaxies in the Virgo Cluster. *The Astronomical Journal*, 136:1623–1644, Oct. 2008. ISSN 0004-6256. doi: 10.1088/0004-6256/136/4/1623.

B. Darvish, B. Mobasher, D. Sobral, A. Rettura, N. Scoville, A. Faisst, and P. Capak. THE EFFECTS OF THE LOCAL ENVIRONMENT AND StelLAR MASS ON GALAXY QUENCHING TO z $\sim$ 3. *The Astrophysical Journal*, 825(2):113, July 2016. ISSN 0004-637X. doi: 10.3847/0004-637X/825/2/113.

L. Dressel. WFC3 Instrument Handbook for Cycle 29 v. 13. In *WFC3 Instrument Handbook for Cycle 29 v. 13*, volume 13, page 13. Jan. 2021.

A. Dressler. Galaxy morphology in rich clusters: Implications for the formation and evolution of galaxies. *The Astrophysical Journal*, 236:351–365, Mar. 1980. ISSN 0004-637X. doi: 10.1086/157753.

A. Dressler, I. Smail, B. Poggianti, H. Butcher, W. Couch, R. Ellis, and A. O. Jr. A Spectroscopic Catalog of 10 Distant Rich Clusters of Galaxies, Jan. 1999.

A. Dressler, A. Oemler, Jr., B. M. Poggianti, M. D. Gladders, L. Abramson, and B. Vulcani. The IMACS Cluster Building Survey. II. Spectral Evolution of Galaxies in the Epoch of Cluster Assembly. *The Astrophysical Journal*, 770:62, June 2013. ISSN 0004-637X. doi: 10.1088/0004-637X/770/1/62.

A. A. Dutton and A. V. Macciò. Cold dark matter haloes in the Planck era: Evolution of structural parameters for Einasto and NFW profiles. *Monthly Notices of the Royal Astronomical Society*, 441:3359–3374, July 2014. ISSN 0035-8711. doi: 10.1093/mnras/stu742.

V. R. Eke, S. Cole, and C. S. Frenk. Cluster evolution as a diagnostic for Omega. *Monthly Notices of the Royal Astronomical Society*, 282:263–280, Sept. 1996. ISSN 0035-8711. doi: 10.1093/mnras/282.1.263.

L. Ferrarese, P. Côté, R. Sánchez-Janssen, J. Roediger, A. W. McConnachie, P. R. Durrell, L. A. MacArthur, J. P. Blakeslee, P.-A. Duc, S. Boissier, A. Boselli, S. Courteau, J.-C. Cuillandre, E. Emsellem, S. D. J. Gwyn, P. Guhathakurta, A. Jordán, A. Lançon, C. Liu, S. Mei, J. C. Mihos, J. F. Navarro, E. W. Peng, T. H. Puzia, J. E. Taylor, E. Toloba, and H. Zhang. The Next Generation Virgo Cluster Survey (NGVS). XIII. The Luminosity and Mass Function of Galaxies in the Core of the Virgo Cluster and the Contribution from

Disrupted Satellites. *The Astrophysical Journal*, 824:10, June 2016. ISSN 0004-637X. doi: 10.3847/0004-637X/824/1/10.

D. Foreman-Mackey, D. W. Hogg, D. Lang, and J. Goodman. Emcee: The MCMC Hammer. *Publications of the Astronomical Society of the Pacific*, 125:306, Mar. 2013. ISSN 0004-6280. doi: 10.1086/670067.

K. C. Freeman. On the Disks of Spiral and S0 Galaxies. *The Astrophysical Journal*, 160: 811, June 1970. ISSN 0004-637X. doi: 10.1086/150474.

Y. Fujita. Pre-Processing of Galaxies before Entering a Cluster. *Publications of the Astronomical Society of Japan*, 56:29–43, Feb. 2004. ISSN 0004-6264. doi: 10.1093/pasj/56.1.29.

M. D. Gladders and H. K. C. Yee. A New Method For Galaxy Cluster Detection. I. The Algorithm. *The Astronomical Journal*, 120:2148–2162, Oct. 2000. ISSN 0004-6256. doi: 10.1086/301557.

M. D. Gladders and H. K. C. Yee. The Red-Sequence Cluster Survey. I. The Survey and Cluster Catalogs for Patches RCS 0926+37 and RCS 1327+29. *The Astrophysical Journal Supplement Series*, 157(1):1, Mar. 2005. ISSN 0067-0049. doi: 10.1086/427327.

R. Gobat, P. Rosati, V. Strazzullo, A. Rettura, R. Demarco, and M. Nonino. Star formation histories of early-type galaxies at z = 1.2 in cluster and field environments. *Astronomy and Astrophysics*, 488:853–860, Sept. 2008. ISSN 0004-6361. doi: 10.1051/0004-6361:200809531.

R. Gobat, E. Daddi, M. Onodera, A. Finoguenov, A. Renzini, N. Arimoto, R. Bouwens, M. Brusa, R.-R. Chary, A. Cimatti, M. Dickinson, X. Kong, and M. Mignoli. A mature cluster with X-ray emission at z = 2.07. *Astronomy & Astrophysics*, 526:A133, Feb. 2011. ISSN 0004-6361, 1432-0746. doi: 10.1051/0004-6361/201016084.

S. Gonzaga, W. Hack, A. Fruchter, and J. Mack. *The DrizzlePac Handbook*. June 2012.

T. Goto, M. Postman, N. J. G. Cross, G. D. Illingworth, K. Tran, D. Magee, M. Franx, N. Benitez, R. J. Bouwens, R. Demarco, H. C. Ford, N. L. Homeier, A. R. Martel, F. Menanteau, M. Clampin, G. F. Hartig, D. R. Ardila, F. Bartko, J. P. Blakeslee, L. D. Bradley, T. J. Broadhurst, R. A. Brown, C. J. Burrows, E. S. Cheng, P. D. Feldman, D. A. Golimowski, C. Gronwall, B. Holden, L. Infante, M. J. Jee, J. E. Krist, M. P. Lesser, S. Mei, G. R. Meurer, G. K. Miley, V. Motta, R. Overzier, M. Sirianni, W. B.

Sparks, H. D. Tran, Z. I. Tsvetanov, R. L. White, W. Zheng, and A. Zirm. The Luminosity Functions of the Galaxy Cluster MS1054-0321 at z=0.83 based on ACS Photometry. *The Astrophysical Journal*, 621(1):188–200, Mar. 2005. ISSN 0004-637X, 1538-4357. doi: 10.1086/427492.

A. W. Graham and S. P. Driver. A Concise Reference to (Projected) Sérsic R1/n Quantities, Including Concentration, Profile Slopes, Petrosian Indices, and Kron Magnitudes. *Publications of the Astronomical Society of Australia*, 22:118–127, Jan. 2005. ISSN 1323-3580. doi: 10.1071/AS05001.

J. E. Gunn and J. R. Gott, III. On the Infall of Matter Into Clusters of Galaxies and Some Effects on Their Evolution. *The Astrophysical Journal*, 176:1, Aug. 1972. ISSN 0004-637X. doi: 10.1086/151605.

H. Gursky, E. Kellogg, S. Murray, C. Leong, H. Tananbaum, and R. Giacconi. A Strong X-Ray Source in the Coma Cluster Observed by UHURU. *The Astrophysical Journal*, 167: L81, Aug. 1971. ISSN 0004-637X. doi: 10.1086/180765.

S. Hansen, E. Sheldon, R. Wechsler, and B. Koester. The Galaxy Content of SDSS Clusters and Groups. *The Astrophysical Journal*, 699, Oct. 2007. doi: 10.1088/0004-637X/699/2/1333.

W. K. Hastings. Monte Carlo Sampling Methods using Markov Chains and their Applications. *Biometrika*, 57:97–109, Apr. 1970. doi: 10.1093/biomet/57.1.97.

W. Herschel. Catalogue of One Thousand New Nebulae and Clusters of Stars. By William Herschel, LL.D. F. R. S. *Philosophical Transactions of the Royal Society of London Series I*, 76:457–499, Jan. 1786.

H. Hoekstra. How well can we determine cluster mass profiles from weak lensing? *Monthly Notices of the Royal Astronomical Society*, 339:1155–1162, Mar. 2003. ISSN 0035-8711. doi: 10.1046/j.1365-8711.2003.06264.x.

D. W. Hogg, M. R. Blanton, D. J. Eisenstein, J. E. Gunn, D. J. Schlegel, I. Zehavi, N. A. Bahcall, J. Brinkmann, I. Csabai, D. P. Schneider, D. H. Weinberg, and D. G. York. The Overdensities of Galaxy Environments as a Function of Luminosity and Color. *The Astrophysical Journal*, 585(1):L5, Jan. 2003. ISSN 0004-637X. doi: 10.1086/374238.

K. Horne. An optimal extraction algorithm for CCD spectroscopy. *Publications of the Astronomical Society of the Pacific*, 98:609–617, June 1986. ISSN 0004-6280. doi: 10.1086/131801.

A. Hou, L. C. Parker, M. L. Balogh, S. L. McGee, D. J. Wilman, J. L. Connelly, W. E. Harris, A. Mok, J. S. Mulchaey, R. G. Bower, and A. Finoguenov. Do group dynamics play a role in the evolution of member galaxies? *Monthly Notices of the Royal Astronomical Society*, 435:1715–1726, Oct. 2013. ISSN 0035-8711. doi: 10.1093/mnras/stt1410.

E. P. Hubble. Extragalactic nebulae. *The Astrophysical Journal*, 64:321–369, Dec. 1926. ISSN 0004-637X. doi: 10.1086/143018.

Y. L. Jaffé, B. M. Poggianti, A. Moretti, M. Gullieuszik, R. Smith, B. Vulcani, G. Fasano, J. Fritz, S. Tonnesen, D. Bettoni, G. Hau, A. Biviano, C. Bellhouse, and S. McGee. GASP. IX. Jellyfish galaxies in phase-space: An orbital study of intense ram-pressure stripping in clusters. *Monthly Notices of the Royal Astronomical Society*, 476:4753–4764, June 2018. ISSN 0035-8711. doi: 10.1093/mnras/sty500.

L. Kawinwanichakij, C. Papovich, R. F. Quadri, K. Glazebrook, G. G. Kacprzak, R. J. Allen, E. F. Bell, D. J. Croton, A. Dekel, H. C. Ferguson, B. Forrest, N. A. Grogin, Y. Guo, D. D. Kocevski, A. M. Koekemoer, I. Labbé, R. A. Lucas, T. Nanayakkara, L. R. Spitler, C. M. S. Straatman, K.-V. H. Tran, A. Tomczak, and P. van Dokkum. Effect of Local Environment and Stellar Mass on Galaxy Quenching and Morphology at $0.5 < z < 2.0$. *The Astrophysical Journal*, 847:134, Oct. 2017. ISSN 0004-637X. doi: 10.3847/1538-4357/aa8b75.

I. King. The structure of star clusters. I. an empirical density law. *The Astronomical Journal*, 67:471, Oct. 1962. ISSN 0004-6256. doi: 10.1086/108756.

A. M. Koekemoer, S. M. Faber, H. C. Ferguson, N. A. Grogin, D. D. Kocevski, D. C. Koo, K. Lai, J. M. Lotz, R. A. Lucas, E. J. McGrath, S. Ogaz, A. Rajan, A. G. Riess, S. A. Rodney, L. Strolger, S. Casertano, M. Castellano, T. Dahlen, M. Dickinson, T. Dolch, A. Fontana, M. Giavalisco, A. Grazian, Y. Guo, N. P. Hathi, K.-H. Huang, A. van der Wel, H.-J. Yan, V. Acquaviva, D. M. Alexander, O. Almaini, M. L. N. Ashby, M. Barden, E. F. Bell, F. Bournaud, T. M. Brown, K. I. Caputi, P. Cassata, P. J. Challis, R.-R. Chary, E. Cheung, M. Cirasuolo, C. J. Conselice, A. Roshan Cooray, D. J. Croton, E. Daddi, R. Davé, D. F. de Mello, L. de Ravel, A. Dekel, J. L. Donley, J. S. Dunlop, A. A. Dutton, D. Elbaz, G. G. Fazio, A. V. Filippenko, S. L. Finkelstein, C. Frazer, J. P. Gardner,

P. M. Garnavich, E. Gawiser, R. Gruetzbauch, W. G. Hartley, B. Häussler, J. Herrington, P. F. Hopkins, J.-S. Huang, S. W. Jha, A. Johnson, J. S. Kartaltepe, A. A. Khostovan, R. P. Kirshner, C. Lani, K.-S. Lee, W. Li, P. Madau, P. J. McCarthy, D. H. McIntosh, R. J. McLure, C. McPartland, B. Mobasher, H. Moreira, A. Mortlock, L. A. Moustakas, M. Mozena, K. Nandra, J. A. Newman, J. L. Nielsen, S. Niemi, K. G. Noeske, C. J. Papovich, L. Pentericci, A. Pope, J. R. Primack, S. Ravindranath, N. A. Reddy, A. Renzini, H.-W. Rix, A. R. Robaina, D. J. Rosario, P. Rosati, S. Salimbeni, C. Scarlata, B. Siana, L. Simard, J. Smidt, D. Snyder, R. S. Somerville, H. Spinrad, A. N. Straughn, O. Telford, H. I. Teplitz, J. R. Trump, C. Vargas, C. Villforth, C. R. Wagner, P. Wandro, R. H. Wechsler, B. J. Weiner, T. Wiklind, V. Wild, G. Wilson, S. Wuyts, and M. S. Yun. CANDELS: The Cosmic Assembly Near-infrared Deep Extragalactic Legacy Survey—The Hubble Space Telescope Observations, Imaging Data Products, and Mosaics. *The Astrophysical Journal Supplement Series*, 197:36, Dec. 2011. ISSN 0067-0049. doi: 10.1088/0067-0049/197/2/36.

K. Kraljic, S. Arnouts, C. Pichon, C. Laigle, S. de la Torre, D. Vibert, C. Cadiou, Y. Dubois, M. Treyer, C. Schimd, S. Codis, V. de Lapparent, J. Devriendt, H. S. Hwang, D. Le Borgne, N. Malavasi, B. Milliard, M. Musso, D. Pogosyan, M. Alpaslan, J. Bland-Hawthorn, and A. H. Wright. Galaxy evolution in the metric of the cosmic web. *Monthly Notices of the Royal Astronomical Society*, 474:547–571, Feb. 2018. ISSN 0035-8711. doi: 10.1093/mnras/stx2638.

S. Lavoie, J. P. Willis, J. Démoclès, D. Eckert, F. Gastaldello, G. P. Smith, C. Lidman, C. Adami, F. Pacaud, M. Pierre, N. Clerc, P. Giles, M. Lieu, L. Chiappetti, B. Altieri, F. Ardila, I. Baldry, A. Bongiorno, S. Desai, A. Elyiv, L. Faccioli, B. Gardner, B. Garilli, M. W. Groote, L. Guennou, L. Guzzo, A. M. Hopkins, J. Liske, S. McGee, O. Melnyk, M. S. Owers, B. Poggianti, T. J. Ponman, M. Scodeggio, L. Spitler, and R. J. Tuffs. The XXL survey XV: Evidence for dry merger driven BCG growth in XXL-100-GC X-ray clusters. *Monthly Notices of the Royal Astronomical Society*, 462(4):4141–4156, Nov. 2016. ISSN 0035-8711. doi: 10.1093/mnras/stw1906.

B. C. Lemaux, A. R. Tomczak, L. M. Lubin, R. R. Gal, L. Shen, D. Pelliccia, P. F. Wu, D. Hung, S. Mei, O. Le Fèvre, N. Rumbaugh, D. D. Kocevski, and G. K. Squires. Persistence of the colour-density relation and efficient environmental quenching to z $\sim$ 1.4. *Monthly Notices of the Royal Astronomical Society*, 490:1231–1254, Nov. 2019. ISSN 0035-8711. doi: 10.1093/mnras/stz2661.

O. K. Leste, J. P. Willis, R. E. A. Canning, and D. Rennehan. A morphological analysis of the galaxy cluster XLSSC 122 at z = 1.98. *Monthly Notices of the Royal Astronomical Society*, 533:2927–2947, Sept. 2024. ISSN 0035-8711. doi: 10.1093/mnras/stae1967.

I. H. Li, H. K. C. Yee, B. C. Hsieh, and M. Gladders. EVOLUTION OF GROUP GALAXIES FROM THE FIRST RED-SEQUENCE CLUSTER SURVEY. *The Astrophysical Journal*, 749(2):150, Apr. 2012. ISSN 0004-637X, 1538-4357. doi: 10.1088/0004-637X/749/2/150.

N. I. Libeskind, R. van de Weygaert, M. Cautun, B. Falck, E. Tempel, T. Abel, M. Alpaslan, M. A. Aragón-Calvo, J. E. Forero-Romero, R. Gonzalez, S. Gottlöber, O. Hahn, W. A. Hellwing, Y. Hoffman, B. J. T. Jones, F. Kitaura, A. Knebe, S. Manti, M. Neyrinck, S. E. Nuza, N. Padilla, E. Platen, N. Ramachandra, A. Robotham, E. Saar, S. Shandarin, M. Steinmetz, R. S. Stoica, T. Sousbie, and G. Yepes. Tracing the cosmic web. *Monthly Notices of the Royal Astronomical Society*, 473:1195–1217, Jan. 2018. ISSN 0035-8711. doi: 10.1093/mnras/stx1976.

R. A. Lucas and J. E. Ryon. ACS Data Handbook v. 11.0. In *ACS Data Handbook v. 11.0*, volume 11, page 11. Feb. 2022.

P. Madau and M. Dickinson. Cosmic Star-Formation History. *Annual Review of Astronomy and Astrophysics*, 52(1):415–486, Aug. 2014. ISSN 0066-4146, 1545-4282. doi: 10.1146/annurev-astro-081811-125615.

A. B. Mantz, Z. Abdulla, J. E. Carlstrom, C. H. Greer, E. M. Leitch, D. P. Marrone, S. Muchovej, C. Adami, M. Birkinshaw, M. Bremer, N. Clerc, P. Giles, C. Horellou, B. Maughan, F. Pacaud, M. Pierre, and J. Willis. The XXL Survey V: Detection of the Sunyaev-Zel'dovich effect of the Redshift 1.9 Galaxy Cluster XLSSU J021744.1-034536 with CARMA. *The Astrophysical Journal*, 794(2):157, Oct. 2014. ISSN 1538-4357. doi: 10.1088/0004-637X/794/2/157.

A. B. Mantz, Z. Abdulla, S. W. Allen, J. E. Carlstrom, C. H. A. Logan, D. P. Marrone, B. J. Maughan, J. Willis, F. Pacaud, and M. Pierre. The XXL Survey: XVII. X-ray and Sunyaev-Zel'dovich Properties of the Redshift 2.0 Galaxy Cluster XLSSC 122. *Astronomy & Astrophysics*, 620:A2, Dec. 2018. ISSN 0004-6361, 1432-0746. doi: 10.1051/0004-6361/201630096.

H. J. Martínez, H. Muriel, and V. Coenda. Galaxies infalling into groups: Filaments versus isotropic infall. *Monthly Notices of the Royal Astronomical Society*, 455(1):127–135, Jan. 2016. ISSN 0035-8711. doi: 10.1093/mnras/stv2295.

I. G. McCarthy, C. S. Frenk, A. S. Font, C. G. Lacey, R. G. Bower, N. L. Mitchell, M. L. Balogh, and T. Theuns. Ram pressure stripping the hot gaseous haloes of galaxies in groups and clusters. *Monthly Notices of the Royal Astronomical Society*, 383:593–605, Jan. 2008. ISSN 0035-8711. doi: 10.1111/j.1365-2966.2007.12577.x.

M. McDonald, S. Courteau, and R. B. Tully. The near-IR luminosity function and bimodal surface brightness distributions of Virgo cluster galaxies. *Monthly Notices of the Royal Astronomical Society*, 394:2022–2042, Apr. 2009. ISSN 0035-8711. doi: 10.1111/j.1365-2966.2009.14442.x.

S. L. McGee, M. L. Balogh, R. G. Bower, A. S. Font, and I. G. McCarthy. The accretion of galaxies into groups and clusters. *Monthly Notices of the Royal Astronomical Society*, 400 (2):937–950, 2009. ISSN 1365-2966. doi: 10.1111/j.1365-2966.2009.15507.x.

S. L. McGee, R. G. Bower, and M. L. Balogh. Overconsumption, outflows and the quenching of satellite galaxies. *Monthly Notices of the Royal Astronomical Society*, 442:L105–L109, July 2014. ISSN 0035-8711. doi: 10.1093/mnrasl/slu066.

K. McNab, M. L. Balogh, R. F. J. van der Burg, A. Forestell, K. Webb, B. Vulcani, G. Rudnick, A. Muzzin, M. C. Cooper, S. McGee, A. Biviano, P. Cerulo, J. C. C. Chan, G. De Lucia, R. Demarco, A. Finoguenov, B. Forrest, C. Golledge, P. Jablonka, C. Lidman, J. Nantais, L. Old, I. Pintos-Castro, B. Poggianti, A. M. M. Reeves, G. Wilson, H. K. C. Yee, and D. Zaritsky. The GOGREEN survey: Transition galaxies and the evolution of environmental quenching. *Monthly Notices of the Royal Astronomical Society*, 508:157–174, Nov. 2021. ISSN 0035-8711. doi: 10.1093/mnras/stab2558.

C. McPartland, H. Ebeling, E. Roediger, and K. Blumenthal. Jellyfish: The origin and distribution of extreme ram-pressure stripping events in massive galaxy clusters. *Monthly Notices of the Royal Astronomical Society*, 455:2994–3008, Jan. 2016. ISSN 0035-8711. doi: 10.1093/mnras/stv2508.

C. Messier. Catalogue des Nébuleuses et des Amas d'Étoiles (Catalog of Nebulae and Star Clusters). Technical report, Jan. 1781.

N. Metropolis, A. W. Rosenbluth, M. N. Rosenbluth, A. H. Teller, and E. Teller. Equation of State Calculations by Fast Computing Machines. *Journal of Chemical Physics*, 21: 1087–1092, June 1953. ISSN 0021-9606. doi: 10.1063/1.1699114.

H. Mo, F. C. van den Bosch, and S. White. *Galaxy Formation and Evolution.* May 2010. doi: 10.1017/CBO9780511807244.

I. G. Momcheva, G. B. Brammer, P. G. van Dokkum, R. E. Skelton, K. E. Whitaker, E. J. Nelson, M. Fumagalli, M. V. Maseda, J. Leja, M. Franx, H.-W. Rix, R. Bezanson, E. Da Cunha, C. Dickey, N. M. Förster Schreiber, G. Illingworth, M. Kriek, I. Labbé, J. Ulf Lange, B. F. Lundgren, D. Magee, D. Marchesini, P. Oesch, C. Pacifici, S. G. Patel, S. Price, T. Tal, D. A. Wake, A. van der Wel, and S. Wuyts. The 3D-HST Survey: Hubble Space Telescope WFC3/G141 Grism Spectra, Redshifts, and Emission Line Measurements for ∼ 100,000 Galaxies. *The Astrophysical Journal Supplement Series*, 225:27, Aug. 2016. ISSN 0067-0049. doi: 10.3847/0067-0049/225/2/27.

B. Moore, N. Katz, G. Lake, A. Dressler, and A. Oemler. Galaxy harassment and the evolution of clusters of galaxies. *Nature*, 379:613–616, Feb. 1996. ISSN 0028-0836. doi: 10.1038/379613a0.

A. Moretti, M. Radovich, B. M. Poggianti, B. Vulcani, M. Gullieuszik, A. Werle, C. Bellhouse, C. Bacchini, J. Fritz, G. Soucail, J. Richard, A. Franchetto, N. Tomičić, and A. Omizzolo. Observing Ram Pressure at Work in Intermediate Redshift Clusters with MUSE: The Case of Abell 2744 and Abell 370. *The Astrophysical Journal*, 925:4, Jan. 2022. ISSN 0004-637X. doi: 10.3847/1538-4357/ac36c7.

S. I. Muldrew, N. A. Hatch, and E. A. Cooke. What are protoclusters? - Defining high-redshift galaxy clusters and protoclusters. *Monthly Notices of the Royal Astronomical Society*, 452:2528–2539, Sept. 2015. ISSN 0035-8711. doi: 10.1093/mnras/stv1449.

A. Muzzin, D. Marchesini, M. Stefanon, M. Franx, H. J. McCracken, B. Milvang-Jensen, J. S. Dunlop, J. P. U. Fynbo, G. Brammer, I. Labbé, and P. G. van Dokkum. The Evolution of the Stellar Mass Functions of Star-forming and Quiescent Galaxies to z = 4 from the COSMOS/UltraVISTA Survey. *The Astrophysical Journal*, 777:18, Nov. 2013. ISSN 0004-637X. doi: 10.1088/0004-637X/777/1/18.

J. B. Nantais, A. Muzzin, R. F. J. van der Burg, G. Wilson, C. Lidman, R. Foltz, A. DeGroot, A. Noble, M. C. Cooper, and R. Demarco. Evidence for strong evolution in galaxy environmental quenching efficiency between z = 1.6 and z = 0.9. *Monthly Notices of the Royal Astronomical Society: Letters*, 465(1):L104–L108, Feb. 2017. ISSN 1745-3925. doi: 10.1093/mnrasl/slw224.

J. F. Navarro, C. S. Frenk, and S. D. M. White. The assembly of galaxies in a hierarchically clustering universe. *Monthly Notices of the Royal Astronomical Society*, 275:56–66, July 1995. ISSN 0035-8711. doi: 10.1093/mnras/275.1.56.

J. F. Navarro, C. S. Frenk, and S. D. M. White. A Universal Density Profile from Hierarchical Clustering. *The Astrophysical Journal*, 490:493–508, Dec. 1997. ISSN 0004-637X. doi: 10.1086/304888.

A. B. Newman, R. S. Ellis, S. Andreon, T. Treu, A. Raichoor, and G. Trinchieri. SPECTROSCOPIC CONFIRMATION OF THE RICH z = 1.80 GALAXY CLUSTER JKCS 041 USING THE WFC3 GRISM: ENVIRONMENTAL TRENDS IN THE AGES AND STRUCTURE OF QUIESCENT GALAXIES. *The Astrophysical Journal*, 788(1):51, May 2014. ISSN 0004-637X. doi: 10.1088/0004-637X/788/1/51.

E. Noordeh, R. E. A. Canning, J. P. Willis, S. W. Allen, A. Mantz, S. A. Stanford, and G. Brammer. Quiescent galaxies in a virialized cluster at redshift 2: Evidence for accelerated size-growth. *Monthly Notices of the Royal Astronomical Society*, 507(4):5272–5280, Sept. 2021. ISSN 0035-8711, 1365-2966. doi: 10.1093/mnras/stab2459.

N. Okabe, M. Oguri, H. Akamatsu, A. Hamabata, A. J. Nishizawa, E. Medezinski, Y. Koyama, M. Hayashi, T. Okabe, S. Ueda, I. Mitsuishi, and N. Ota. Halo concentration, galaxy red fraction, and gas properties of optically defined merging clusters†. *Publications of the Astronomical Society of Japan*, 71(4):79, Aug. 2019. ISSN 0004-6264. doi: 10.1093/pasj/psz059.

A. Paccagnella, B. Vulcani, B. M. Poggianti, J. Fritz, G. Fasano, A. Moretti, Y. L. Jaffé, A. Biviano, M. Gullieuszik, D. Bettoni, A. Cava, W. Couch, and M. D'Onofrio. OmegaWINGS: The First Complete Census of Post-starburst Galaxies in Clusters in the Local Universe. *The Astrophysical Journal*, 838(2):148, Apr. 2017. ISSN 0004-637X, 1538-4357. doi: 10.3847/1538-4357/aa64d7.

S. Parsa, J. S. Dunlop, R. J. McLure, and A. Mortlock. The galaxy UV luminosity function at z $\simeq$ 2-4; new results on faint-end slope and the evolution of luminosity density. *Monthly Notices of the Royal Astronomical Society*, 456:3194–3211, Mar. 2016. ISSN 0035-8711. doi: 10.1093/mnras/stv2857.

P. J. E. Peebles. *The Large-Scale Structure of the Universe*. Jan. 1980.

Y.-j. Peng, S. J. Lilly, K. Kovač, M. Bolzonella, L. Pozzetti, A. Renzini, G. Zamorani, O. Ilbert, C. Knobel, A. Iovino, C. Maier, O. Cucciati, L. Tasca, C. M. Carollo, J. Silverman, P. Kampczyk, L. de Ravel, D. Sanders, N. Scoville, T. Contini, V. Mainieri, M. Scodeggio, J.-P. Kneib, O. Le Fèvre, S. Bardelli, A. Bongiorno, K. Caputi, G. Coppa, S. de la Torre, P. Franzetti, B. Garilli, F. Lamareille, J.-F. Le Borgne, V. Le Brun, M. Mignoli, E. Perez Montero, R. Pello, E. Ricciardelli, M. Tanaka, L. Tresse, D. Vergani, N. Welikala, E. Zucca, P. Oesch, U. Abbas, L. Barnes, R. Bordoloi, D. Bottini, A. Cappi, P. Cassata, A. Cimatti, M. Fumana, G. Hasinger, A. Koekemoer, A. Leauthaud, D. Maccagni, C. Marinoni, H. McCracken, P. Memeo, B. Meneux, P. Nair, C. Porciani, V. Presotto, and R. Scaramella. Mass and Environment as Drivers of Galaxy Evolution in SDSS and zCOSMOS and the Origin of the Schechter Function. *The Astrophysical Journal*, 721: 193–221, Sept. 2010. ISSN 0004-637X. doi: 10.1088/0004-637X/721/1/193.

Y.-j. Peng, S. J. Lilly, A. Renzini, and M. Carollo. MASS AND ENVIRONMENT AS DRIVERS OF GALAXY EVOLUTION. II. THE QUENCHING OF SAtelLITE GALAXIES AS THE ORIGIN OF ENVIRONMENTAL EFFECTS. *The Astrophysical Journal*, 757(1):4, Aug. 2012. ISSN 0004-637X. doi: 10.1088/0004-637X/757/1/4.

A. A. Penzias and R. W. Wilson. A Measurement of Excess Antenna Temperature at 4080 Mc/s. *The Astrophysical Journal*, 142:419–421, July 1965. ISSN 0004-637X. doi: 10.1086/148307.

B. Poggianti, I. Smail, A. Dressler, W. Couch, A. Barger, H. Butcher, R. Ellis, and A. O. Jr. The Star Formation Histories of Galaxies in Distant Clusters, Jan. 1999.

B. M. Poggianti, A. Aragón-Salamanca, D. Zaritsky, G. De Lucia, B. Milvang-Jensen, V. Desai, P. Jablonka, C. Halliday, G. Rudnick, J. Varela, S. Bamford, P. Best, D. Clowe, S. Noll, R. Saglia, R. Pelló, L. Simard, A. von der Linden, and S. White. THE ENVIRONMENTS OF STARBURST AND POST-STARBURST GALAXIES AT z = 0.4–0.8 *. *The Astrophysical Journal*, 693(1):112, Feb. 2009. ISSN 0004-637X. doi: 10.1088/0004-637X/693/1/112.

B. M. Poggianti, A. Moretti, M. Gullieuszik, J. Fritz, Y. Jaffé, D. Bettoni, G. Fasano, C. Bellhouse, G. Hau, B. Vulcani, A. Biviano, A. Omizzolo, A. Paccagnella, M. D'Onofrio, A. Cava, Y. K. Sheen, W. Couch, and M. Owers. GASP. I. Gas Stripping Phenomena in Galaxies with MUSE. *The Astrophysical Journal*, 844:48, July 2017. ISSN 0004-637X. doi: 10.3847/1538-4357/aa78ed.

A. Raichoor and S. Andreon. Star formation and environment in clusters up to z ∼ 2.2. *Astronomy and Astrophysics*, 537:A88, Jan. 2012. ISSN 0004-6361. doi: 10.1051/0004-6361/201117998.

A. M. M. Reeves, M. L. Balogh, R. F. J. van der Burg, A. Finoguenov, E. Kukstas, I. G. McCarthy, K. Webb, A. Muzzin, S. McGee, G. Rudnick, A. Biviano, P. Cerulo, J. C. C. Chan, M. C. Cooper, R. Demarco, P. Jablonka, G. D. Lucia, B. Vulcani, G. Wilson, H. K. C. Yee, and D. Zaritsky. The GOGREEN survey: Dependence of galaxy properties on halo mass at z > 1 and implications for environmental quenching. *Monthly Notices of the Royal Astronomical Society*, 506(3):3364–3384, July 2021. ISSN 0035-8711, 1365-2966. doi: 10.1093/mnras/stab1955.

T. N. Reynolds, B. Catinella, L. Cortese, T. Westmeier, G. R. Meurer, L. Shao, D. Obreschkow, J. Román, L. Verdes-Montenegro, N. Deg, H. Dénes, B.-Q. For, D. Kleiner, B. S. Koribalski, K. Lee-Waddell, C. Murugeshan, S.-H. Oh, J. Rhee, K. Spekkens, L. Staveley-Smith, A. R. H. Stevens, J. M. van der Hulst, J. Wang, O. I. Wong, B. W. Holwerda, A. Bosma, J. P. Madrid, and K. Bekki. WALLABY pilot survey: H I gas disc truncation and star formation of galaxies falling into the Hydra I cluster. *Monthly Notices of the Royal Astronomical Society*, 510(2):1716–1732, Dec. 2021. ISSN 0035-8711, 1365-2966. doi: 10.1093/mnras/stab3522.

J. C. Roediger, L. Ferrarese, P. Côté, L. A. MacArthur, R. Sánchez-Janssen, J. P. Blakeslee, E. W. Peng, C. Liu, R. Munoz, J.-C. Cuillandre, S. Gwyn, S. Mei, S. Boissier, A. Boselli, M. Cantiello, S. Courteau, P.-A. Duc, A. Lançon, J. C. Mihos, T. H. Puzia, J. E. Taylor, P. R. Durrell, E. Toloba, P. Guhathakurta, and H. Zhang. The Next Generation Virgo Cluster Survey (NGVS). XXIV. The Red Sequence to ∼106 L ⊙ and Comparisons with Galaxy Formation Models. *The Astrophysical Journal*, 836:120, Feb. 2017. ISSN 0004-637X. doi: 10.3847/1538-4357/836/1/120.

V. C. Rubin, W. K. Ford, Jr., and N. Thonnard. Rotational properties of 21 SC galaxies with a large range of luminosities and radii, from NGC 4605 (R=4kpc) to UGC 2885 (R=122kpc). *The Astrophysical Journal*, 238:471–487, June 1980. ISSN 0004-637X. doi: 10.1086/158003.

E. S. Rykoff, E. Rozo, M. T. Busha, C. E. Cunha, A. Finoguenov, A. Evrard, J. Hao, B. P. Koester, A. Leauthaud, B. Nord, M. Pierre, R. Reddick, T. Sadibekova, E. S. Sheldon, and R. H. Wechsler. redMaPPer. I. Algorithm and SDSS DR8 Catalog. *The Astrophysical Journal*, 785:104, Apr. 2014. ISSN 0004-637X. doi: 10.1088/0004-637X/785/2/104.

A. Sandage, B. Binggeli, and G. A. Tammann. Studies of the Virgo cluster. V. Luminosity functions of Virgo cluster galaxies. *The Astronomical Journal*, 90:1759–1771, Sept. 1985. ISSN 0004-6256. doi: 10.1086/113875.

I. Santiago-Bautista, C. A. Caretta, H. Bravo-Alfaro, E. Pointecouteau, and H. Andernach. Identification of filamentary structures in the environment of superclusters of galaxies in the Local Universe. *Astronomy & Astrophysics*, 637:A31, May 2020. ISSN 0004-6361, 1432-0746. doi: 10.1051/0004-6361/201936397.

C. L. Sarazin. X-ray emission from clusters of galaxies. *Reviews of Modern Physics*, 58(1): 1–115, Jan. 1986. doi: 10.1103/RevModPhys.58.1.

J. Sayers, A. Montaña, T. Mroczkowski, G. W. Wilson, M. Zemcov, A. Zitrin, N. Cibirka, S. Golwala, D. Hughes, D. Nagai, E. D. Reese, D. Sánchez, and J. Zuhone. Imaging the Thermal and Kinematic Sunyaev-Zel'dovich Effect Signals in a Sample of 10 Massive Galaxy Clusters: Constraints on Internal Velocity Structures and Bulk Velocities. *The Astrophysical Journal*, 880:45, July 2019. ISSN 0004-637X. doi: 10.3847/1538-4357/ab29ef.

P. Schechter. An analytic expression for the luminosity function for galaxies. *The Astrophysical Journal*, 203:297–306, Jan. 1976. ISSN 0004-637X. doi: 10.1086/154079.

J. L. Sersic. *Atlas de Galaxias Australes*. Jan. 1968.

H. Shapley and A. Ames. A Survey of the External Galaxies Brighter than the Thirteenth Magnitude. *Annals of Harvard College Observatory*, 88:41–76, Jan. 1932.

T. Shibuya, M. Ouchi, and Y. Harikane. Morphologies of ∼190,000 Galaxies at z = 0-10 Revealed with HST Legacy Data. I. Size Evolution. *The Astrophysical Journal Supplement Series*, 219:15, Aug. 2015. ISSN 0067-0049. doi: 10.1088/0067-0049/219/2/15.

R. E. Skelton, K. E. Whitaker, I. G. Momcheva, G. B. Brammer, P. G. van Dokkum, I. Labbé, M. Franx, A. van der Wel, R. Bezanson, E. Da Cunha, M. Fumagalli, N. Förster Schreiber, M. Kriek, J. Leja, B. F. Lundgren, D. Magee, D. Marchesini, M. V. Maseda, E. J. Nelson, P. Oesch, C. Pacifici, S. G. Patel, S. Price, H.-W. Rix, T. Tal, D. A. Wake, and S. Wuyts. 3D-HST WFC3-selected Photometric Catalogs in the Five CANDELS/3D-HST Fields: Photometry, Photometric Redshifts, and Stellar Masses. *The Astrophysical Journal Supplement Series*, 214:24, Oct. 2014. ISSN 0067-0049. doi: 10.1088/0067-0049/214/2/24.

M. Slob, M. Kriek, A. G. Beverage, K. A. Suess, G. Barro, R. Bezanson, G. Brammer, C. M. Cheng, C. Conroy, A. de Graaff, N. M. F. Schreiber, M. Franx, B. Lorenz, P. E. M. Piña, D. Marchesini, A. Muzzin, A. B. Newman, S. H. Price, A. E. Shapley, M. Stefanon, P. van Dokkum, and D. R. Weisz. The JWST-SUSPENSE Ultradeep Spectroscopic Program: Survey Overview and Star-Formation Histories of Quiescent Galaxies at $1 < z < 3$, July 2024.

D. V. Stark. ACS Instrument Handbook for Cycle 33 v. 24.0. In *ACS Instrument Handbook for Cycle 33 v. 24.0*, volume 24, page 24. Dec. 2024.

V. Strazzullo, P. Rosati, M. Pannella, R. Gobat, J. S. Santos, M. Nonino, R. Demarco, C. Lidman, M. Tanaka, C. R. Mullis, C. Nuñez, A. Rettura, M. J. Jee, H. Böhringer, R. Bender, R. J. Bouwens, K. Dawson, R. Fassbender, M. Franx, S. Perlmutter, and M. Postman. Cluster galaxies in XMMU J2235-2557: Galaxy population properties in most massive environments at $z \sim 1.4$. *Astronomy and Astrophysics, Volume 524, id.A17, <NUMPAGES>14</NUMPAGES> pp.*, 524:A17, Dec. 2010. ISSN 0004-6361. doi: 10.1051/0004-6361/201015251.

V. Strazzullo, E. Daddi, R. Gobat, B. Garilli, M. Mignoli, F. Valentino, M. Onodera, A. Renzini, A. Cimatti, A. Finoguenov, N. Arimoto, M. Cappellari, C. M. Carollo, C. Feruglio, E. Le Floc'h, S. J. Lilly, D. Maccagni, H. J. McCracken, M. Moresco, L. Pozzetti, and G. Zamorani. Passive galaxies as tracers of cluster environments at $z \sim 2$. *Astronomy and Astrophysics*, 576:L6, Apr. 2015. ISSN 0004-6361. doi: 10.1051/0004-6361/201425038.

V. Strazzullo, E. Daddi, R. Gobat, F. Valentino, M. Pannella, M. Dickinson, A. Renzini, G. Brammer, M. Onodera, A. Finoguenov, A. Cimatti, C. M. Carollo, and N. Arimoto. The Red Sequence at Birth in the Galaxy Cluster Cl J1449+0856 at $z = 2$. *The Astrophysical Journal*, 833:L20, Dec. 2016. ISSN 0004-637X. doi: 10.3847/2041-8213/833/2/L20.

V. Strazzullo, M. Pannella, J. J. Mohr, A. Saro, M. L. N. Ashby, M. B. Bayliss, S. Bocquet, E. Bulbul, G. Khullar, A. B. Mantz, S. A. Stanford, B. A. Benson, L. E. Bleem, M. Brodwin, R. E. A. Canning, R. Capasso, I. Chiu, A. H. Gonzalez, N. Gupta, J. Hlavacek-Larrondo, M. Klein, M. McDonald, E. Noordeh, D. Rapetti, C. L. Reichardt, T. Schrabback, K. Sharon, and B. Stalder. Galaxy populations in the most distant SPT-SZ clusters. I. Environmental quenching in massive clusters at $1.4 < z < 1.7$. *Astronomy and Astrophysics*, 622:A117, Feb. 2019. ISSN 0004-6361. doi: 10.1051/0004-6361/201833944.

R. A. Sunyaev and Ia. B. Zeldovich. Microwave background radiation as a probe of the contemporary structure and history of the universe. *Annual Review of Astronomy and Astrophysics*, 18:537–560, Jan. 1980. ISSN 0066-4146. doi: 10.1146/annurev.aa.18.090180.002541.

A. Trudeau, J. P. Willis, D. Rennehan, R. E. A. Canning, A. C. Carnall, B. Poggianti, E. Noordeh, and M. Pierre. The XXL survey. XLIX. Linking the members star formation histories to the cluster mass assembly in the z=1.98 galaxy cluster XLSSC 122. *Monthly Notices of the Royal Astronomical Society*, 515(2):2529–2547, Aug. 2022. ISSN 0035-8711, 1365-2966. doi: 10.1093/mnras/stac1760.

A. Trudeau, A. H. Gonzalez, K. Thongkham, K.-S. Lee, S. Alberts, M. Brodwin, T. Connor, P. R. M. Eisenhardt, E. Moravec, E. Puvvada, and S. A. Stanford. The Massive and Distant Clusters of WISE Survey 2: A Stacking Analysis Investigating the Evolution of Star Formation Rates and Stellar Masses in Groups and Clusters. *The Astrophysical Journal*, 972(1):27, Aug. 2024. ISSN 0004-637X. doi: 10.3847/1538-4357/ad5545.

S. A. Urquhart, J. P. Willis, H. Hoekstra, and M. Pierre. An environmental Butcher-Oemler effect in intermediate-redshift X-ray clusters. *Monthly Notices of the Royal Astronomical Society*, 406:368–381, July 2010. ISSN 0035-8711. doi: 10.1111/j.1365-2966.2010.16766.x.

F. Valentino, M. Tanaka, I. Davidzon, S. Toft, C. Gómez-Guijarro, M. Stockmann, M. Onodera, G. Brammer, D. Ceverino, A. L. Faisst, A. Gallazzi, C. C. Hayward, O. Ilbert, M. Kubo, G. E. Magdis, J. Selsing, R. Shimakawa, M. Sparre, C. Steinhardt, K. Yabe, and J. Zabl. Quiescent Galaxies 1.5 Billion Years after the Big Bang and Their Progenitors. *The Astrophysical Journal*, 889:93, Feb. 2020. ISSN 0004-637X. doi: 10.3847/1538-4357/ab64dc.

R. F. J. van der Burg, S. McGee, H. Aussel, H. Dahle, M. Arnaud, G. W. Pratt, and A. Muzzin. The stellar mass function of galaxies in Planck-selected clusters at $0.5 < z < 0.7$: New constraints on the timescale and location of satellite quenching. *Astronomy and Astrophysics*, 618:A140, Oct. 2018. ISSN 0004-6361. doi: 10.1051/0004-6361/201833572.

R. F. J. van der Burg, G. Rudnick, M. L. Balogh, A. Muzzin, C. Lidman, L. J. Old, H. Shipley, D. Gilbank, S. McGee, A. Biviano, P. Cerulo, J. C. C. Chan, M. Cooper, G. De Lucia, R. Demarco, B. Forrest, S. Gwyn, P. Jablonka, E. Kukstas, D. Marchesini, J. Nantais, A. Noble, I. Pintos-Castro, B. Poggianti, A. M. M. Reeves, M. Stefanon, B. Vulcani, K. Webb, G. Wilson, H. Yee, and D. Zaritsky. The GOGREEN Survey: A deep stellar mass function of cluster galaxies at 1.0 < z < 1.4 and the complex nature of satellite quenching. *Astronomy and Astrophysics*, 638:A112, June 2020. ISSN 0004-6361. doi: 10.1051/0004-6361/202037754.

A. van der Wel, M. Franx, P. G. van Dokkum, and H. W. Rix. The Fundamental Plane of Field Early-Type Galaxies at z = 1. *The Astrophysical Journal*, 601:L5–L8, Jan. 2004. ISSN 0004-637X. doi: 10.1086/381887.

A. van der Wel, M. Franx, P. G. van Dokkum, R. E. Skelton, I. G. Momcheva, K. E. Whitaker, G. B. Brammer, E. F. Bell, H. W. Rix, S. Wuyts, H. C. Ferguson, B. P. Holden, G. Barro, A. M. Koekemoer, Y.-Y. Chang, E. J. McGrath, B. Häussler, A. Dekel, P. Behroozi, M. Fumagalli, J. Leja, B. F. Lundgren, M. V. Maseda, E. J. Nelson, D. A. Wake, S. G. Patel, I. Labbé, S. M. Faber, N. A. Grogin, and D. D. Kocevski. 3D-HST+CANDELS: The Evolution of the Galaxy Size-Mass Distribution since z = 3. *The Astrophysical Journal*, 788:28, June 2014. ISSN 0004-637X. doi: 10.1088/0004-637X/788/1/28.

C. Wang, R. Li, L. Gao, H. Shan, J.-P. Kneib, W. Wang, G. Chen, M. Makler, M. E. S. Pereira, L. Wang, M. A. G. Maia, and T. Erben. Do satellite galaxies trace matter in galaxy clusters? *Monthly Notices of the Royal Astronomical Society*, 475(3):4020–4026, Apr. 2018. ISSN 0035-8711. doi: 10.1093/mnras/sty073.

A. B. Watts, L. Cortese, B. Catinella, T. Brown, C. D. Wilson, N. Zabel, I. D. Roberts, T. A. Davis, M. Thorp, A. Chung, A. R. H. Stevens, S. L. Ellison, K. Spekkens, L. C. Parker, Y. M. Bahé, V. Villanueva, M. Jiménez-Donaire, D. Bisaria, A. Boselli, A. D. Bolatto, and B. Lee. VERTICO V: The environmentally driven evolution of the inner cold gas discs of Virgo cluster galaxies. *Publications of the Astronomical Society of Australia*, 40:e017, 2023. ISSN 1323-3580, 1448-6083. doi: 10.1017/pasa.2023.14.

K. Webb, M. L. Balogh, J. Leja, R. F. J. van der Burg, G. Rudnick, A. Muzzin, K. Boak, P. Cerulo, D. Gilbank, C. Lidman, L. J. Old, I. Pintos-Castro, S. McGee, H. Shipley, A. Biviano, J. C. C. Chan, M. Cooper, G. De Lucia, R. Demarco, B. Forrest, P. Jablonka, E. Kukstas, I. G. McCarthy, K. McNab, J. Nantais, A. Noble, B. Poggianti, A. M. M. Reeves, B. Vulcani, G. Wilson, H. K. C. Yee, and D. Zaritsky. The GOGREEN survey: Post-infall environmental quenching fails to predict the observed age difference between quiescent field and cluster galaxies at z > 1. *Monthly Notices of the Royal Astronomical Society*, 498:5317–5342, Nov. 2020. ISSN 0035-8711. doi: 10.1093/mnras/staa2752.

A. Werle, B. Poggianti, A. Moretti, C. Bellhouse, B. Vulcani, M. Gullieuszik, M. Radovich, J. Fritz, A. Ignesti, J. Richard, G. Soucail, G. Bruzual, S. Charlot, M. Mingozzi, C. Bacchini, N. Tomicic, R. Smith, A. Kulier, G. Peluso, and A. Franchetto. Post-starburst Galaxies in the Centers of Intermediate-redshift Clusters. *The Astrophysical Journal*, 930: 43, May 2022. ISSN 0004-637X. doi: 10.3847/1538-4357/ac5f06.

S. V. Werner, N. A. Hatch, A. Muzzin, R. F. J. van der Burg, M. L. Balogh, G. Rudnick, and G. Wilson. Satellite quenching was not important for z $\sim$ 1 clusters: Most quenching occurred during infall. *Monthly Notices of the Royal Astronomical Society*, 510(1):674–686, Feb. 2022. ISSN 0035-8711. doi: 10.1093/mnras/stab3484.

A. R. Wetzel, J. L. Tinker, C. Conroy, and F. C. van den Bosch. Galaxy evolution in groups and clusters: Satellite star formation histories and quenching time-scales in a hierarchical Universe. *Monthly Notices of the Royal Astronomical Society*, 432:336–358, June 2013. ISSN 0035-8711. doi: 10.1093/mnras/stt469.

S. D. M. White and C. S. Frenk. Galaxy Formation through Hierarchical Clustering. *The Astrophysical Journal*, 379:52, Sept. 1991. ISSN 0004-637X. doi: 10.1086/170483.

S. D. M. White and M. J. Rees. Core condensation in heavy halos: A two-stage theory for galaxy formation and clustering. *Monthly Notices of the Royal Astronomical Society*, 183: 341–358, May 1978. ISSN 0035-8711. doi: 10.1093/mnras/183.3.341.

J. P. Willis, N. Clerc, M. N. Bremer, M. Pierre, C. Adami, O. Ilbert, B. Maughan, S. Maurogordato, F. Pacaud, I. Valtchanov, L. Chiappetti, K. Thanjavur, S. Gwyn, E. R. Stanway, and C. Winkworth. Distant galaxy clusters in the XMM Large Scale Structure survey. *Monthly Notices of the Royal Astronomical Society*, 430(1):134–156, Mar. 2013. ISSN 1365-2966, 0035-8711. doi: 10.1093/mnras/sts540.

J. P. Willis, R. E. A. Canning, E. S. Noordeh, S. W. Allen, A. L. King, A. Mantz, R. G. Morris, S. A. Stanford, and G. Brammer. Spectroscopic confirmation of a mature galaxy cluster at redshift two. *Nature*, 577(7788):39–41, Jan. 2020. ISSN 0028-0836, 1476-4687. doi: 10.1038/s41586-019-1829-4.

Ya. B. Zeldovich and R. A. Sunyaev. The Interaction of Matter and Radiation in a Hot-Model Universe. *Astrophysics and Space Science*, 4:301–316, July 1969. ISSN 0004-640X. doi: 10.1007/BF00661821.

H. Zhao. Analytical models for galactic nuclei. *Monthly Notices of the Royal Astronomical Society*, 278:488–496, Jan. 1996. ISSN 0035-8711. doi: 10.1093/mnras/278.2.488.

S. Zou, B. J. Maughan, P. A. Giles, A. Vikhlinin, F. Pacaud, R. Burenin, and A. Hornstrup. The X-ray luminosity–temperature relation of a complete sample of low-mass galaxy clusters. *Monthly Notices of the Royal Astronomical Society*, 463(1):820–831, Nov. 2016. ISSN 0035-8711. doi: 10.1093/mnras/stw1992.

F. Zwicky. Die Rotverschiebung von extragalaktischen Nebeln. *Helvetica Physica Acta*, 6: 110–127, Jan. 1933. ISSN 0018-0238.

Appendix A

CL J021741.7-034546

A.1 CL J021741.7-034546

When creating the updated catalogue of XLSSC 122 cluster members, a significant overdensity of galaxies around $z = 1.93$ was discovered close to XLSSC 122. The G141 grism's range allows for a similar spectroscopic redshift identification of these galaxies as for the primary cluster. Included below in Fig. A.1 and Fig. A.2 are the colour magnitude diagrams for the second cluster, CL J021741.7-034546. These are shown in both filter combinations used for the XLSSC122 figures, with the same colour cuts. The colour of the red and blue populations are similar to those seen in XLSSC 122, with a low scatter flat red coloration at an F105W-F140W colour of 1.4, and a blue cloud with high scatter around a colour of 0.5 from the same bands. There are 47 galaxies in the gold and silver categories of CL J021741.7-034546 as seen in the cluster membership map in Fig. A.3. Given the large number of these galaxies distributed around a central location, I label it a galaxy cluster. The central point of this cluster is listed as the barycentre of the 12 galaxies nearest the brightest classified galaxy. This cluster, though it may have complicated the classification of some members of XLSSC 122, is distinctly separated from that cluster, and is not dynamically interacting with the cluster. As such it has no additional bearing on the investigation of XLSSC 122. However, as a galaxy cluster it also shows a strong colour bimodality and the occasional post-starburst galaxy. CL J021741.7-034546 does have a much larger proportion of blue galaxies, most galaxies in the cluster are blue, with a strong red core at the very centre. CL J021741.7-034546 has a red fraction of $0.26\% \pm 12\%$. These signs point to CL J021741.7-034546 being a smaller, less mature cluster than XLSSC 122.

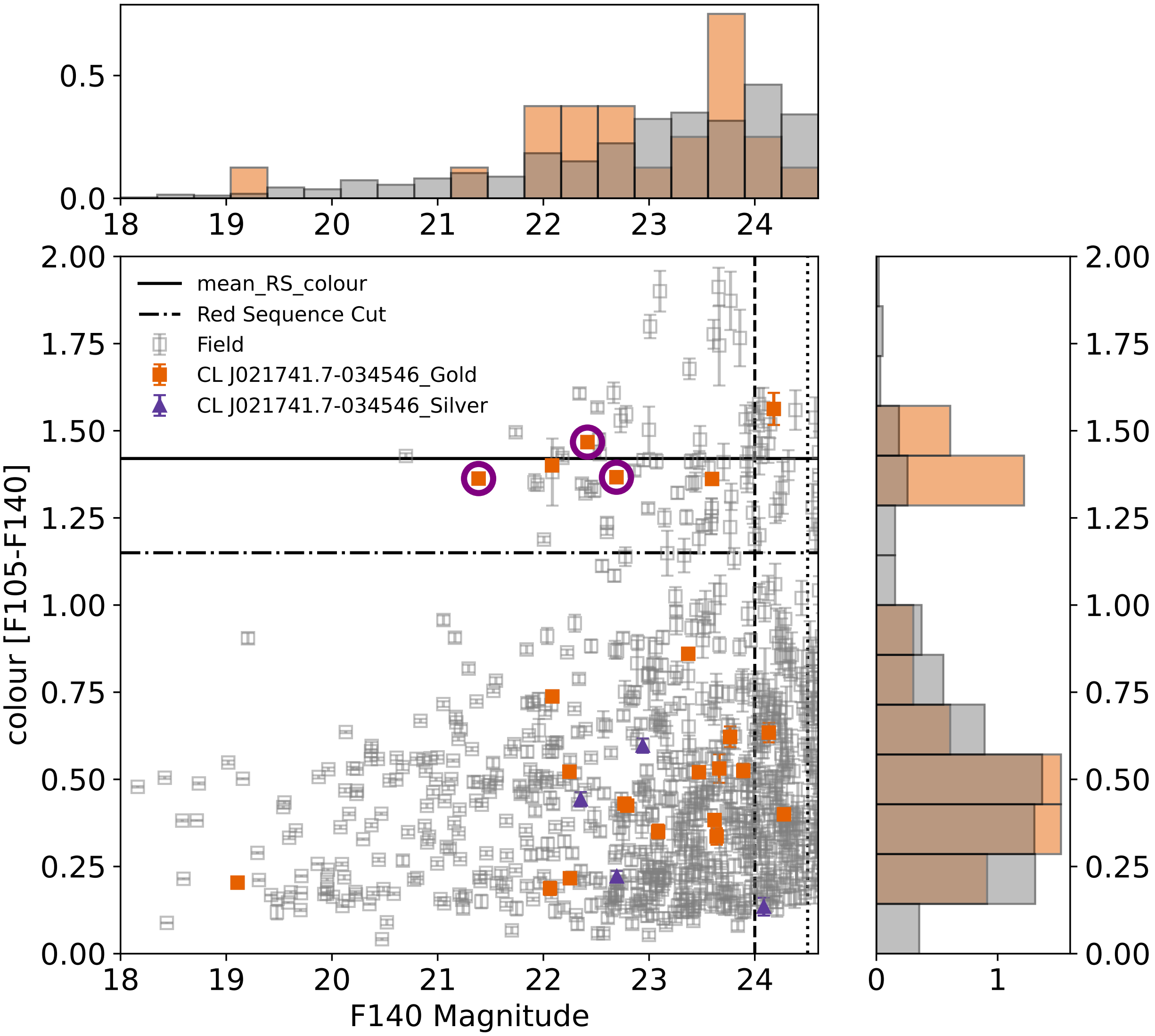

Figure A.1: A Colour-Magnitude Diagram of the full CL J021741.7-034546 photometric field. Red and green points are gold and silver members respectively. Membership is determined by the MCMC probability within $z = (1.96, 2.00)$. Grey points represent all photometrically extracted objects in the area. Vertical lines designate the 24 and 24.5 magnitude limits on cluster membership from prior core observations. The dash-dot horizontal line at 1.15 in colour indicates the red-sequence blue-cloud cut. The solid horizontal black line indicates the mean colour of the gold red sequence members. The histograms show the relative normalized number density of cluster members (orange) to non-cluster-members (grey) over magnitude.

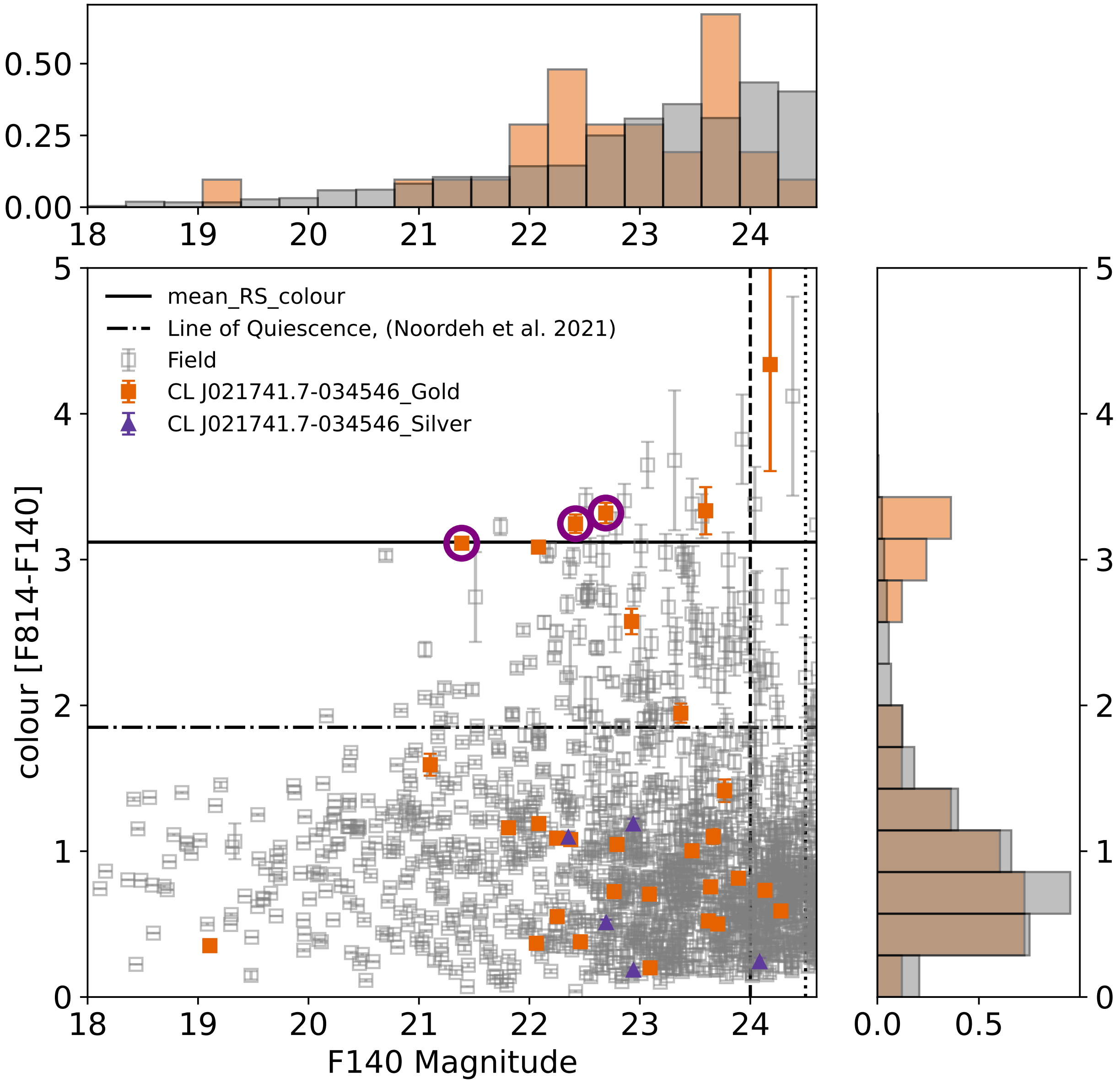

Figure A.2: A Colour-Magnitude Diagram of the full CL J021741.7-034546 photometric field. Red and green points are gold and silver members respectively. Membership is determined by the MCMC probability within $z = (1.96, 2.00)$. Grey points represent all photometrically extracted objects in the area. Vertical lines designate the 24 and 24.5 magnitude limits on cluster membership from prior core observations. The dash-dot horizontal line at 1.85 in colour indicates the red-sequence blue-cloud cut from (Noordeh et al., 2021) given as a quenched cut. The solid horizontal black line indicates the mean colour of the gold red sequence members. The histograms show the relative normalized number density of cluster members (orange) to non-cluster-members (grey) over magnitude.

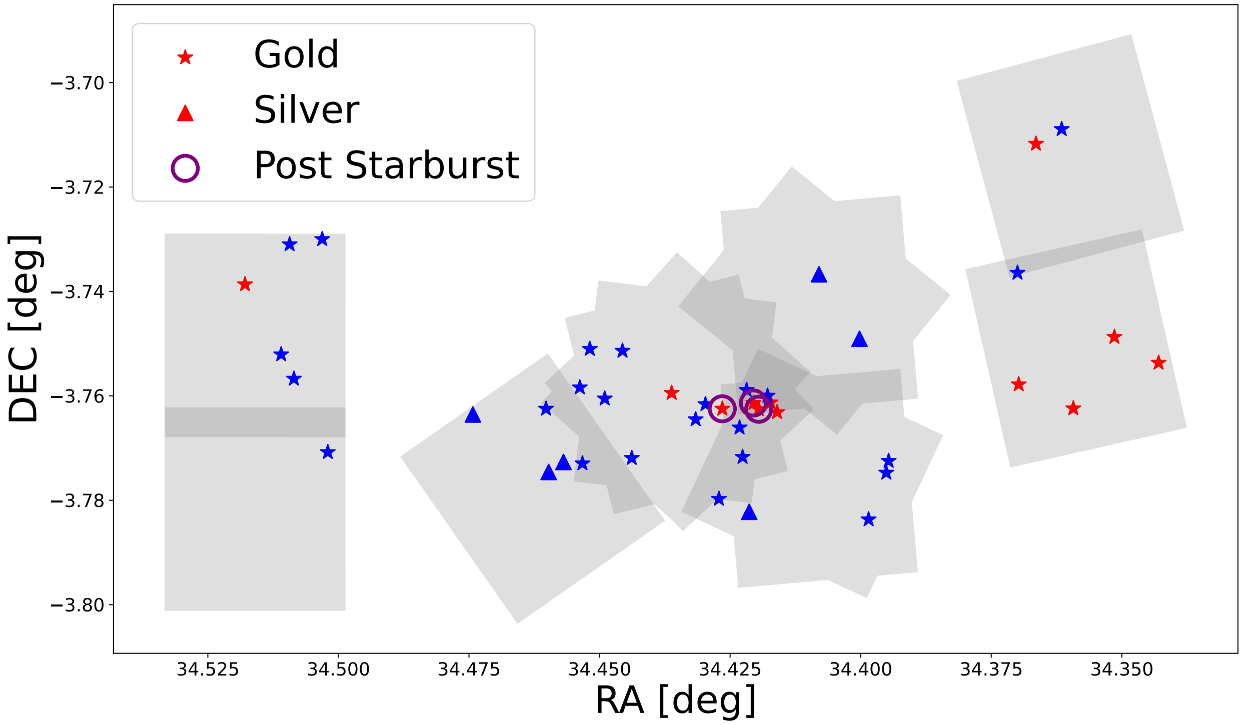

Figure A.3: A footprint map with the F140W+G141 exposure in grey. Members of the Gold/Silver classification of z = 1.93 structure members is shown with stars/triangles. Cluster members are coloured red or blue based on the colour cuts in F105W-F140W = 1.15 in the central region, and F814W-F140W = 1.85 in the far regions. post-starburst galaxies are indicated by a purple circle.